DYNAMICS AND STRUCTURE IN METALLIC SUPERCOOLED LIQUIDS AND GLASSES STUDIED BY NMR

Lilong Li

A dissertation submitted to the faculty of the University of North Carolina at Chapel Hill in partial fulfillment of the requirements for the degree of Doctor of Philosophy in the Curriculum in Applied and Materials Sciences.

Chapel Hill
2005

Approved by

Advisor: Yue Wu

Reader: M. Gregory Forest

Reader: Alfred Kleinhammes

Reader: Lu-Chang Qin

Reader: Sean Washburn

Reader: Otto Zhou

ABSTRACT

LILONG LI: Dynamics and Structure in Metallic Supercooled Liquids and Glasses Studied by NMR
(Under the direction of Yue Wu)

In this dissertation, we used high temperature NMR to study the dynamic behavior of metallic liquids and glasses from completely molten state to temperatures well below the glass transition. We found that there are different processes in the system that have distinct effects to NMR probing methods, so we employed several NMR techniques to study these processes separately. A dramatic temperature dependence of Knight shift was recorded and it was attributed to the fast vibration and rattling processes. A transition was directly observed at T_c which is about 100 K above the glass transition temperature. The result was shown to be consistent with MCT, mode coupling theory. Nuclear quadrupolar relaxation, 1-d lineshape analysis and stimulated echo techniques were utilized to study the slow processes. At high temperatures, the dynamics follow the MCT predictions. Starting from T_c and below, a decoupling in diffusion behavior between the light/small atoms and heavy/big ones was discovered. We discussed possible dynamic and thermodynamic explanations.

In the second part of the dissertation, we used NMR to study the primary crystallization in some Aluminum-based metallic glasses. A precursor for crystallization was found even in as-quenched samples. A common metastable state was discovered at low temperatures. We also presented some studies on the electronic structure and short-range order of some metallic glasses and possible correlations of such properties with the glass forming ability.

TO MY PARENTS

ACKNOWLEDGMENTS

I'd like to thank first and foremost my advisor, Yue Wu, for his guidance and help throughout my graduate study. His enthusiasm for and insight into science have perpetually stimulated me. Discussing with him has always been refreshing experiences due to his broad knowledge, good intuition and quickness of thought.

Experimental work in the lab would not be possible if not for the training and help from other group members, past and present: Xiaoping Tang, Jonathan Baugh, Yuanyuan Jia, Shenghua Mao, Harsha Kulkarni, and particularly Alfred Kleinhammes. I also thank Horst Keisemmier for discussions and encouragements. I'd like to express my gratitude to everyone, especially my advisor Yue Wu, for the help in writing and oral presentations.

I benefited from the discussions and collabrations with other groups, particularly Johnson's group at Caltech, Perepezko's group at University of Wisconsin–Madison, and Wang's group at the Institute of Physics, Chinese Academy of sciences. I especially thank the members of my committee: Alfred Kleinhammes, Lu-Chang Qin, Sean Washburn, Yue Wu, Otto Zhou. M. Gregory Forest and Edward Samulski gave valueable advise and critique till the final oral defense, which they are unable to attend due to schedule conflicts.

The work was supported by the U.S. Army Research Office (Grant No. DAAD19-02-1-0225) and by the National Science Foundation (Grant No. DMR-0139452).

I am so grateful to my parents and my brother. They are the forever support of my

life, for whichever path I choose. Finally I'd like to express my love and gratitude to Qian. It would have been so much harder without her company.

CONTENTS

LIST OF FIGURES

LIST OF ABBREVIATIONS

BMG	Bulk Metallic Glass
CSA	Chemical Shift Anisotropy
CSRO	Chemical Short Range Order
DOS	Density of States
DSC	Differential Scanning Calorimetry
EFG	Electric Field Gradient
fcc	Face-Centered Cubic
FID	Free Induction Decay
FWHM	Full Width at Half Maximum
GFA	Glass Forming Ability
IS	Inherent Structure
MCT	Mode Coupling Theory
MSR	Melt Spun Ribbon
NMR	Nuclear Magnetic Resonance
NQR	Nuclear Quadrupolar Relaxation
rf	Radio Frequency
RFOT	Random First Order Transition
RT	Room Temperature
TEM	Transmission Electron Microscopy
TTT	Time-Temperature-Transformation
XRD	X-Ray Diffraction

CHAPTER 1

INTRODUCTION

The approach to condensed matter physics very often starts from molecules or atoms in translational symmetry, the theory of which has been developed in great detail. However, there is a whole range of systems, with various degree of disorder, that exhibit new types of physical behavior that cannot be understood unless the disorder is taken as a fundamental aspect of the physics involved. Liquids and glasses are examples of such systems.

1.1 Supercooled Liquids, Glasses and the Glass Transition

Glasses are usually made by cooling a liquid to sufficiently low temperatures while preventing crystallization. A liquid that is cooled below its liquidus temperature T_{liq} is called a supercooled liquid. As a supercooled liquid is cooled to lower temperatures, the molecular movements become more and more sluggish, and the time-scale for molecular rearrangement to reach thermodynamic equilibrium state (structural relaxation) gets extremely long below certain temperatures. The systemremains in thermodynamic non-equilibrium state, and in all practical senses, the material now becomes a

solid, and is called a glass. This transition from highly viscous supercooled liquid to a non-equilibrium state of a rigid solid is called glass transition, and the temperature associated with the glass transition is called glass transition temperature T_g.

T_g can be defined in many different ways. One convenient way is to observe the enthalpy or specific volume as a function of temperature. As shown in Figure 1.1, there is a change in heat capacity as the material goes from the liquid state to the glass state. This will result in a step transition in Differential Scanning Calorimetry (DSC) curves, so T_g can thus be quantitatively determined experimentally. It is important to note that the glass transition does not occur suddenly but depends on the cooling rate.

It is now widely believed that the structure of the material, while undergoing a transition from the liquid state to the glass state, varies little and smoothly if any, over the entire temperature range. There is no abrupt change of structure at any temperature region. The liquid-glass transition is thus regarded as a kinetic phenomenon. But to understand such a phenomenon proved to be a serious intellectual challenge in condensed matter physics. All kinds of complex phenomena observed, the dynamics ranging from picosecond to the order of 1000 seconds, a broad range of glass-formers, from biological tissues to polymers, from oxides to metallic alloys, from granular materials to spin glasses, capture the interests and imagination of researchers, theorists and experimentalists alike, to the problem of glass transition. Among all the theoretical efforts, mode coupling theory stands out as a theory that predicts precisely several aspects of the behavior of simple liquids as they are cooled down towards the glass transition. Yet so far, some experimental tests of MCT still remain ambiguous. There is great need to use simple glass forming system to capture the essential features, to employ new experimental strategies, and to put experimental observations in a coherent theoretical context. In this dissertation, we employed various NMR techniques to study several metallic glass formers and got a comprehensive picture of the dynamical

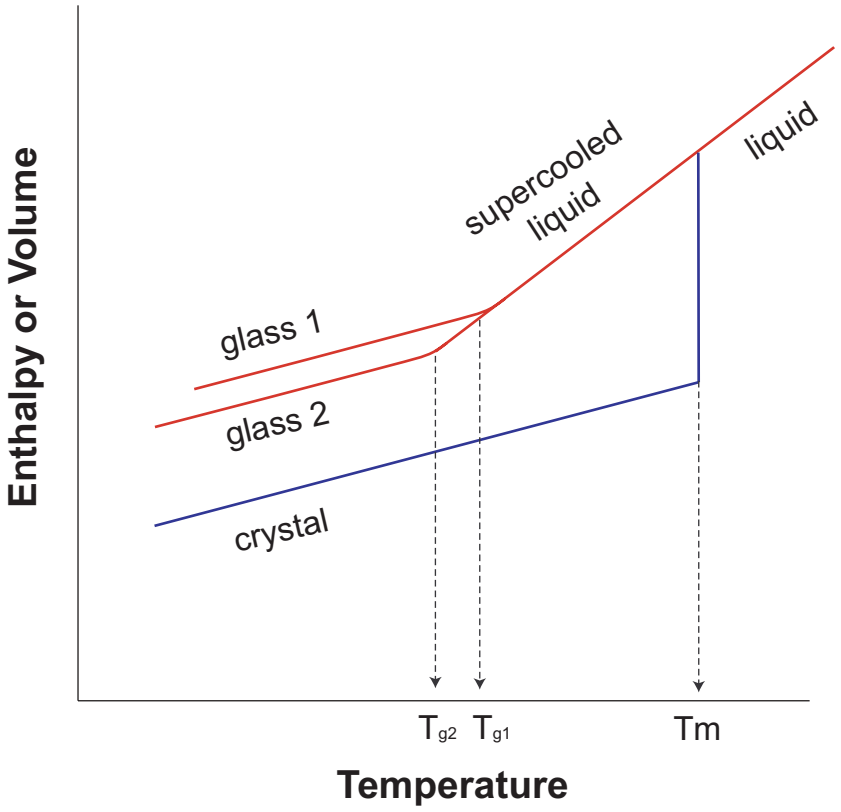

Figure 1.1: Enthalpy or volume as a funtion of temperature as system undergoes crystallization or glass transition. Glass 1 has a higher cooling rate than glass 2.

behavior of these systems as a function of temperature. We will compare our results with the dynamical theory of liquids and glasses, or specifically the MCT.

The perspective of viewing the glass transition as a pure kinetic phenomena is not left un-challenged, however. Theories have been developed to treat the glass transition thermodynamically, and to explain the phenomenology topologically or quantitatively with thermodynamic quantities. Energy landscape theory and random first order transition (RFOT) theory are two theories that will be discussed in the dissertation. Although these theories consider the thermodynamic aspect of the glass transition, they are not irreconcilable with the dynamical theories. They are two aspects of the same problem. Thus a unification of the theories is anticipated.

1.2 Metallic Glasses and Bulk Metallic Glasses

It was first reported by Duwez at Caltech in 1960 of the glass formation of $Au_{75}Si_{25}$ alloy (Klement et al., 1960). They developed rapid quenching techniques for cooling metallic liquids at rates of $10^5 - 10^6$ K/s, and started the whole field of metallic glasses. Later in the 1970s and 1980s quenching and casting techniques were developed to manufacture metallic glasses in shapes of ribbons, lines, and sheets. During this period, Turnbull and coworkers made crucial contribution to the discipline. They demonstrated that metallic glasses are another kind of glass, similar to any other conventional glasses such as silicates, polymers etc. They also led the early studies of glass forming ability (GFA)(Turnbull, 1961; Chen and Turnbull, 1968; Chen and Turnbull, 1969; Turnbull and Fisher, 1949; Turnbull, 1969).

If one arbitrarily defines a metallic glass that reaches millimeter scale in all three dimensions as being "bulk", the first bulk metallic glass (BMG) was produced by Chen in 1974 (Chen, 1974). Turnbull and coworkers later on developed Pd-Ni-P BMG system and used boron oxide fluxing method to purify the melt and prevent heterogeneous nucleation (Drehman et al., 1982; Kui et al., 1984). Some metallic glasses studied in this dissertation are recent developments to Turnbull's Pd-Ni-P system, the most important one of which, $Pd_{43}Ni_{10}Cu_{27}P_{20}$, is probably the best metallic glass former so far found (Lu et al., 1999). In the late 1980s, Inoue et al at Tohoku University systematically investigated the GFA of alloys of rare earth elements with Al and ferrous metals (Inoue, 2000). Another part of the dissertation is related to this type of compositions. It is worthwhile to note some other metallic glass systems here too: Zr-based metallic glasses developed by Johnson group in Caltech with compositions such as $Zr_{41.2}Ti_{13.8}Cu_{12.5}Ni_{10.0}Be_{22.5}$(Peker and Johnson, 1993), which were most extensively studied; BMGs based on yttrium (Guo et al., 2003).

Metallic glasses provide a new kind of materials to study the glass transition phe-

nomenon. They are relatively new-comers to the world of glasses, yet they represent a type of glass that has different bonding, namely the metallic bonding, and they are closest to dense random packing among all structural glasses. The simpler structure and dynamics of metallic glass-forming liquids and glasses would provide essential feature of the glass transition phenomenon and give us a better understanding of the very nature of glass transition. The research possibility used to be very limited on metallic glasses, but with the development of BMGs that stay in the supercooled liquid state for a minimum of several minutes, new momentum are gathered in this research field. We'll see that there are several NMR techniques that can be used to study the dynamics in metallic supercooled liquids and glasses which can provide insight into the very nature of glass transition.

1.3 Structure and Crystallization Mechanism

Metallic glasses possess some unique properties that are superior to conventional crystalline metals and alloys, such as high strength (close to theoretical limits for metals and alloys), high elastic strain limit, high hardness, very good corrosion resistance, and soft magnetism (low coercivity and low hysteresis). These properties offer many structural and functional applications for metallic glasses once they can be made in bulk form. BMGs can become soft in moderately elevated temperatures, which suggests unique processing possibilities compared with conventional metals and alloys. However, there are still limitations to BMGs, and one of them is that the material costs are relatively high. Furthermore, there are very specific requirements for the properties for metallic glasses, for example, very high density, or density as low as possible while retaining high strength. Aluminum is a very good candidate for light weight metallic glasses, yet so far, Al-based metallic glasses are very easy to crystallize. It is crucial to characterize

the crystallization behavior of such metallic glasses and find a way to avoid it. NMR is a good tool in characterizing local structures and may prove very useful in this regard.

Theoretically, since when Fahrenheit performed the first recorded undercooling experiment on liquid water (Fahrenheit, 1724), it has been made clear that in terms of the first order phase transition, there is a barrier separating the initial and final phases. Nucleation, or stochastic thermally activated transition over that barrier, is normally treated within the classical theory of nucleation, a phenomenological model that describes the time-evolution of the size distribution of clusters of the new phase. Nucleation in supercooled liquids and glasses now seems to require a revisit of the nucleation theories to test and refine them. A better understanding of the nucleation in liquids and glasses will also provide us an improved ability to manipulate nucleation processes to produce desired microstrutures for practical applications. In this dissertation, some unusual crystallization behavior of an Al-based metallic glass was studied by NMR, and we try to relate our observation to nucleation theories.

Local icosahedral order in amorphous metals is frequently invoked to explain the high barrier of some supercooled metallic liquids against crystallization. This would imply a minimum in electronic density of states at the Fermi level (Nagel and Tauc, 1975; Tang et al., 1997). We can use NMR to study the electronic properties of some metallic glasses and see how electronic energy will influence the glass forming ability, or how the changes in chemical composition would influence the electronic structure of the metallic glass system.

1.4 NMR as a Probe of Structure and Dynamics

NMR is a powerful tool to probe locally the atomic environment and the change of it—the dynamics. We'll see in this dissertation that the NMR spectra offer detailed local

structural information, and can also characterize the electronic structure of metals. The rate of spin lattice relaxation (T_1) can indicate bonding characteristics, provide the rate of dynamical processes. The temperature dependence of spectra shift and shape can provide information on the amplitude of vibrational processes and the rate of chemical exchange. Furthermore, complicated NMR pulse sequences can be employed to accomplish advanced requirements for studying structure and dynamics in certain systems. With a home-made high temperature probe, we can vary the temperature in-situ and observed the temperature dependence of NMR observables. NMR, being a non-destructive, non-perturbing technique, is ideal for the research objectives outlined in this dissertation.

1.5 Dissertation Outline

In chapter 2, we describe the theory of dynamics in a liquid, and introduce the mode coupling theory, which extends the earlier theories to the case of deeply supercooled state. We emphasize the importance of T_c, critical temperature predicted by MCT where ergodicity to non-ergodicity transition occurs. T_c is higher than T_g, so the actual transition happens at some point higher than T_g and T_g is nothing particular but a point where the time scale of relaxation crosses the experimental time scale according to MCT in the extended form.

In chapter 3, we use high temperature NMR to study the temperature dependence of ^{31}P Knight shift in some BMG systems. We show that the change of Knight shift is proportional to the amplitude of the vibrational processes. We observed directly an abrupt change of Knight shift at some point T_c which is about 100 K above T_g. This demonstrates that our experimental results are compatible with MCT. The basics of NMR spectroscopy is also introduced to readers not so familiar with the details

involved.

In chapter 4, a variety of other NMR techniques are employed to study the slower processes in metallic supercooled liquids and glasses. The temperature dependence of the rate constant for the slow processes is obtained from RT to about 1000 K. The difference between the data from other published results are compared and explained. The NMR theories behind each technique are summarized. Theories of glass transition from thermodynamic point of view are also presented in this chapter. How these theories can describe our experimental observation is discussed.

In chapter 5, we'll study the primary crystallization in $Al_{92}Sm_8$, and discuss the possible relationship between glass forming ability and CSRO/electronic structure.

CHAPTER 2

THEORY OF LIQUIDS AND THE GLASS TRANSITION

2.1 Glass Transition as a Transition in Dynamics

In general, when a liquid is cooled, the mobility in the liquid decreases, diffusion constants decrease and the viscosity increases. The time scale for relaxation of the liquid becomes longer. When the liquid is further cooled and in the absence of crystallization, the time scale for relaxation in the liquid exceeds the time scale of the experiment, the material behaves more like a solid than a liquid, and we call it a glass. This transition from a liquid to a glass is then the glass transition. The glass transition behaves like a second-order phase transition, but it's not strictly a second-order phase transition in the thermodynamic sense. There's no good order parameter to characterize such a transition. The difference between the glass and a liquid is widely viewed as an issue of kinetics rather than thermodynamics. In the framework of statistical mechanics, the configuration spaces of the glass and the liquid are fundamentally the same. The configuration space of the glass appears smaller just because on the time scale of the experiment, the glass does not relax. In this sense a glass is therefore not in an

equilibrium state.

Structurally a glass is barely distinguishable from the liquid of which it is formed. In fact, both experimental observations and molecular dynamics simulations show that the structure varies smoothly across the entire temperature range of supercooled liquids and glasses with no special anomaly found at any temperature (Bernu et al., 1985; Moutain and Thirumalai, 1987; Ullo and Yip, 1989; Meyer et al., 1996a). Now glass transition is commonly interpreted in the context of transition in dynamics (Jäckle, 1986; Richter et al., 1989; Angell, 1995). However in chapter 4, we'll discuss the thermodynamic approaches to the glass transition. Thermodynamic and dynamic considerations may turn out to be different but complementary approaches to the same phenomena, but not mutually excluding theories.

2.2 Theory of Dynamics in Liquid

The dynamics of the liquid at microscopic level are described by the classical equation of motion of a very large number of particles. Early theories of fluid considers only short-range uncorrelated binary collisions of the constituent particles, which leads to the conclusion that any fluctuation from equilibrium decays with an exponential dependence on time.

Further theoretical development for the dynamics of fluids came from studying the relaxation behavior of liquids near the critical point, where a long tail of relaxation is observed (Kawasaki, 1966).

The relevance of the mode-coupling theory to the theory of the glass transition emerged with the idea of expressing the mode-coupling terms in terms of the density correlation function ϕ. With this approach, one can obtain a closed equation for ϕ and predict the dynamics of a densely packed liquid. As a result of the mode coupling

study of the glass transition phenomenon, a dynamic transition of the liquid to non-ergodic state was predicted (Geszti, 1983; Bengtzelius et al., 1984; Leutheusser, 1984). In the long-time limit, the density correlation function ψ freezes to a nonzero value beyond the transition point which was later verified to be above T_g, the glass transition temperature. The thermodynamic quantities of the liquid is said to vary smoothly through the transition. The viscosity would follow a power-law divergence approaching the dynamical transition point accompanied by a finite shear modulus in the glassy state. Such a sharp transition at a temperature T_c above T_g was not observed in real systems, so the theory was further developed to incorporate the coupling of current terms, which would restore the ergodicity at temperatures below T_c (Das and Mazenko, 1986).

Now we get down to the equations for macroscopic hydrodynamics and mode coupling theory.

2.2.1 Conventional Hydrodynamics

We'll write down without proof the equation for local densities in a classical liquid (Zubarev et al., 1997; Martin et al., 1972):

$$\begin{aligned} &\partial_t \rho + \bigtriangledown \cdot \vec{g} = 0 \\ &\partial_t g_i + \bigtriangledown_j [g_i g_j/\rho] = - \bigtriangledown P + L^0_{ij} \nu_j \\ &\partial_t \epsilon + \vec{v} \cdot \bigtriangledown \epsilon = -h \bigtriangledown \cdot \vec{v} + \lambda \bigtriangledown^2 T \end{aligned} \tag{2.1}$$

where $\{\rho(\vec{r},t), \vec{g}(\vec{r},t), \epsilon(\vec{r},t)\}$ are the local mass density, mass current, and energy density in the system, $\vec{v} = \vec{g}/\rho$ is the velocity, λ is the thermal conductivity, $h = e + P$ is the enthalpy density, with e the energy density and P the pressure in equilibrium. The

dissipation matrix L^0_{ij} relates to the viscosity in the following way:

$$L^0_{ij} = \eta^{'}_0 \delta_{ij} \bigtriangledown^2 + \eta_0 \bigtriangledown_i \bigtriangledown_j \tag{2.2}$$

with the longitudinal viscosity $\eta^{'}_0 = \zeta_0 + \eta_0/3$.

Eq. 2.1 describes the conservation of mass, the dissipation of mass and energy respectively. The transport coefficients (thermal conductivity, and viscosity) in Eq. 2.1 are system-dependent and are treated as inputs. Transport coefficients for a given interaction potential can be computed in the framework of the kinetic theory of liquids. To compute the transport coefficients in terms of the basic interactions, suitable kinetic equations must be used to describe the irreversible dynamics at the microscopic level. Liouville equation (Hansen and McDonald, 1990) is just such a theory to include microscopic dynamics. In the simplest form the dynamics are taken into account at the level of two-body uncorrelated collisions. Enskog corrections improves Liouville equations at higher densities to obtain density dependent transport coefficients (Chapman and Cowling, 1991; Résibois and de Leener, 1977).

Hydrodynamic variables fluctuate due to the random motion of the fluid particles. Conventional hydrodynamics considers properties of the fluid over length and time scale long compared to the corresponding microscopic scales. So the fluctuations of interest are those of low frequency ω and small wave number q, so that $\omega\tau_c \ll 1$ and $ql \ll 1$, where τ_c is the mean time between collisions and l the average particle spacing in the liquid. To get a hydrodynamic equation, we do a Fourier-transform for the first two equations in Eq. 2.1 (we ignore the energy fluctuation first) in the small q-limit, and get:

$$\begin{aligned} &\partial_t \delta\rho(q,t) + i\vec{q}\cdot\vec{g}(k,t) = 0 \\ &\partial_t \vec{g}(q,t) + i\vec{q}c_0^2 + \eta_0^K q^2 \vec{g}(q,t) + \eta_0^{'k}\vec{q}q\cdot\vec{g}(k,t) = 0 \end{aligned} \tag{2.3}$$

where $\eta_0'^K = \eta_0'/\rho_0$ and $\eta_0^K = \eta_0/\rho_0$, with ρ_0 being the average mass density, $c_0^2 = (\partial P/\partial\rho)_T$ is the isothermal speed of sound. From the above equation, one can get longitudinal and transversal modes that are decaying exponentially in an isotropic liquid. If we include energy fluctuation in Eq. 2.3, another *heat mode* comes in which also decays exponentially.

2.2.2 Generalized Hydrodynamics

To go beyond the conventional hydrodynamics so that a theoretical description of the dynamics in a dense fluid becomes possible, one approach is to include in conventional hydrodynamics the short wave-length, short time phenomena. One can do so by replacing thermodynamic properties or transport coefficients with functions that can vary in space and time. The resulting theory is termed *generalized hydrodynamics*. In generalized hydrodynamics, the equation of motion for the conserved densities of mass, momentum and energy were obtained using the *projection operator* technique of Mori and Zwanzig (Zwanzig, 1961; Mori, 1965b; Mori, 1965a).

Consider a set of dynamical variable $\{A_i(\vec{r},t)\}$that follows the Liouville equation, i.e., $A_i(t) = \exp(i\mathcal{L}t)A_i$, where $\mathcal{L}$ is the Liouville operator (Hansen and McDonald, 1990) and $A_i \equiv A_i(t=0)$. For some other dynamical variable $B(t)$, the projection operator $\mathcal{P}$ is defined as,

$$\mathcal{P}B(t) = \sum_{j,k} \left\langle B(t)A_j^* \right\rangle \left\langle A_j^* A_k \right\rangle^{-1} A_k \tag{2.4}$$

where the angular brackets denote the equilibrium average. The projection operator $\mathcal{P}$ projects variable $B(t)$ into $\{A_i(\vec{r},t)\}$ subspace, while operator $\mathcal{Q} = 1 - \mathcal{P}$ denotes the projection in the orthogonal subspace. Now one can obtain (Hansen and McDonald,

1990) the equations for the time evolution of the dynamic variable A_i:

$$\dot{\vec{A}}(t) - i\vec{\Omega}\cdot\vec{A}(t) + \int_0^t \vec{M}(t-s)\cdot\vec{A}(s)ds = \vec{R}(t) \tag{2.5}$$

Here $\vec{A}$ becomes a column vector with the A_i's. The frequency matrix $\vec{\Omega}$ and the random force vector $\vec{R}$ are given by:

$$\begin{aligned} \Omega_{ij} &= \sum_k \left(A_i^* i\mathcal{L}A_k\right)\chi_{kj}^{-1} \\ R_i(t) &= \exp(i\mathcal{Q}L\mathcal{Q}t)K_i \end{aligned} \tag{2.6}$$

with $K_i = Q\dot{A}_i$ and χ the equilibrium correlation function matrix $\chi_{ij} = \langle A_i^* A_j\rangle$. $\vec{R}(t)$ on the right side of Eq. 2.5 is orthogonal to the space of $\vec{A}$ at all times, or $\langle A_i^* R_j(t)\rangle = 0$. One important quantity in Eq. 2.5 is the *memory function* $\vec{M}$: $\vec{M}$ relates $\dot{\vec{A}}$ to $\vec{A}$ at short times and is expressed in terms of the correlation of forces $\vec{R}(t)$ in the subspace of $\mathcal{Q}$:

$$M_{ij} = \sum_k \langle R_i R_k(t)\rangle \chi_{kj}^{-1} \tag{2.7}$$

One can multiply Eq. 2.5 from the right with $\vec{A}^* \left\langle \vec{A}^* \vec{A} \right\rangle^{-1}$ and take advantage of the fact that $\vec{R}$ is orthogonal to space $\vec{A}$, and get the following

$$\frac{\partial\vec{\phi}}{\partial t} - i\vec{\Omega}\cdot\vec{\phi}(t) + \int_0^t \vec{M}(t-s)\cdot\vec{\phi}(s)ds = 0 \tag{2.8}$$

where $\vec{\phi}$ is now the normalized correlation function of $\vec{A}$. With a Laplace transform of the above equation, one can reduce Eq. 2.8 to the form

$$\left[z\vec{I} + \vec{\Omega} + \vec{M}\right]\vec{\phi}(z) = \chi \tag{2.9}$$

where $\chi \equiv \phi(t=0)$ represents the initial condition for Eq. 2.8.

We will now cease to discuss further the dynamic models to solve the above equations except to say that if one assumes linear-coupling of the dynamic equations and frequency independent transport coefficients, one'll get exponential relaxation of fluctuations.

2.3 Mode Coupling Theory

The power law long time relaxation tail observed in transport properties near critical points is regarded as at odds with the exponential relaxation in various dynamical models. In order to explain the discrepancy, Kawasaki (Kawasaki, 1966) introduced the idea of non-linear coupling of collective modes.

From Eq. 2.9, one can get for density correlation function $\phi(q,z)$,

$$\frac{\phi(q,z)}{z\phi(q,z)-1} = z + im^L(q,z) \tag{2.10}$$

where the memory function $m^L(q,z)$ has two contributions (Bengtzelius et al., 1984),

$$m^L(q,z) = m_0^L(q) + \int_0^\infty dt e^{izt} \tilde{m}^L(q,t) \tag{2.11}$$

with $m_0^L(q)$ as the contribution from uncorrelated binary collision, and $\tilde{m}^L(q,t)$ as that from ring and repeated-ring type of correlated collisions.

$\tilde{m}^L(q,t)$ can be obtained as

$$\tilde{m}^L(q,t) = \frac{n}{2m\beta} \int \frac{d\vec{k}}{(2\pi)^3} \left[V_L(\vec{q},\vec{k})\right]^2 S(k_1)S(k)\phi(k_1,t)\phi(k,t) \tag{2.12}$$

with S being the static structure factor, $\vec{k}_1 = \vec{q} - \vec{k}$ and the function $V_L(\vec{q},\vec{k})$ defined as

$$V_L(\vec{q},\vec{k}) = (\hat{\vec{q}}\cdot\vec{k})c(k) + (\hat{\vec{q}}\cdot\vec{k}_1)c(k_1) \tag{2.13}$$

One essential assumption of MCT is that after a certain time frame, the correlation function does not change much.

$$\phi(q,t) = f_q + (1 - f_q)\phi_\nu(q,t) \tag{2.14}$$

where f_q is the non-decaying part of $\phi(q,t)$ at long time limit and $\phi_\nu(q,t)$ goes to zero at long times. The f_q's, or the so-called non-ergodicity parameters, are determined from the following coupled non-linear equations:

$$\frac{f_q}{1 - f_q} = \frac{1}{\Omega_q}\tilde{m}^L(q, t \to \infty) \equiv \mathcal{H}_q\left[f_k\right] \tag{2.15}$$

where the functional $\mathcal{H}_q$ are defined as proportional to the long time limit of $\tilde{m}^L(q,t)$ in Eq. 2.12. The necessary input for Eq. 2.15 is the static structure factor $S(q)$. At low densities, there are only trivial solutions to Eq. 2.15. At a critical density, a non-zero set of f_q will be obtained simultaneously. The temperature point that corresponds to such a critical density is called critical temperature T_c. Below T_c, the system will enter the non-ergodic state and have a non-vanishing ergodicity parameter.

After solving the self-consistent mode coupling equations, one is able to predict the decay of the density correlation function $\phi_q(t)$. First, $\phi_q(t)$ decays to a plateau value f_q,

$$\phi_q(t) = f_q^c + \tilde{h}_q(\tau_\beta/t)^a \qquad t_0 \ll t \ll \tau_\beta \tag{2.16}$$

where $t_0 = 1/\Omega_q$ is the microscopic time scale, $\tau_\beta = Ct_0\left|\epsilon\right|^{-1/2a}$ with C as a constant calculable from the mode coupling equations, $\epsilon = (T_c - T)/T_c$. Above the critical density, or below T_c, this is the only relaxation step. Below the critical density, or above T_c, the power-law relaxation crosses over to von-Schweidler relaxation (von Schweidler, 1907),

$$\phi_q(t) = f_q^c - \tilde{h}_q(t/\tau_\alpha)^b \qquad \tau_\beta \ll t \ll \tau_\alpha \tag{2.17}$$

where

$$\tau_\alpha = CT_0 \left|\epsilon\right|^{-\gamma} \tag{2.18}$$

with $\gamma = 1/(2a+2b)$, a and b as solutions to the following equation

$$\lambda = \Gamma^2(1-a)/\Gamma(1-2a) = \Gamma^2(1+b)/\Gamma(1+2b) \qquad 0 \leqslant a < \frac{1}{2}, 0 < b \leqslant 1 \tag{2.19}$$

where Γ stands for the normal gamma functions, λ $(1/2 < \lambda < 1)$ is a parameter defined in (Götze, 1984; Götze, 1985). Here we get one important equation for the time scale of α relaxation, namely, the power law dependence: $\tau_\alpha \propto (T - T_c)^{-1/\gamma}$.

Another aspect of import MCT predictions deals with the non-ergodicity parameter, or the effective Debye-Waller factor:

$$f_q = \begin{cases} f_q^c + \tilde{h}_q\sqrt{|\epsilon|} + O(\epsilon) & T < T_c \\ f_q^c + O(\epsilon) & T > T_c \end{cases} \tag{2.20}$$

Eq. 2.20 essentially predicts a cusp behavior for the non-ergodicity parameter: for $T > T_c$, f_q changes very little; as soon as temperature goes down below critical temperature T_c, the amplitude of effective Debye-Waller factor increase dramatically, or in other words, the amplitude of the vibrational motion decrease dramatically.

2.4 The Implications of Mode Coupling Theory

For a review on MCT, the reader is invited to (Götze and Sjögren, 1992) and references therein. Here we just summarize the following assumptions or implications of MCT:

- No structual singularity. This is a general assumption of MCT. There are experimental and simulation evidences to support this, and so far, there is no evidence against it.

- Equilibrium dynamics, homogeneity. MCT supposes that the supercooled liquid is homogeneous and in thermal equilibrium.

- Multi-step relaxation. MCT predict a multi-step relaxation: first a ballistic critical power law relaxation to a plateau f_q^c; around f_q^c, the density correlation function follows von-Schweidler law; at the long time, the von-Schweidler law crosses over to stretched exponential relaxation.

- Intrinsic non-exponential relaxation. The non-exponentiality is an intrinsic property of the relaxation behavior according to MCT, but not a sum of different exponential relaxation due to heterogeneity.

- Cage effect. Physically the multi-step relaxation corresponds well to the cage effect. In the densely packed liquid, atoms would be trapped in a cage before undergoes cage opening and diffusion. In this picture the power law initial relaxation is due to the cage rattling process. Later relaxation behavior corresponds to cage callapsing.

- Ergodic–non-ergodic transition above T_g. Freezing happens above T_g.

- Hopping process in extended MCT. If we include the "hopping" process (current term on top of density term in Eq. 2.12), which is not considered in the ideal MCT, the ergodicity can be restored even at temperatures below T_c. MCT's explanation to T_g: experimentally observed freezing that happens at a relaxation timescale comparable to the time scale of experimental observations.

CHAPTER 3

NMR STUDY ON THE FAST PROCESSES

Before we start the discussion of how NMR can detect dynamics in liquids and glasses, I'll present in the following section (Section 3.1) the physical background of NMR spectroscopy in order to give the reader some familiarity with NMR and pave the way for later discussions in this dissertation where a series of other NMR techniques are used. For advanced treatment of this topic, the reader is encouraged to consult standard texts in this area, namely two books authored by Abragam and Slichter (Slichter, 1990; Abragam, 1961). Ernst also presented a very clear summary of the density matrix formalism (Ernst et al., 1990).

3.1 Basics of NMR Spectroscopy

Assume that we have a static magnetic field, now normally generated by a superconducting magnet, that is much stronger than internal magnetic field produced by nuclear spins inside a bulk sample of matter. This assumption makes our treatment a lot simpler, because we can consider the main interaction between external magnetic field and the nuclear spins first, and later the internal interactions as a perturbation. According

to quantum mechanics, any measurement involving interaction with the spin system will force the spin angular momenta to assume quantized projections along the external magnetic field direction. Now we only consider spins that have two eigenstates of spin angular momenta, or two projections along the external magnetic field (spin-up and spin-down). We call them spin 1/2. Later in the dissertation we'll extend our discussion to spin 3/2 and spin 5/2 cases.

The magnetic moment that a nuclear spin possess is

$$\vec{\mu} = \gamma \vec{I} \tag{3.1}$$

$\vec{I}$ is the spin angular momentum and γ is normally called the γ ratio. The interaction between such a magnetic moment and external magnetic field is called Zeeman interaction, with an interaction energy (Hamiltonian) being:

$$\hat{H} = -\vec{\mu}\vec{B} = -\gamma \vec{I}\vec{B} \tag{3.2}$$

Thus previously a single energy state now separates into multiple energy states. In a bulk sample, at temperature T, the spin population difference between these states provides a macroscopic magnetization of the spin system, which in Boltzmann distribution is given by:

$$M = N\gamma\hbar \frac{\sum_{m=-I}^{I} \exp(\gamma\hbar m B_0/kT)}{\sum_{m=-I}^{I} \exp(\gamma\hbar m B_0/kT)} \tag{3.3}$$

where N is total number of nuclear spins, $\hbar$ is Planck's constant, $\vec{I} = \hbar I$ is the spin angular momentum. Since usually it holds that $\gamma\hbar m B_0 \ll 1$ owing to the small value

of $\hbar$, equation 3.3 now simplifies to

$$M = \frac{N\gamma^2\hbar^2 I(I+1)}{3kT} B_0 = \chi_0 B_0 \tag{3.4}$$

χ_0 is called static nuclear susceptibility. At room temperature, $\chi_0 \sim 10^{-10}$ due to the very small eigenstate population difference which in turn is due to the small energy difference between the two states compared with kT. The energy splitting, according to Eq. 3.2, equals to the following

$$\hbar\omega_0 = E_{-1/2} - E_{1/2} = \gamma\hbar B_0 \tag{3.5}$$

Now if one applies an electromagnetic excitation with a frequency $\nu = \omega_0/2\pi$, one would be able to to create resonance phenomenon, and it's readily call nuclear magnetic resonance. ν is called Larmor frequency and it is usually in the radio frequency range.

The majority of magnetic resonance experiments are nowadays done with radio frequency (rf) pulses. Figure 3.1 illustrates the interaction between nuclear spin system with a rf pulse in resonance. One has to keep in mind that such an illustration is a classical picture of spin 1/2 system. In Figure 3.1(a), when we turn on the transmitter, the sinusoidal rf current in the transmitter coil generates a linearly polarized magnetic field $2H_1\cos(\omega_0 t)$. This linear motion can be decomposed into two counter rotating vectors of magnitude H_1 as show in Figure 3.1(b). In a frame rotating at ω_0 (Figure 3.1(c)), one of the rotating fields will have the right frequency and appears to be stationary. (The other one will be neglected because it is $2\omega_0$ away from the right frequency and has little interaction with the spin system.) It can be proved that in order for the physics to valid in rotating frame, a hypothetical $-B_0$ has to be added to the system. Therefore the magnetization $\vec{M}$ only sees the stationary H_1 field and precesses around it at angular speed $\omega_1 = \gamma H_1$ (Figure 3.1(d)). When we turn off the

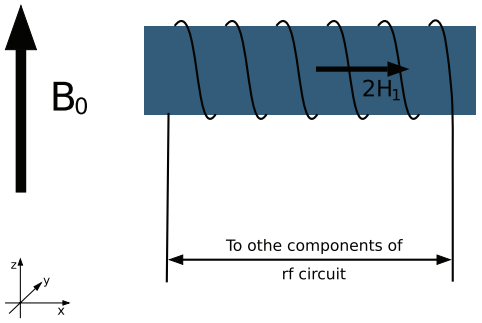

(a) Oscillating H_1 field generated by coil rf current. H_1 is perpenticular to external magnetic field B_0.

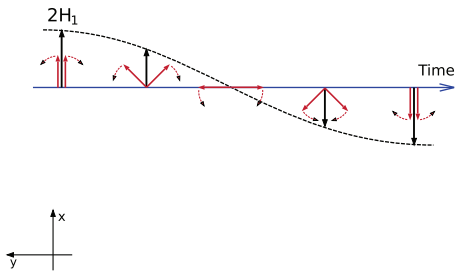

(b) Decomposition of H_1 into two fields rotating in opposite direction.

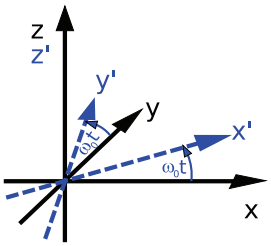

(c) Rotating frame.

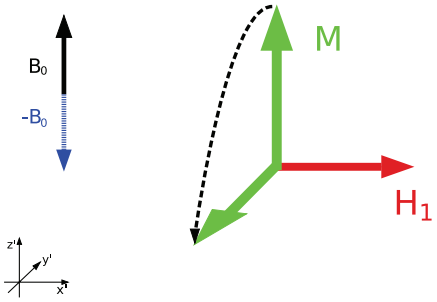

(d) Magnetization in rotating frame.

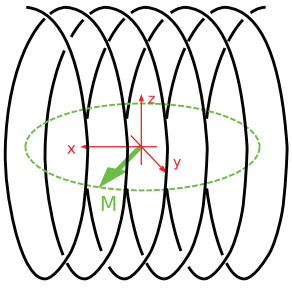

(e) Pulse off; precessing magnetization in laboratory frame, which induces signal detectable by coil.

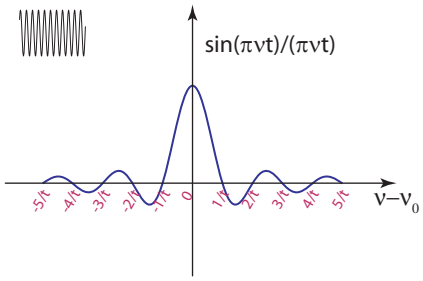

(f) Excitation profile of a pulse of length t.

Figure 3.1: Illustration of the effect of a radio frequency pulse.

transmitter, in the laboratory frame, the magnetization will precess around external magnetic field B_0, and will induce signal in the coil, which is call free induction decay, or FID (Figure 3.1(e)). Later in this dissertation it will become clear that in real system due to internal interactions the resonance frequency will have a distribution; nevertheless, rf pulses can cover all the resonance frequencies because of the excitation profile shown in Figure 3.1(f). The width of the central peak in Figure 3.1(f) is on the order of $1/t$, or well above 100KHz for most of the experiments.

The discussion above didn't include the internal interactions between the nucleus spins and the environment such as other nucleus spins or electron spins or the electric field gradient produced by other nuclei and electrons. Normally such internal interactions are sufficiently small compared to the main Zeeman interaction, so in quantum mechanics, we can treat them as a perturbation to the main Zeeman interaction, and the net effect is that the nucleus of interest would experience a small additional magnetic field due to interactions with the environment. One of such interactions in that between the nucleus spin and the unpaired electrons in a metal. We'll discuss this further in the following section.

3.2 NMR on Metallic Sample: Knight Shift

The Knight shift is named after Professor Walter Knight, who first observed the phenomenon. What he found was that the resonance frequency of ^{63}Cu in metallic copper was 0.23% higher than that in CuCl. Since this shift is an order of magnitude higher than normal chemical shifts, it is reasonable to attribute it to effects in the metal. Here we are also studying nuclei in a metallic sample, so the phenomenon of Knight shift is something we must consider. As we shall see, the correct explanation of the Knight shift involves considering the field the nucleus experiences as a result of the interaction

with un-paired conduction electrons through the s-state hyperfine coupling.

We consider a system of nuclear moments and electrons. The hyperfine coupling between the nuclear spins and electron spins is so weak that we can treat it as a perturbation in terms of the electrons and nuclear spins. We further consider the interactions between electrons are non-existent or at least so weak that we don't need to consider it for the first step of approximation. Therefore, we can describe the system with a Hamiltonian:

$$\mathcal{H} = \mathcal{H}_e + \mathcal{H}_n + \mathcal{H}_{en} \tag{3.6}$$

where $\mathcal{H}_e$ describes the weakly interacting electrons, $\mathcal{H}_n$ describes the system of nuclear spins and includes the Zeeman energy and nuclear dipolar couplings, $\mathcal{H}_{en}$ describes the interaction between electrons and nuclear spins and is something of our interest here.

Now we'll just write down the basic interaction assumptions and the results. For detailed deduction, please refer to the texts mentioned above (Abragam, 1961; Slichter, 1990).

For simplicity, the coupling between electrons and nuclear spins is assumed to be a δ-function:

$$\mathcal{H}_{en} = \frac{8\pi}{3}\gamma_e\gamma_n\hbar^2 \sum_{j,l} \mathbf{I}_j \cdot \mathbf{S}_l \delta(\vec{r_l} - \vec{R_j}) \tag{3.7}$$

where $\vec{r_l}$ is the position vector of the lth electron, and $\vec{R_j}$ is that of jth nucleus, $\mathbf{I}$ and $\mathbf{S}$ are the nuclear spin and electron angular momentum quantum numbers respectively, $\gamma_e = 2\mu_B/\hbar = 1.76 \times 10^{11}$ Hz/Tesla is the electron gyromagnetic ratio, γ_n is the gyromagnetic ratio of the nucleus, $h = 2\pi\hbar$ is the usual Planck constant.

This type of interaction can be shown to be equivalent to adding an extra magnetic field ΔH on top of the external field B_0, and the Knight shift K is finally given by:

$$K = \frac{\Delta H}{B_0} = \frac{8\pi}{3}\left\langle \left|\psi_{\vec{k}}(0)\right|^2_{E_F} \right\rangle \chi_e^s \tag{3.8}$$

where $\left|\psi_{\vec{k}}(0)\right|^2_{E_F}$ is the electron wave function at the Fermi level at the nucleus averaged over all states, χ_e^s is the electron paramagnetic susceptibility.

The coupling between nuclear spins and electrons not only gives rise to giant Knight shift, but also provides a mechanism for the nucleus to relax to lower energy state. In a metal, relaxation due to Knight shift is normally the dominant relaxation mechanism. The rate of this relaxation process is given in "Korringa relation" (Korringa, 1950):

$$T_1 K^2 = \frac{\hbar}{4\pi k_B T} \frac{\gamma_e^2}{\gamma_n^2} \tag{3.9}$$

where T is the temperature, k_B is the Boltzmann constant.

If we includes the effect of electron-electron interaction, Eq. 3.9 becomes

$$T_1 K^2 T = \frac{\hbar}{4\pi k} \frac{\gamma_e^2}{\gamma_n^2} f \tag{3.10}$$

where f is called the "enhancement factor".

3.3 Experimental Details

3.3.1 Sample Preparation

Amorphous samples of $Pd_{43}Ni_{10}Cu_{27}P_{20}$ were prepared by inductively melting the pure metals and elemental phosphorus in quartz tubes for 20min at 1200 K followed by water quenching. The following ingot materials were used for induction melting: Pd, 3-6mm pieces, Cerac Incorporated, purity of 99.95%; Ni, rod, Alfa Aesar, purity of 99.999%; Cu, shots, Alfa Aesar, purity of 99.9999%; P, lump, purity of 99.999%. Subsequently, samples were processed in B_2O_3 by slowly heating to 1200K and cooling back down to room temperature several times. The B_2O_3 used was previously dehydrated for 3h at 1200 K. Samples of $Pd_{40}Ni_{40}P_{20}$ and $Pt_{43}Ni_{10}Cu_{27}P_{20}$ were prepared the same way,

except that for $Pt_{43}Ni_{10}Cu_{27}P_{20}$, ingots of Pt with a purity of 99.95 % was used.

Small particles of amorphous samples were used in NMR measurement. They are vacuum sealed in quartz tubes, with B_2O_3 as flux and Al_2O_3 powders as separators. The weight ratio between metallic glass sample, B_2O_3 and Al_2O_3 is about 40 : 30 : 30. Al_2O_3 was also dehydrated at 1200 K for several hours.

3.3.2 High Temperature NMR

In order to get to the liquid state of the metallic glasses, a high temperature NMR probe is needed. High temperature probes have been built previously to study quasi-crystals and other metallic glass systems. The probe shown in Figure 3.2 is one of the high temperature probes previously built, but with slight later improvements, mainly on the bottom plate so that water cooling becomes possible. The heating wire inside the water jacket is winded in a way that the magnetic field generated by static heating current would be minimal. The heating wire and thermal couple wire are further shielded by molybdenum foils to minimize noise input to the coil. Temperature calibration of the probe was done by mimicking real experimental conditions and putting another thermocouple in the sample region to get a correspondence between temperatures in the heating zone and sample zone. Calibration was further verified by NMR measurement of ^{27}Al up to melting temperature of Al (660 ^{o}C), and the error of the calibration is confirmed to be within 5 K.

3.3.3 Thermal Properties of $Pd_{43}Cu_{27}Ni_{10}P_{20}$ Sample

Very detailed thermal characterization was performed previously for $Pd_{43}Ni_{10}Cu_{27}P_{20}$ system (Schroers et al., 2002). Here some of the related results are presented. An understanding of the thermal properties not only forms the basis of the experiments during the NMR study, but also shed light on the problems that could be of interest

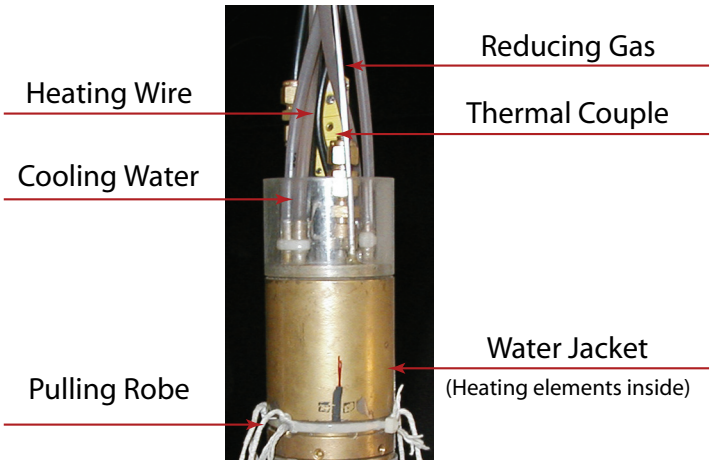

(a) Heating cap

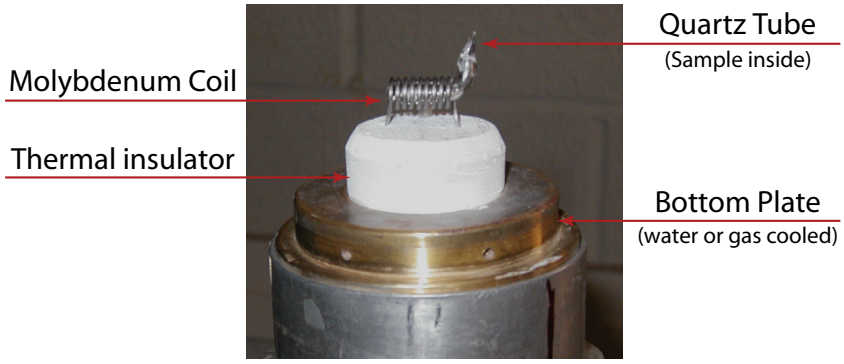

(b) Bottom Plate

Figure 3.2: High temperature probe.

and guided the design of the experiment, and make important contribution to the interpretation of the final experimental results.

The Differential Scanning Calorimetry (DSC) curve of Figure 3.3 clearly shows the characteristics of a glass. There is a step in heat flow which corresponds to the glass transition temperature. At about 670 K the sample begin to crystallize, and above 870 K melting of all crystalline phases finishes and we mark 870 K as the liquidus temperature T_{liq}. These important temperature points serve as guidance for NMR study that will be discussed later. In Figure 3.4 a Time-Temperature-Transformation (TTT) diagram is shown. At high temperature in the supercooled state, the driving force for crystallization, or the difference in free energy between the liquid state and the crystalline state, is small, so the waiting time before the sample crystallizes is long. At low temperature, although the driving force is getting big, the kinetics of the system is slow, so the atoms take a long time to move to the low energy crystalline state. That's why we see a typical nose shape in the TTT diagram. The nose temperature is about 700 K, and at 700 K it takes about 200 sec for the sample to crystallize. That explains why later in this dissertation there is a small temperature gap in the NMR study of this sample. There isn't enough time for the sample stabilize in temperature and us afterwards to finish NMR data acquisition around nose temperature.

A very important discovery in Ref. (Schroers et al., 2002) is the observation of a transition in crystallization mechanism at about 718 K (Figure 3.5). In Figure 3.5(a) and 3.5(b) each sharp peak is a crystallization event of a single particle. In Figure 3.5(c) and 3.5(d) such sharp peaks disappear and it looks as if particles are crystallizing collectively, all in the same way, and the crystallization is not distinguishable from that of one large sample. Such a transition in crystallization behavior suggests an underlying more fundamental change in dynamics or thermodynamics, and we would like to use NMR to probe such fundamental changes and compare the results with theoretical

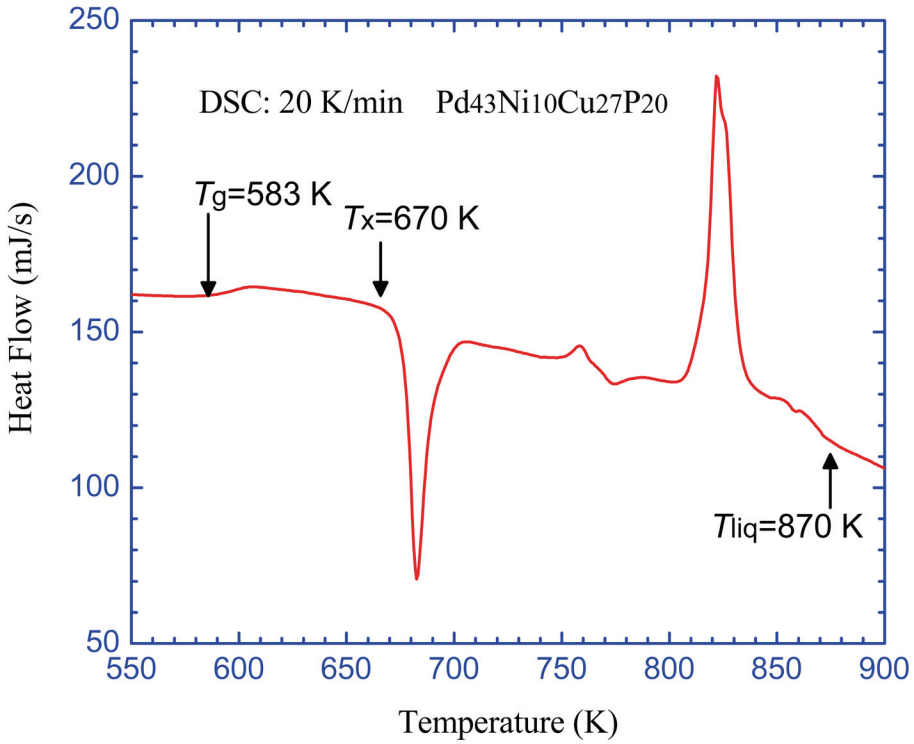

Figure 3.3: DSC curve of $Pd_{43}Ni_{10}Cu_{27}P_{20}$ metallic glass sample at a heating rate of 20 K/min. T_g and liquidus temperature are identified as 583 K and 870 K, respetively. The onset of crystallization is at 670 K.

thinking.

3.4 Results and Analysis

3.4.1 Temperature Dependence of Knight Shift

Figure 3.6 shows the room temperature (RT) ^{31}P NMR spectra of the glassy $Pd_{43}Ni_{10}$-$Cu_{27}P_{10}$ sample, and a crystalline sample obtained upon crystallization of the supercooled liquid at 767 K. A ^{31}P spectrum of the liquid taken at 1057 K is also shown in Figure 3.6. The RT spectrum of the glassy state is broad since the chemical environment is different for the same kind of nuclei in such an amorphous system, and the

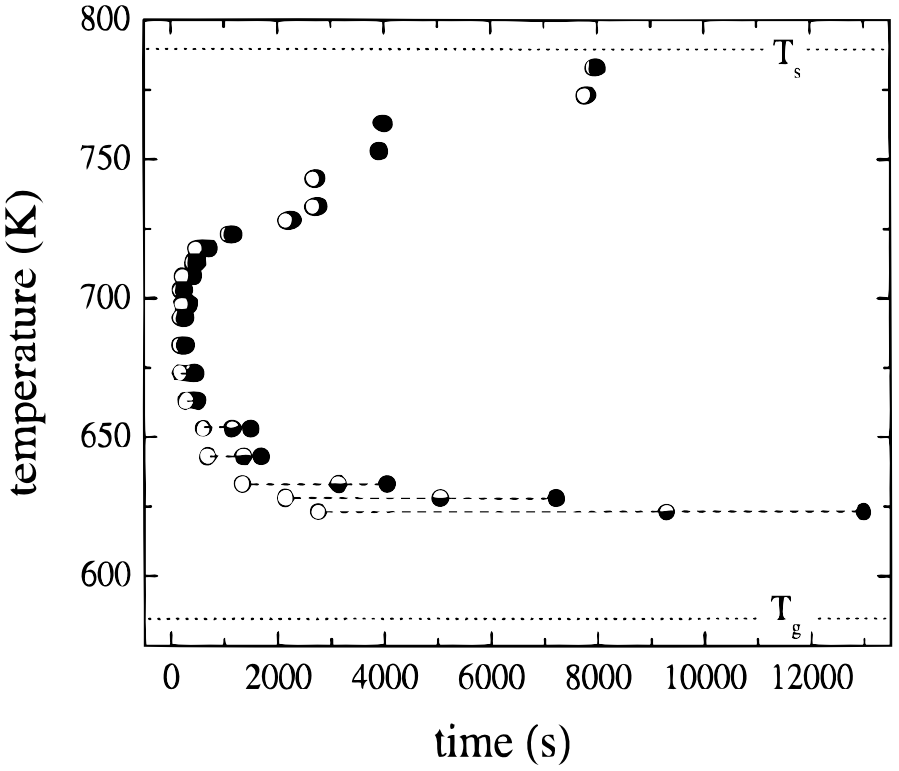

Figure 3.4: Time-temperature-transformation diagram for $Pd_{43}Ni_{10}Cu_{27}P_{20}$. In the diagram, the time to reach 1% (open circle), 50% (half filled circle), 100% (solid circle) is shown as a functin of temperature. At nose temperature (˜700 K) the time for the sample to remain in the supercooled liquid state is about 2-3 minutes. Adapted from (Schroers et al., 2002)

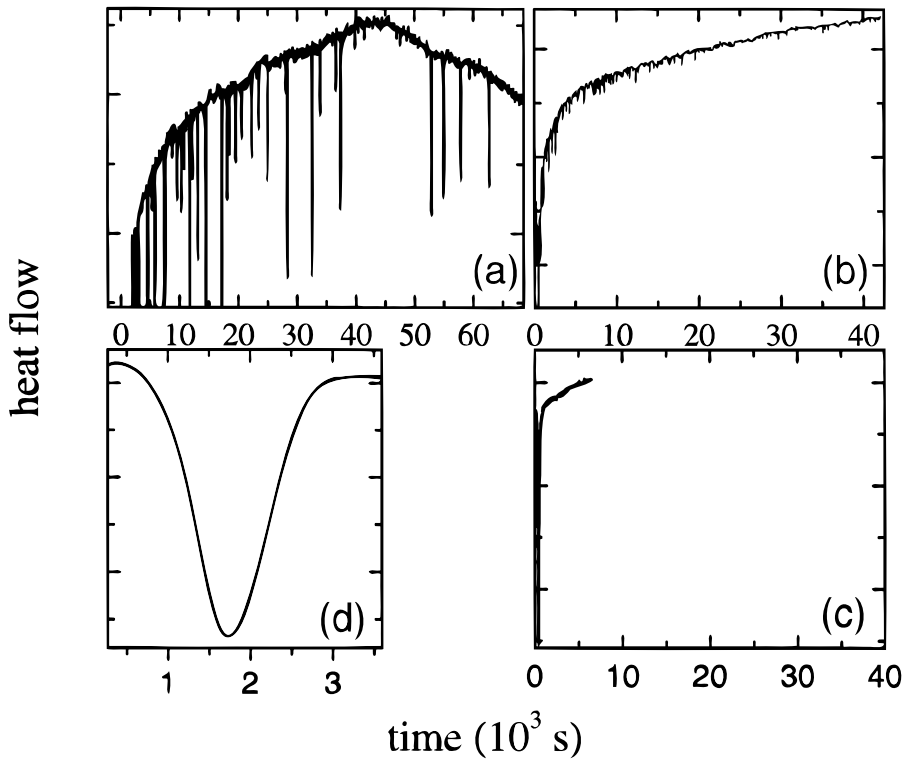

Figure 3.5: Isothermal DSC thermograms of $Pd_{43}Ni_{10}Cu_{27}P_{20}$ on powder sample containing about 300 particles with diameters between 100 and 350 μm. (a)753 K, (b)723K, (c)718K, (d)643K. Between 723 K and 718 K there's a change in crystallization mechanism. At tempertatures below 718 K crystallization occurs simultaneously in all particles. Adapted from (Schroers et al., 2002)

projected local magnetic field B_{local} along the external magnetic field direction varies with $\vec{R}_i$ from site to site. However, the ensemble average of B_{local} is represented by an average shift K of the spectrum given by the first moment of the spectrum (Abragam, 1961). The liquid line is very narrow, as expected from motional narrowing effect, the theory of which will be described in section 4.2.1. From Figure 3.8 we can see that at temperatures above 740 K, the shape of ^{31}P spectra doesn't change much. At temperatures below 740 K, the spectra starts broaden upon further cooling. After cooling down below T_g, however, the FWHM of the spectra changes very little again (Figure 3.9). From Figure 3.9, we see that there's dramatic change of dynamics at temperatures between 583 K (T_g) and 740 K. In section 4.2, we shall take advantage of this drastic change of ^{31}P line shape at this temperature range to quantitatively study the P atom hopping rates, or, the α relaxation process in this temperature region.

Apart from the shape or FWHM of the spectra, there's another notable difference in liquid and glassy state of the spectra, namely, the difference in Knight shift. The Knight shift jumps from about 1500 ppm at RT to about 2000 ppm at 1057 K, a huge and very unusual change of shift with temperature. This feature is manifested even clearer in Figure 3.7, where we plot ^{31}P spectra at various temperatures. We studied the temperature dependence of Knight shift more systematically, and plot the Knight shift as a function of temperature of the amorphous solid, liquid, and crystallized sample in Figure 3.8. The Knight shift K of samples in amorphous state shows a linear temperature dependence both above 700 K, with a slope of 0.75 ppm/K, and below T_g, with a slope of 0.27 ppm/K. Data above 700 K were obtained by first heating the sample above T_{liq} and then cool directly to T in-situ for NMR measurement. The same results were obtained by cooling (or heating) directly from one $T < T_{\text{liq}}$ to another $T < T_{\text{liq}}$ (lower or higher) without going back to $T > T_{\text{liq}}$ in the absence of crystallization. Data below 700 K were obtained by heating the glassy sample from RT to the measurement

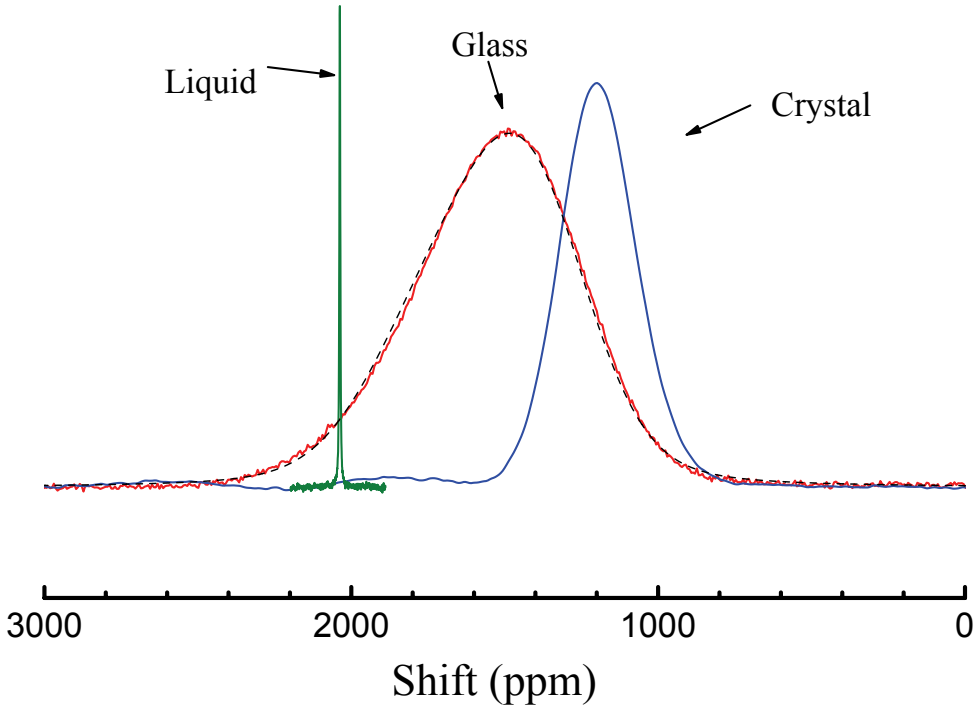

Figure 3.6: ^{31}P NMR spectra of the glassy and crystallized samples of $Pd_{43}Ni_{10}Cu_{27}P_{20}$ at RT, detected with Hahn echo sequence, and the spectrum of the liquid state taken at 1057 K. The shift reference is ^{31}P in 85 % H_3PO_4. The dashed line is a powder pattern fit using a CSA parameter $\delta_{\text{aniso}} = 370$ ppm, $\eta = 0$, and a 500 ppm line broadening.

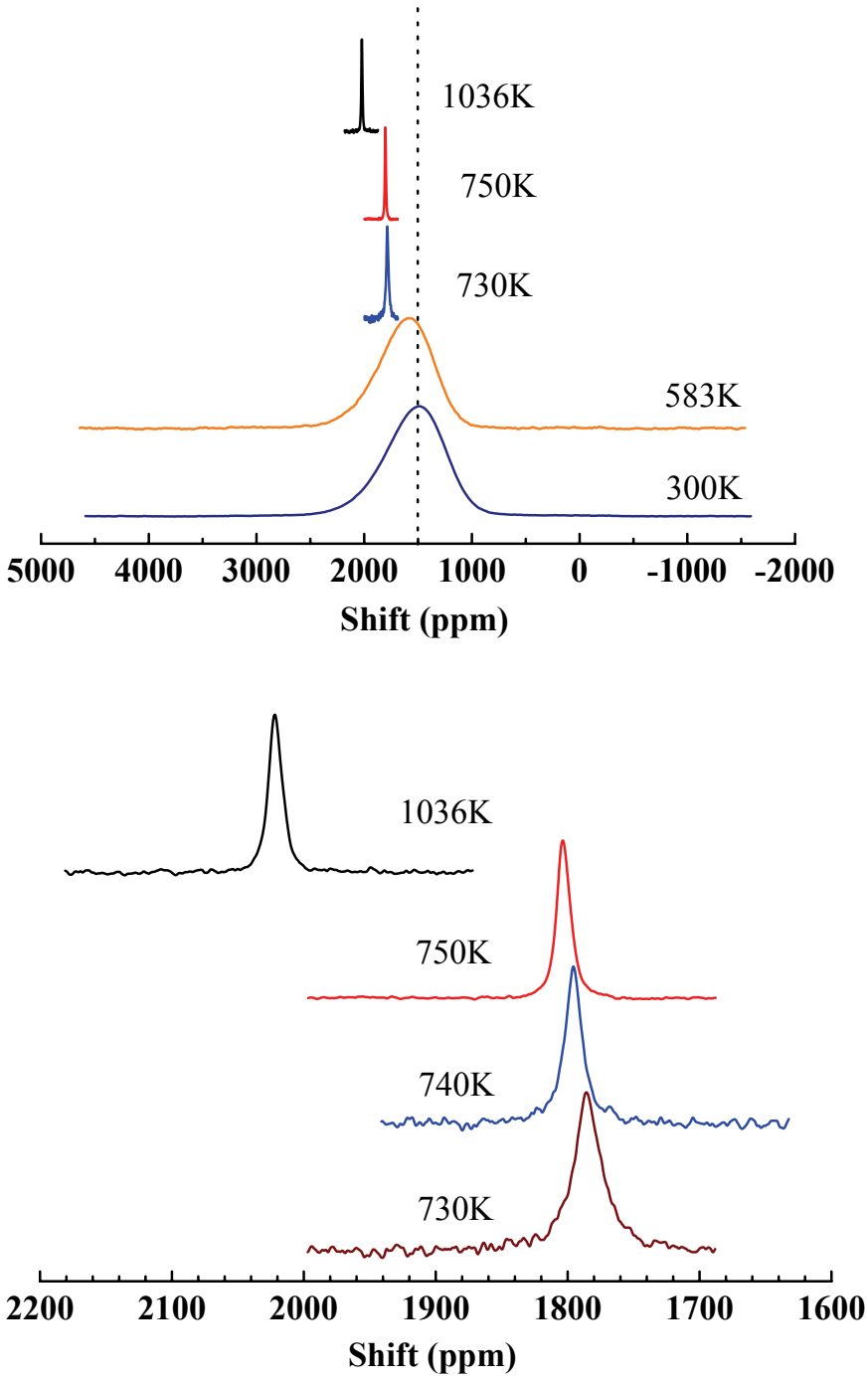

Figure 3.7: ^{31}P spectra in $Pd_{43}Ni_{10}Cu_{27}P_{20}$ at various temperatures that presents ^{31}P Knight shift and line shape at a function of temperauture. During the time all the spectra were taken, the sample remained amorphous.

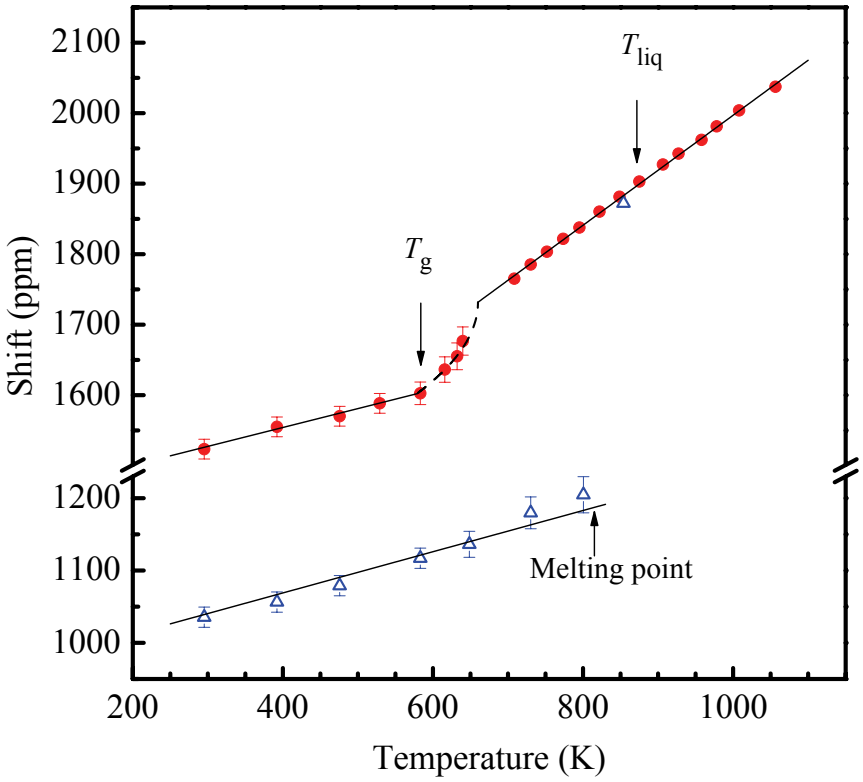

Figure 3.8: The average shift K of ^{31}P in $Pd_{43}Ni_{10}Cu_{27}P_{20}$ measured at 9.4 Tesla versus T in the liquid, supercooled liquid, and the glassy state (solid circle) as well as that of the crystallized sample (open triangle). The error bar in the liquid and supercooled liquid states above 700 K is about the same as the size of the symbol. The liquidus temperature T_{liq}, the glass transition temperature, and the melting temperature of the crystalline phase are indicated. The dashed line is a fit using Eq. 3.12 with $T_c = 660$ K. The shift of the crystalline sample after melting is slightly lower than that of the supercooled liquid because homogeneous composition can only be restored after heating above T_{liq}.

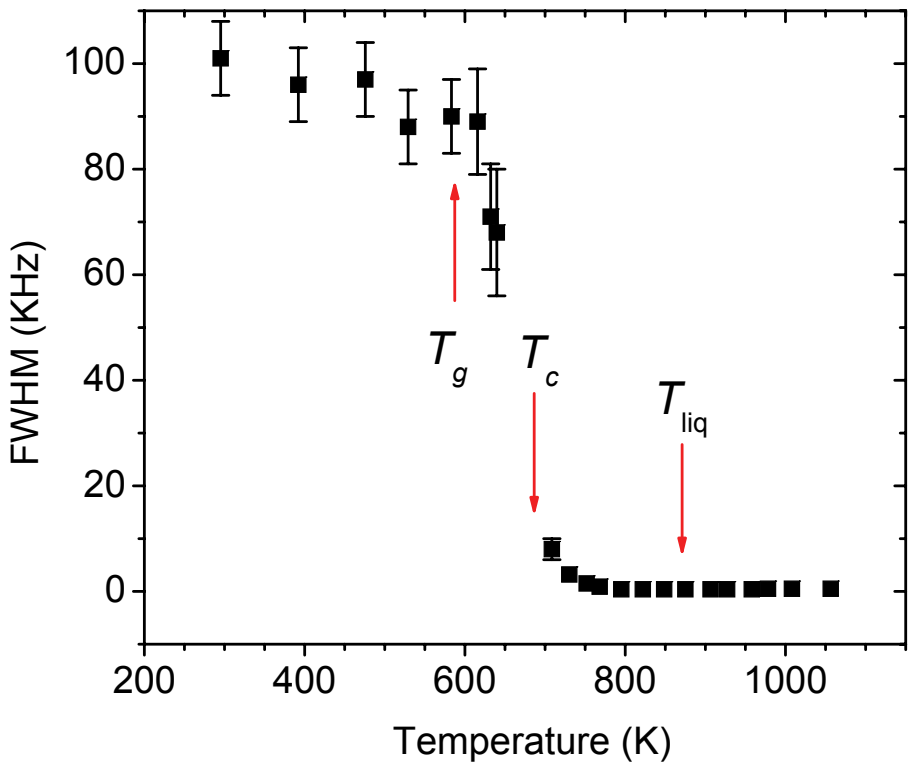

Figure 3.9: FWHM of ^{31}P spectra as a function of temperature for sample $Pd_{43}Ni_{10}Cu_{27}P_{20}$. The error bar above 730 K is about or smaller than the size of the symbol.

temperature. Same results were obtained by direct in-situ cooling from the melt to the measurement temperature. No time dependence of K was observed at any temperature.

3.4.2 Reason for Temperature Dependence of Knight Shift

According to Korringa relation (Eq. 3.10), $T_1TK^2 = \hbar\gamma_e^2 f/(4\pi k_B\gamma_n^2) = 1.6 \times 10^{-6} f$ for ^{31}P if we plug in the gyromagnetic ratio of ^{31}P. Figure 3.10 shows the measured T_1TK^2. The measured T_1 is the same at 9.4 and 4.7 Tesla. As expected from Eq. 3.10, T_1TK^2 remains constant at a value of 3.4×10^{-6} despite large T-dependence of K. The measured value of $f = 2.1$ implies a certain degree of electron-electron interactions typically found in metals. The constant T_1TK^2 and the value of $f = 2.1$ are consistent with other NMR studies in similar systems where d-band contributions to T_1 and K are ruled out (Hines et al., 1980). Thus the T-dependence of K cannot be attributed to the d-band effect (Winter, 1971).

Contribution from volume expansion can also be excluded, based on the following estimation. We write down the following equation:

$$\left.\frac{\partial \ln K}{\partial T}\right|_P = \left.\frac{\partial \ln K}{\partial \ln V}\right|_T \left.\frac{\partial \ln V}{\partial T}\right|_P + \left.\frac{\partial \ln K}{\partial T}\right|_V \tag{3.11}$$

Here $(\partial \ln K/\partial T)_P$ is the T-dependence of Knight shift observed in our experiments, $(\partial \ln K/\partial \ln V)_T(\partial \ln V/\partial T)_P$ is change of Knight shift from volume expansion, and $(\partial \ln K/\partial T)_V$ is the explicit T-dependence of Knight shift held at constant volume. As a rough estimation, we have $(\partial \ln K/\partial T)_P = (\Delta K/K\Delta T)_P$, and $\Delta K/K$ is about 35% in Figure 3.8 from RT to 1000 K. For the first term on the right side of Eq. 3.11, $(\partial \ln K/\partial \ln V)_T$ 2/3 from theoretical consideration of Eq. 3.8; in practice, however, one can get a number from 0 to 1. It is very small nevertheless. $(\partial \ln V/\partial T)_P = (\Delta V/V\Delta T)_P$, and from RT to about 1000 K, $\Delta V/V$ is less than 5% (Lu et al., 2002).

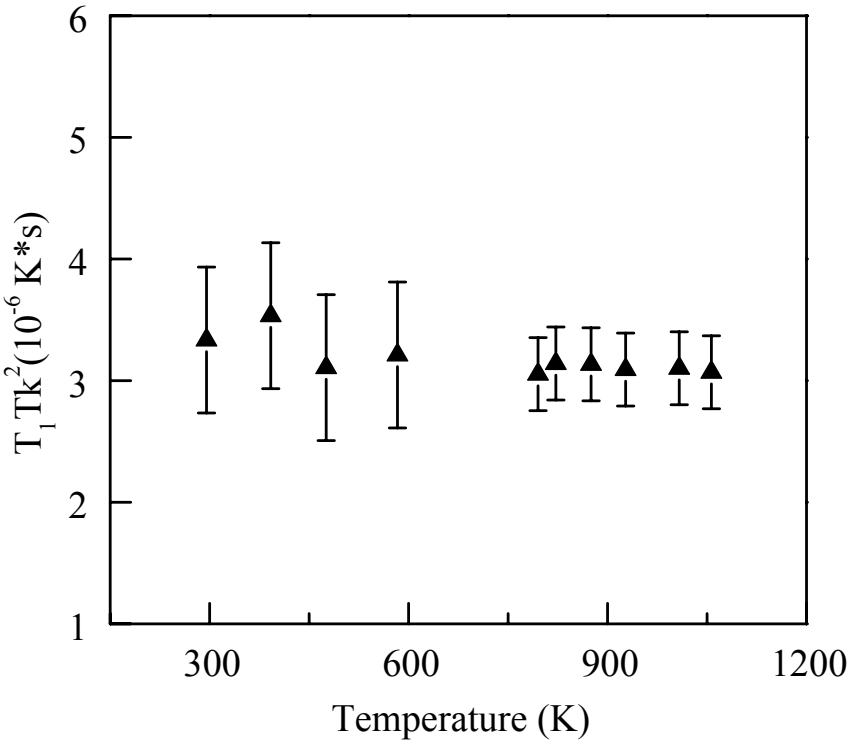

Figure 3.10: T_1TK^2 versus T for ^{31}P in $Pd_{43}Ni_{10}Cu_{27}P_{20}$ in glassy or liquid state.

So we can conclude the majority of observed T-dependence of Knight shift is coming from the second term in the right side of Eq. 3.11, i.e., the explicit one at constant volume. Also, in Ref. (Lu et al., 2002), there is no abrupt change of volume at any temperature except the change of slope at T_g, while in our data (Figure 3.8) there is a temperature region from T_g above that shows very interesting features. This also suggests that the T-dependence of Knight shift is from an mechanism other than pure volume effect.

3.4.3 Relation to MCT

A distribution of K caused by the distribution of local structures cannot be the single dominant factor for the linewidth of the RT spectrum. The high-frequency side of

the spectrum would relax much faster than the low-frequency side of the spectrum according to the Korringa relation if K variation dominates the linewidth. Observation shows that the relaxation rate is indistinguishable across the entire spectrum. The asymmetric lineshape of the RT spectrum is characteristic of the powder pattern of anisotropic shift mechanisms such as the chemical shift anisotropy (CSA). A fit using a CSA parameter $\delta_{\text{aniso}} = 370$ ppm and asymmetry parameter $\eta = 0$ is shown in Figure 3.6. Such CSA value is typical for ^{31}P spectra (Alam and Brow, 1998; Oyama et al., 2002). In the presence of motions, the linewidth is determined by the distribution of the time-averaged B_{local} experienced by each ^{31}P spin over the duration of the time-domain NMR signal (about 9 μs). Rapid exchange of chemical environment over this timescale will result in all spins experiencing the same time-averaged B_{local} leading to motional narrowing (section 4.2). However, motional narrowing should not lead to a different ensemble of local environments in the glassy and supercooled liquid state. Therefore, the time-averaged B_{local} is the same as the spatially averaged B_{local} obtained by first-moment calculation. Thus, diffusion does not lead to the T-dependence of K. Then, where does the change of K as a function of temperature come from? In order to understand that, we need to consider the influence of short-time dynamics on the shift of NMR spectra.

In a liquid of densely packed atoms, an atom is temporarily trapped inside the cage formed by neighboring atoms and undergoes vibrations and rattling before escaping the cage (Götze and Sjögren, 1992; Donth, 2001). Here the time dependence of the position vector $\vec{r}_i(t)$ of a given atom i can be described by $\vec{r}_i(t) = \vec{R}_i(t) + \vec{u}_i(t)$ where the rapidly changing $\vec{u}_i(t)$ describes local motions with time average $\langle \vec{u}_i(t) \rangle = 0$ and the slowing varying $\vec{R}_i(t)$ describes the transition of the atom from one cage to another (Mezei, 1991). MCT, described in section 2.3, is consistent with this picture. MCT predicts that $\phi(q,t)$, the correlation function of density fluctuations with wave number

q, undergoes two-step relaxation process—the fast β relaxation and the α relaxation (Götze and Sjögren, 1992; Donth, 2001). An important prediction of the MCT is the T dependence of $\vec{u}_i$ associated with the fast β relaxation (Götze and Sjögren, 1992; Donth, 2001). The effect of $\vec{u}_i$ contributes to the effective Debye-Waller factor $f_q = \exp(-2W)$. For MCT prediction of f_q as a function of temperature see Eq. 2.20. Experimentally the separation between the timescales of α and fast β relaxations in the temperature range of interest is often insufficient for model-independent determination of f_q by techniques relying on the time domain, such as neutron scattering (Mezei and Russina, 1999). So far, measurements of the effect of $\vec{u}_i$ have not revealed the critical behavior of f_q in metallic supercooled liquids (Meyer et al., 1996b; Meyer et al., 1996a; Meyer et al., 1998). Only recently, a diffusion measurement (Zöllmer et al., 2003), which measures the effect of $\vec{R}_i(t)$, showed changes of diffusion mechanisms in the supercooled region of $Pd_{43}Ni_{10}Cu_{27}P_{20}$. We'll discuss the effect of $\vec{R}_i(t)$ in section 4. Here we'll focus on the effect of $\vec{u}_i(t)$ on the Knight shift.

In contrast to $\vec{R}_i(t)$, $\vec{u}_i(t)$ cannot lead directly to efficient motional narrowing since it cannot cause a given ^{31}P spin to experience $\vec{B}_{\rm local}$ at different phosphorus sites. However, changes of $\vec{u}_i(t)$ with T will alter the ensemble of local fields. For instance, the closest possible atomic distance, which affects $\vec{B}_{\rm local}$, will change with the increase of the amplitude of $\vec{u}_i(t)$. Therefore, the T-dependence of $\vec{u}_i(t)$ could lead to the T-dependence of K in both the solid and liquid metals (Kasowski and Falicov, 1969; Kasowski, 1969; Ritter and Gardner, 1971; Benedek and Kushida, 1958). The electron wave function in Eq. 3.8 can be represented formally in the form of tight binding as $\psi(\vec{r}) = \psi_0(\vec{r}) + \sum \psi_i(\vec{r} - (\vec{R}_i + \vec{u}_i))$ where $\psi_o(\vec{r})$ represents orbitals of the atom at the origin associated with the observing nuclear spin and $\psi_i(\vec{r} - (\vec{R}_i + \vec{u}_i))$ represents orbitals of the neighbouring atom at $\vec{r}_i(t) = \vec{R}_i(t) + \vec{u}_i(t)$. With a Taylor expansion with respect to $\vec{u}_i$, it can be shown that the time average of $\left\langle |\psi(0)|^2 \right\rangle_{E_{\rm F}}$ can be expressed

as $\left\langle |\psi(0)|^2 \right\rangle_{E_F} = a_0 + a_1 \langle \vec{u}^2 \rangle$ if higher order terms of $\vec{u}_i$ are negligible. Here, a_0 and a_1 are constants and $\vec{u}$ is an average of $\vec{u}_i$'s of neighboring atoms. Other terms in Eq. 3.8 might also depend slightly on $\vec{u}$. Nevertheless, the lowest order term of $\vec{u}$ in K is still proportional to $\langle \vec{u}^2 \rangle$ because $\langle \vec{u}(t) \rangle = 0$. It is important to realize that, unlike the linewidth, K does not just probe motions within a certain timescale window, K represents the average $\vec{B}_{\text{local}}$ over all timescales including the static effect, namely, the distribution of local environments. This makes K particularly useful for detecting the onset of motions regardless of the range of timescales.

The linear T-dependence of the shift below 580 K shown in Figure 3.8 suggests that $\langle \vec{u}^2 \rangle \propto k_B T$ as expected from equipartition theorem for harmonic vibrations. The linear T-dependence of K in the crystalline sample exhibits the same slope as the glassy state. This demonstrates that the ^{31}P Knight shift in this type of alloys is sensitive to atomic vibrations. It is expected that K will be more sensitive to T above T_g since sound velocities and elastic moduli in metallic glasses decrease above T_g (Nishiyama et al., 2001; Pelletier et al., 2002). The observed linear T-dependence of K with a larger slope above 700 K indeed agrees with this expectation. The more interesting feature is the abrupt change of Knight from 700 K to about T_g. It indicates that some $\vec{u}_i(t)$-associated atomic motion present in the liquid-like region decreases rapidly upon cooling below 700 K. A candidate of such atomic motion is the fast β process associated with cage rattling. Since NMR is a local probe, it can be particularly sensitive to such atomic motion. In the ideal form of MCT, accomplishing the cusp behavior of f_q below T_c, $\sqrt{\langle u^2 \rangle}$ below T_c is given by:

$$\sqrt{\langle u^2 \rangle} = u_c \left(1 - \frac{1}{2} a \sqrt{(T_c - T)/T_c} \right) \tag{3.12}$$

where $a > 0$ and u_c is magnitude of rattling above T_c. A fit is shown in Figure 3.8 using Eq. 3.12 with $T_c = 660 \pm 10$ K assuming the shift is proportional to $\langle u^2 \rangle$ over

the entire temperature range. The T_c value agrees within the range of uncertainties with diffusion results (Zöllmer et al., 2003; Meyer et al., 1999). This by no means implies that the change is actually as abrupt as the curve in the fitting. The change might be gradual below 700 K and the effective T_c might be as high as 700 K. The detail is obscured by the lack of K data in that temperature range due to the fast crystallization. It is interesting to note that no difference in K was observed at any temperature by changing the quenching rate of the sample as well as by annealing. Samples vitrified under different cooling rate of 10^2 K/s and 10^4 K/s give exactly the same shift. Furthermore, annealing of a sample, originally obtained by quenching at a cooling rate of 10^2 K/s, for 700 minutes at 573 K in DSC does not depend on the residual structural relaxation with the employed quenching rate.

3.4.4 Other Metallic Glass Systems

Such a dramatic temperature dependence of Knight shift and a crossover at certain temperature region is present in other systems too. We've studied ^{31}P Knight shift in $Pd_{40}Cu_{40}P_{20}$ and $Pt_{43}Cu_{27}Ni_{10}P_{20}$ as a function of temperature (Figure 3.11 and Figure 3.12). We can see from Figure 3.11 and Figure 3.12 that both $Pd_{40}Cu_{40}P_{20}$ and $Pt_{43}Cu_{27}Ni_{10}P_{20}$ Knight shift scales linearly with temperature in liquid/supercooled liquid state and glassy state. The glass forming ability of the two systems are not as good as the previous one, $Pd_{43}Cu_{27}Ni_{10}P_{20}$, so there are wide gaps in the supercooled region where we cannot reach yet with NMR studies. But if we extend the linear relationship in the glass and supercooled liquid region, there's a discontinuity in Knight shift that one has to cross. So there must be a crossover region the same as that presented in Figure 3.8. We see from Figure 3.11 that although $Pd_{40}Ni_{40}P_{20}$ system has a larger Knight shift, the change of Knight shift is smaller for the temperature region measured. So how sensitive the Knight shift is with regard to temperature is

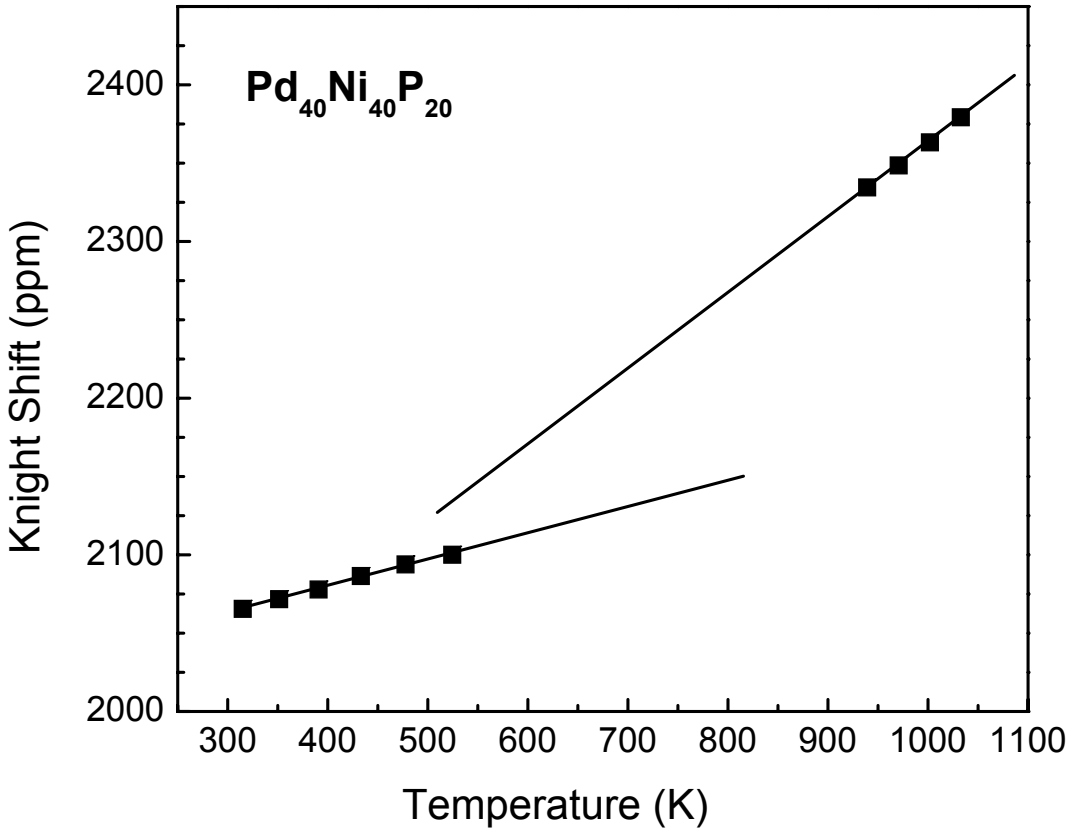

Figure 3.11: Knight Shift versus T in $Pd_{40}Cu_{40}P_{20}$ metallic glass forming system. During the time the data was taken, the sample remained amorphous. Lines on graph are guides to the eyes.

related to the electronic structure of the system, but the general feature seems to be universal, namely, the Knight shift is linearly temperature dependent for both above T_c and below T_g and there's a crossover between T_c and T_g. This feature must be related to the universal properties of the dynamics in supercooled liquid state and glasses. In section 4 the Knight shift of ^{63}Cu and ^{65}Cu is also linearly temperature dependent above T_c. This is consistent with our discussion here.

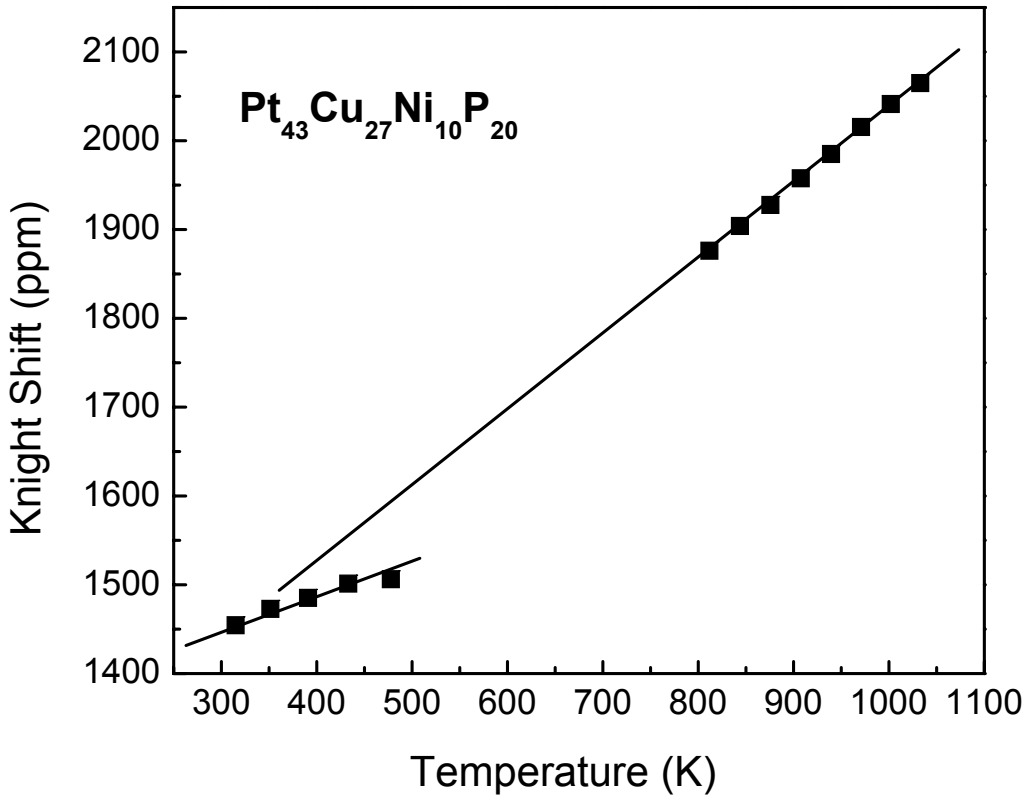

Figure 3.12: Knight Shift versus T in $Pt_{43}Cu_{27}Ni_{10}P_{20}$ metallic glass forming system. During the time the data was taken, the sample remained amorphous. Lines on graph are guides to the eyes.

3.4.5 Conclusion

NMR results reveals directly for the first time a qualitative change of local properties in a metallic supercooled liquid significantly above T_g. It is shown that in the supercooled liquid region of $Pd_{43}Ni_{10}Cu_{27}P_{20}$ certain local atomic motion changes rapidly between crossover temperature $T_c > T_g$ and a temperature very close to T_g. Above T_c, the mean-squared amplitude of local motions depends linearly on k_BT. This is also the case for temperatures between T_g and RT. The results show consistency with the MCT.

CHAPTER 4

NMR STUDY ON THE SLOW PROCESSES

4.1 Nuclear Quadrupolar Relaxation

Quadrupole interactions have long been recognized as something that can provide important information regarding the structure and dynamics in both the liquid and solid state of the matter. Probing nuclear spin relaxation caused by fluctuation of the electric field gradient (EFG) is a particular promising technique in liquid dynamics, which was successfully utilized to study protein dynamics, ionic motion, density and concentration dependence of chemical reaction. Such studies were also carried out in metallic liquids (Sholl, 1974; Gaskell and Woolfson, 1984; Marsden et al., 1980; Claridge et al., 1972; v. Hartrott et al., 1979). So far, however, a good general theory about NQR in metallic liquids is still lacking. Theory developed by Warren (William W. Warren, 1974) and Sholl (Sholl, 1974) suggests a $T^{-1/2}$ dependence of NQR rate for pure metals. For liquid alloys, a stronger temperature dependence and a larger value of NQR rate are usually observed. Extension of the theory to liquid alloys (Claridge et al., 1972; v. Hartrott et al., 1979) cannot fully account for the phenomena. Later on thermodynamical in-

fluences were raised to explain the discrepancy (Maxim et al., 1986; Ott et al., 1989). Correlation between NQR and theory of liquid dynamics are never fully explored and verified both in theory and experiments. Here through our study on temperature dependence of NQR of ^{63}Cu and ^{65}Cu in $Pd_{43}Ni_{10}Cu_{27}P_{20}$, we try to establish such a correlation, and support the theory of liquid dynamics by new experimental evidences.

4.1.1 Nuclear Quadrupolar Interaction and NMR

Here a background knowledge about the influence of nuclear quadrupolar interactions (NQI) on NMR spectroscopy will be presented. This information will also be very useful in the following chapter when we discuss the structural information that can be obtained by NMR, by exploiting the fact that quadrupolar nuclei are far more sensitive to structure and symmetry.

Nuclear Quadrupolar interaction is the interaction between nuclear magnetic moment and the electric field gradient (EFG) at the nuclei. We can obtain a Hamiltonian for quadrupole interactions by first considering the classical equivalence of the interaction energy E of a charge distribution of Density ρ with a electric potential V:

$$E = \int \rho(\vec{r})V(\vec{r})d\tau \tag{4.1}$$

One can do a Taylor's expansion regarding the origin of the nuclei:

$$V(\vec{r}) = V(0) + \sum_{\alpha} x_\alpha \left.\frac{\partial V}{\partial x_\alpha}\right|_{r=0} + \frac{1}{2!}\sum_{\alpha,\beta} x_\alpha x_\beta \left.\frac{\partial^2 V}{\partial x_\alpha x_\beta}\right|_{r=0} + \cdots \tag{4.2}$$

The third term is the so-called electrical quadrupole term and is of our interest here.

If one finds the principle axes such that

$$V_{\alpha\beta} \equiv \left.\frac{\partial^2 V}{\partial x_\alpha \partial x_\beta}\right|_{r=0} = 0 \qquad \text{if } \alpha \neq \beta \tag{4.3}$$

Moreover, V satisfies LaPlace's equation:

$$\bigtriangledown^2 V = 0 \tag{4.4}$$

Now it's easy to prove that

$$E^{(2)} = \frac{1}{6}\sum_{\alpha,\beta} V_{\alpha\beta} Q_{\alpha\beta} \tag{4.5}$$

with

$$Q_{\alpha\beta} = \int (3x_\alpha x_\beta - \delta_{\alpha\beta} r^2)\rho d\tau \tag{4.6}$$

When one replaces the classical ρ with a quantum mechanical operator $\hat{\rho}$, one can get the quadrupole Hamiltonian $\mathcal{H}_Q$:

$$\mathcal{H}_Q = \frac{1}{6}\sum_{\alpha,\beta} V_{\alpha\beta}\hat{Q}_{\alpha\beta} \tag{4.7}$$

with

$$\hat{Q}_{\alpha\beta} = e\sum_{k=\text{protons}} (3x_{\alpha k}x_{\beta k} - \delta_{\alpha\beta} r_k^2) \tag{4.8}$$

From Eq. 4.7 and Eq. 4.8 it seems that it's necessary to know the position of all the protons inside the nuclei, which is an unsolvable task. Fortunately, for an NMR spectropist, his only concern would be the resonance between eigenstates near the ground state, or the total angular momentum I and its $2I = 1$ components. In other words, we are only interested in the following matrix elements of the quadrupole operator:

$$\left\langle Im\eta \left| \hat{Q}_{\alpha\beta} \right| Im'\eta \right\rangle \tag{4.9}$$

with η being other quantum numbers not of our interest. These elements can be shown to obey the following form:

$$\left\langle Im\eta \left| \hat{Q}_{\alpha\beta} \right| Im'\eta \right\rangle = C \left\langle Im \left| \frac{3}{2}(I_\alpha I_\beta + I_\beta I_\alpha) - \delta_{\alpha\beta} I^2 \right| Im' \right\rangle \tag{4.10}$$

where C is a constant,

$$C = \frac{eQ}{I(2I-1)} \tag{4.11}$$

and Q is called the *quadrupole moment* and is a property of the nuclei:

$$eQ = \left\langle II\eta \left| e \sum_{k=\text{protons}} (3z_k^2 - r_k^2) \right| II\eta \right\rangle \tag{4.12}$$

For spin 1/2 nuclei the quadrupole moment would be zero, and there's no quadrupole coupling to the EFG.

The quadrupole Hamiltonian can now be written as

$$\mathcal{H}_Q = \frac{eQ}{6I(2I-1)} \sum_{\alpha,\beta} V_{\alpha\beta} \left[\frac{3}{2}(I_\alpha I_\beta + I_\beta I_\alpha) - \delta_{\alpha\beta} I^2 \right] \tag{4.13}$$

It is sometimes useful to rewrite Eq. 4.13 in terms of I^+ $(I_x + iI_y)$, $I^-(I_x - iI_y)$ and I_z for an arbitrary set of axes. Define:

$$\begin{aligned} V_0 &= V_{zz} \\ V_{\pm 1} &= V_{zx} \pm iV_{zy} \\ V_{\pm 2} &= \frac{1}{2}(V_{xx} - V_{yy}) \pm iV_{xy} \end{aligned} \tag{4.14}$$

we can then get a quadrupole Hamiltonian in the following form:

$$\begin{aligned}\mathcal{H}_Q =& \frac{eQ}{4I(2I-1)}\left[V_0(3I_z^2 - I^2) + V_{+1}(I^- I_z + I_z I^-)\right. \\ &\left. + V_{-1}(I^+ I_z + I_z I^+ + V_{+2}(I^-)^2 + V_{-2}(I^+)^2\right]\end{aligned} \tag{4.15}$$

Figure 4.1 illustrates the effect of quadrupole coupling to NMR spectrum and the final powder pattern. The energy was computed with the assumption that quadrupole coupling can be treated as a perturbation to the main Zeeman interaction. The first order perturbation gives an unaffected central line, but the so-called satellite transitions are usually several MHz away and "smeared out" in a powder sample due to the angular dependence of quadrupole coupling. The shift of energy follows equation

$$\Delta E_m^{(1)} = \frac{e^2 qQ}{4I(2I-1)}\left(\frac{3\cos^2\theta - 1}{2}\right)\left[3m^2 - I(I+1)\right] \tag{4.16}$$

where θ is the angle between the principle axis of the quadrupole moment and the direction of the external magnetic field. If we carry the perturbation calculation to the second order we can see that even the central transition gets shifted to the order of $(e^2qQ)^2/\gamma_n\hbar H_0$ and broadened for a powder sample.

In an isotropic liquid where fast random movement of molecules is present, the magnetic resonance frequency of quadrupole nuclei will not show any splitting because the average EFG is zero on NMR time scale (here NMR time scale is $1/\nu$ where ν is Larmor frequency). But at any transient moment the EFG is not zero and there's a coupling between EFG and magnetic moment of the quadrupole nuclei and it's fluctuating due to the molecule (or "lattice") movement, thus it will provide means for the nuclei to relax to lower energy state, hence the increased spin lattice relaxation. It was first shown by Sholl that in the fast motion limit, the quadrupole relaxation rate is

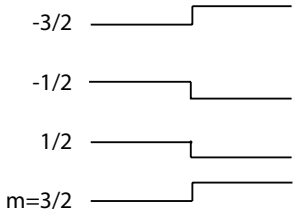

(a) Effect of quadrupole coupling to the first order. The shifts of all levels for $I = 3/2$ have the same magnitude.

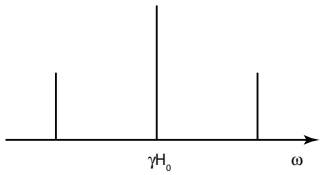

(b) Central line and sattelite lines. Central line is not affected to the first order.

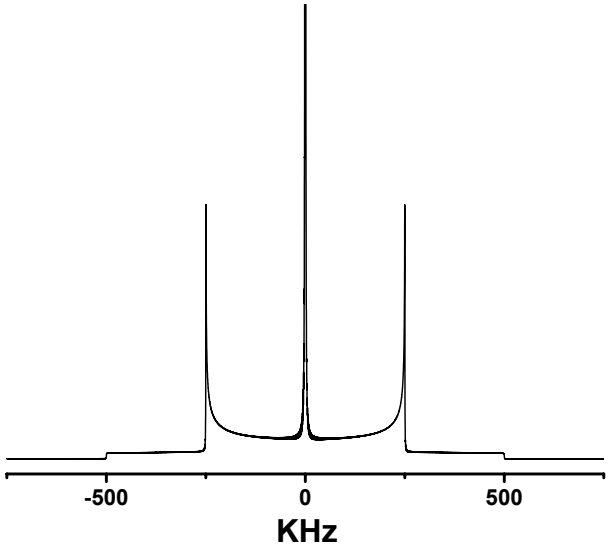

(c) Powder pattern. Spectrum is generated by SIMPSON NMR simulation program, for ^{63}Cu in 400 MHz magnet, with $e^2qQ/2h = 1$ MHz

Figure 4.1: Quadrupole coupling effect and powder patter in strong magnetic field.

determined by the integral of the correlation function of EFG as a function of t:

$$R_Q(T) = \frac{3}{4}\frac{2I+3}{I^2(2I-1)}\left[\frac{eQ}{\hbar}\right]^2 \left\langle |V_m|^2 \right\rangle \int_0^\infty dt \frac{\langle V_m^*(t)V_{-m}(0)\rangle}{\left\langle |V_m|^2 \right\rangle} \tag{4.17}$$

Here the angular brackets denotes an ensemble average, and V_m is a component of EFG as defined in Eq. 4.14 .

4.1.2 Experimental Results and Discussions

Figure 4.2 presents ^{65}Cu NMR spectra at various temperatures. We can see a clear systematic temperature dependence of Knight shift. We plot the temperature dependence of Knight shift in the insert of Figure 4.3 and immediately see that it's linear. Such a linear T-dependence of Knight shift is consistent with ^{31}P results in Chapter 3. Besides the shift, it is also seen from Figure 4.2 that there is a broadening of the spectra as the sample goes deeper into the supercooled region. Such a broadening was not seen in ^{31}P spectra (Figure 3.9 and insert in Figure 4.3). So the additional broadening of ^{65}Cu shouldn't be due to the fact that the chemical exchange is not fast enough, but because of the relaxation effect.

There are two significant contributions to the spin lattice relaxation of ^{65}Cu and ^{63}Cu in such a metallic liquid system: one is the nuclear quadrupolar relaxation explained in the previous section; the other one is the contribution due to Knight shift, as explained in section 3.2. The contribution from Knight shift is described in Eq. 3.10. We rewrite Eq. 3.10 here in another form:

$$R_K(T) = \frac{4\pi k_B \gamma_i^2}{\hbar \gamma_e^2} T K_s^2 / f \tag{4.18}$$

All quantities on the right side of Eq. 4.18 are constants or measurable, except f, the enhancement factor.

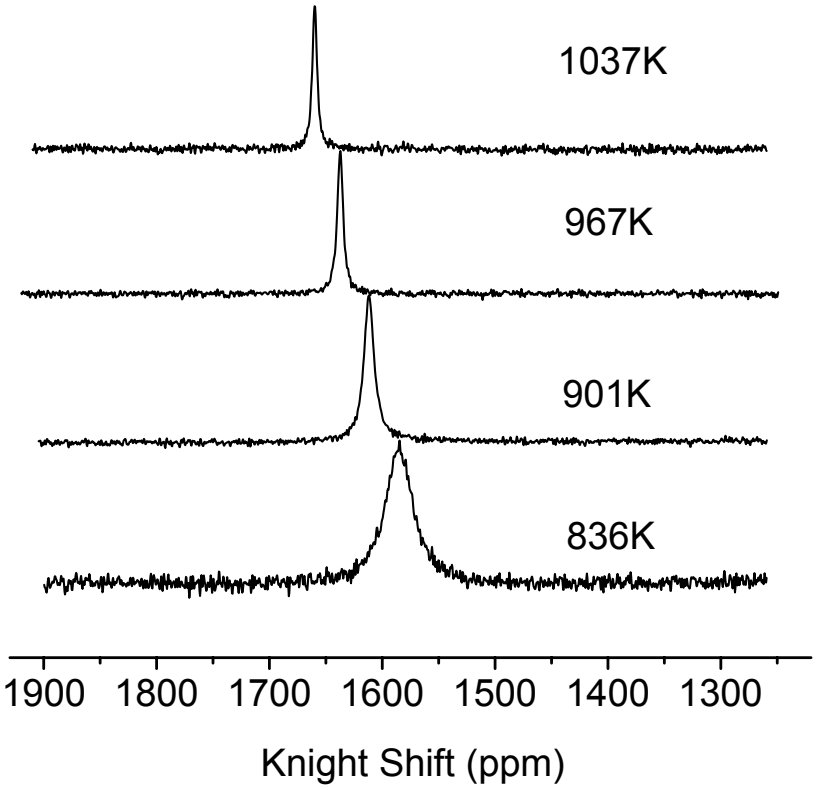

Figure 4.2: Spectra of ^{65}Cu in $Pd_{43}Ni_{10}Cu_{27}P_{20}$ at various temperatures.

In the fast motion limit, the rate of spin-lattice and spin-spin relaxation will be the same, and the NMR spectrum is a Lorentzian with full width at half maximum (FWHM) being (Abragam, 1961)

$$\Delta\nu_{1/2} = \pi^{-1}R \tag{4.19}$$

where R is the spin-lattice relaxation rate from all contributions. We verified the validity of Eq. 4.19 at 836 K and 967 K. Eq. 3 is obeyed at both temperatures. In other words, fast exchange condition is met for the temperature points we measured. Also from Figure 3.9 we see that in this temperature region, the FWHM of ^{31}P doesn't change much, which means that there's no line broadening due to chemical exchange being slower. So we take $\pi\Delta\nu_{1/2}$ as an easy way to obtain spin lattice relaxation rate R. To get R_Q, we need to further subtract R_K from R, or, according to Eq. 4.18, we need to determine the enhancement factor f. f is determined by a method commonly used in literature: the isotope effect, namely, the R_Q for ^{65}Cu and ^{63}Cu should be proportional to the square of their respective nuclear quadrupole moment, as manifested in Eq. 4.17. We neglect small isotope effect on the dynamics of ^{65}Cu and ^{63}Cu.

The final result of R_Q as a function of T is plotted in Figure 4.3, and we see a dramatic temperature dependence of R_Q. This dramatic change of R_Q as a function of temperature is explained in the following. For a nucleus of interest, the EFG at the nucleus is a sum of contributions from all other atoms in the liquid:

$$V_m(t) = \sum_{i=1}^{N-1} v_m(\vec{r}_{i0}(t)) \tag{4.20}$$

From Eq. 4.17 and Eq. 4.20 it is clear that quadrupolar relaxation is related to the dynamic processes in a liquid, but a detailed description to directly connect R_Q to experimentally measurable dynamical quantities proved to be difficult. It was recognized

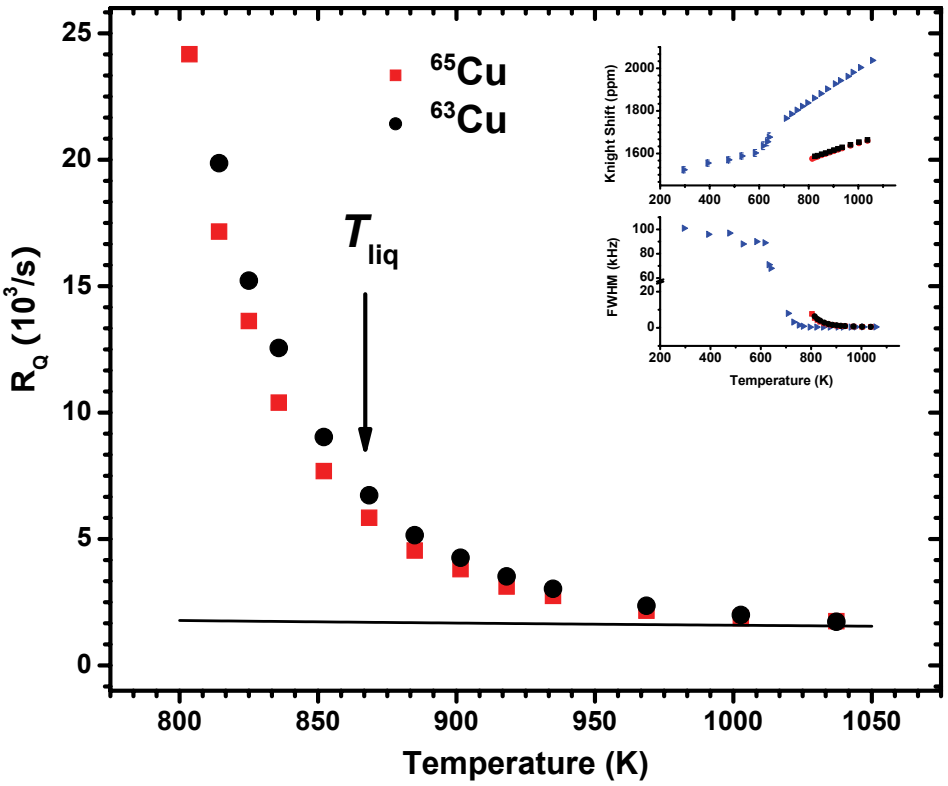

Figure 4.3: Temperature dependence of spin lattice relaxation rate for ^{65}Cu and ^{63}Cu in $Pd_{43}Ni_{10}Cu_{27}P_{20}$ system due to quadrupole effect. The solid line near the bottom is proportional to $T^{-1/2}$. The inserts are the temperature dependence of Knight shift and full width at half maximum of the spectra, respectively.

by Warren (William W. Warren, 1974) that the correlation of EFG should be determined by the timescale over which an ion moves on the order of inter-atomic separation but not on the macroscopic scale that is related to diffusion coefficient. The theory established by Warren and others predicts a roughly $T^{-1/2}$ law for NQR for pure liquid metals.

From Figure 4.3, we immediately see that the temperature dependence of NQR rate shows marked difference from $T^{-1/2}$ line predicted by the theory. Experimental data compiled in Ref. (Gaskell and Woolfson, 1984) shows that for many monoatomic metallic liquids, the T dependence of R_Q does follow a $T^{-1/2}$ variation. Enhancement of

R_Q and stronger temperature dependence are sometimes found for liquid alloys, which are not easily explained by a simple extension of the theory. Thermodynamic models were also proposed to explain NQR characteristics in liquid alloys (Ott et al., 1989). Although stronger temperature dependence are often observed for NQR in liquid alloys, we have yet to find a T-dependence that is as drastic as our case here. So we propose that in our case, the much stronger temperature dependence of NQR is related to dense packing and the deeply supercooled nature of the metallic liquid. In other words, we believe that the difference between our supercooled liquid and the monoatomic metallic liquid described by the aforementioned theory lies in dynamics, and we need to relate the correlation function of EFG to dynamic theory of liquids, especially that of dense random packed liquids.

In the theory for NQR in monoatomic liquids (William W. Warren, 1974; Sholl, 1974), there's an important assumption that the correlation of any other two atoms, i and j, is independent of the motion of the atom of interest. We contend that this may be true for monoatomic liquid at high temperatures, but not for densely random packed liquids at supercooled state. In regular liquid, where packing is not so efficient and the cage effect is not as obvious as in densely packed liquid, binary collisions provide the dominant structural relaxation mechanism, and the assumption about the independence of motion can be readily made. In a densely packed liquid, on the other hand, the cage effect is very strong. Atoms spend a long time rattling inside the cage before moving out of the cage, accomplishing yet another step of relaxation. The latter type of movement is highly cooperative and the assumption about the independence of motion would not longer be true, especially for atoms close by. Thus in a densely packed liquid, the movement of atoms can be a lot slower and a much stronger T dependence of atomic motions possible because of stronger T dependence of the latter type of motion. Reports on viscosity measurement in some metallic glass forming liquids (Masuhr et al.,

1999; Mukherjee et al., 2004) show that in such systems the atomic movement is indeed slow and glass forming ability is correlated to viscosity and specific volume. This further supports our arguments.

In mode coupling theory, the cage rattling type of motion provides the so-called β relaxation, while cage opening and atom moving out of cage give rise to α relaxation. For regular liquid, the time scale for β and α relaxation is not well separated, and the much slower $T^{-1/2}$ dependence of R_Q for regular liquids suggests a smooth T dependence from β relaxation in such liquids(Götze and Sjögren, 1992; Donth, 2001). In densely packed liquids, both the timescale and amplitude of cage rattling don't show a strong temperature dependence, and the contribution from β relaxation should be small due to its short time scale and the fact that at higher temperatures the R_Q is indeed much smaller, as seen in Figure 4.3. Thus we conclude that the main contribution of R_Q in our system comes from α relaxation.

Figure 4.4 replot our data in a way that will clearly show the power law T-dependence of the correlation time of EFG for both ^{65}Cu and ^{63}Cu nuclear sites and the data also points to a freezing temperature of about 700 K. We present the data in this way to further connect our experimental results to the predictions of MCT. MCT is not just a description of density correlation function $\Phi(\vec{q},t)$ but of any correlation function Φ_{XY} between quantities X and Y on condition that $\langle X\delta\rho_{\vec{q}}\rangle$ and $\langle Y\delta\rho_{\vec{q}}\rangle$ do not vanish. For time scale between microscopic time scale and the time scale for α relaxation, the correlation function Φ_{XY} can be written as:

$$\Phi_{XY}(t) = f_{XY} + h_{XY}\sqrt{|\epsilon|}g_{\pm}(\hat{t}), \qquad \hat{t} = t\,|\epsilon|^{1/2a}/t_0$$

where $\pm$ stands for the glass and liquid side of the transition, respectively, and t_0 is the microscopic time scale, $\epsilon \equiv (T_c - T)/T_c$. At longer time, The $\Phi_{XY}(t)$ can be approximated as Kohlrausch-Williams-Watt (KWW) stretched exponential (Kohlrausch,

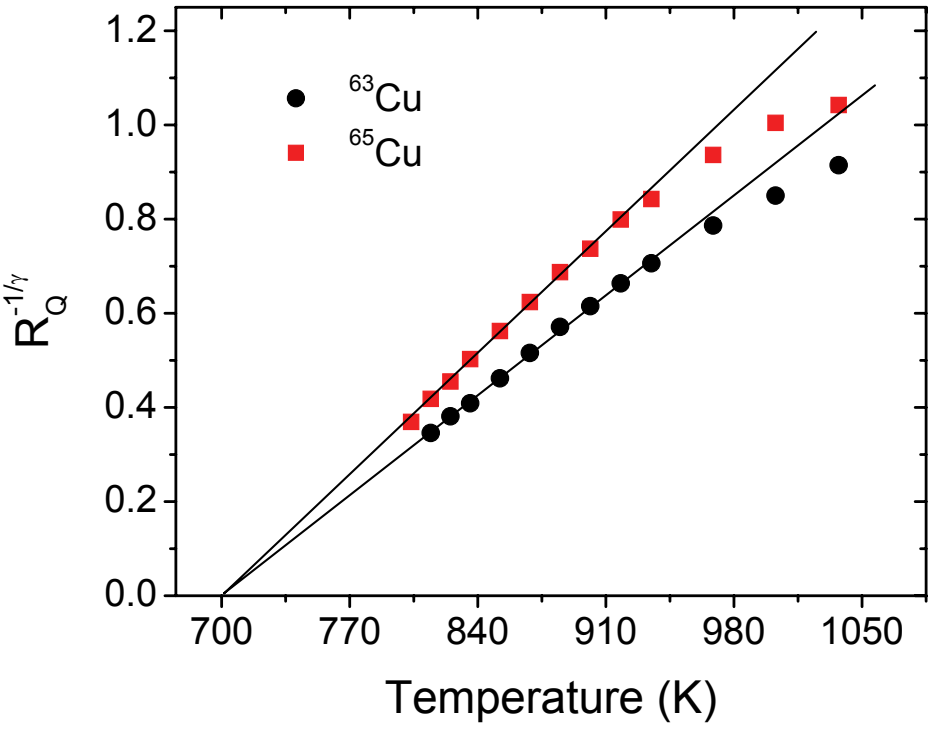

Figure 4.4: Power law temperature dependence of nuclear quadrupole relaxation rate of ^{65}Cu and ^{63}Cu in $Pd_{43}Ni_{10}Cu_{27}P_{20}$. Here $\gamma = 2.8$. The solid lines are guides to the eyes.

1854; Williams and Watts, 1970),

$$\Phi_{XY}(t) \cong A \exp\left[-(t/\tau_\alpha)^\beta\right] \tag{4.21}$$

with τ_α being the α relaxation time scale and its temperature dependence following Eq. 2.18.

In our case of quadrupole relaxation, the correlation function of interest would be that of EFG. From Eq. 4.17 we see that quadrupole relaxation rate is proportional to the integral of correlation function of EFG. When α relaxation is the dominant contribution to such an integral, or when cage rattling type of motion occurs at another higher frequency domain and only provides an average to the α relaxation contribution, from Eq. 4.21 we would expect that $R_Q(T)$ in Eq. 4.17 be proportional to τ_α, or propotionalproportional to $(T - T_c)^{-\gamma}$ according to Eq. 2.18. In other words, $[R_Q(T)]^{-1/\gamma}$ would then be proportional to $T - T_c$. Figure 4.4 shows that this is clearly the case for both ^{63}Cu and ^{65}Cu, and they both points to a singular T_c, 700 K. This agrees with the data for ^{31}P shown in Figure 3.8.

To our knowledge, our observation is an extension to previous research results on two fronts: one is to connect the theory of quadrupole relaxation in metallic liquid to the dynamic theory of liquids and get the conclusion that the nuclear quadrupolar relaxation rate is actually proportional to the α relaxation time scale on fast averaging limit; the other to extend the applicability of MCT to the case of the correlation function of EFG experienced by nuclei in the liquid. We explored an NMR technique that could be very useful in studying the dynamics of various complex fluids, and points to the dynamical processes that can be studied with this technique. We also get fulfilling experimental evidence that MCT is indeed a good theory to describe the dynamics above the temperature point where freezing starts. Although MCT is a theory of any correlation function of quantities that have non-trivial correlation with the density

fluctuation of the liquid, such correlation function often limits to density correlation function in real experiments. Our study shows that EFG correlation function is also one of the functions that can be studies within the theoretical framework of MCT.

4.2 1-d Lineshape Analysis

When temperature gets lower than the temperature points studied in the previous section, the Cu spectra get really broad due to slow quadrupole relaxation, so a much longer NMR averaging time is needed to reach desirable signal/noise ratio, but such long time averaging is not realistic because of sample crystallization. It is also important to note that at lower temperatures the ^{31}P also starts to broaden, so the assumption of fast averaging limit for Cu may not be true anymore. We have to use some other technique to study the dynamical processes at even lower temperatures. One of the techniques would be to study the change of line-shape of ^{31}P due to chemical exchange effect.

4.2.1 Theoretical Basis

The effects of chemical exchange on NMR spectra are familiar to us: as the rate of exchange increases, the spectrum lines broaden, coalesce and sharpen to a single averaged line. In our situation here, we assume that there is one to one correspondence between the chemical sites and the lines in the spectrum. This is equivalent to say that there is no spin-spin coupling, so it's sufficient to use classical representation to deal with the

problem. In classical theory, NMR is best described with Bloch equations:

$$\begin{aligned}
\frac{dM_x}{dt} &= \gamma M_y B_0 + \gamma M_z H_1 \sin 2\pi\nu t - \frac{M_x}{T_2} \\
\frac{dM_y}{dt} &= -\gamma M_z B_0 + \gamma M_z H_1 \cos 2\pi\nu t - \frac{M_y}{T_2} \\
\frac{dM_z}{dt} &= -\gamma M_x H_1 \sin 2\pi\nu t - \gamma M_y H_1 \cos 2\pi\nu t - \frac{M_z - M_0}{T_1}
\end{aligned} \tag{4.22}$$

In a rotating frame (u, v),

$$\begin{aligned}
M_x &= u \cos 2\pi\nu t - v \sin 2\pi\nu t \\
M_y &= -u \sin 2\pi\nu t - v \sin 2\pi\nu t
\end{aligned} \tag{4.23}$$

using Eq. 4.23, we can rewrite Bloch equations in the rotating frame,

$$\begin{aligned}
\frac{du}{dt} &= 2\pi v\,(\nu_0 - \nu) - \frac{u}{T_2} \\
\frac{dv}{dt} &= -2\pi u\,(\nu_0 - \nu) - \frac{\nu}{T_2} - \gamma B_1 M_z \\
\frac{dM_z}{dt} &= -\frac{M_z - M_0}{T_1} + \gamma B_1 \nu
\end{aligned} \tag{4.24}$$

Under steady state approximation, $du/dt = dv/dt = dM_z/dt = 0$, we have the solution to Eq. 4.24:

$$\begin{aligned}
u &= \frac{2\pi\gamma B_1 M_0 T_2^2 (\nu_0 - \nu)}{1 + 4\pi^2 T_2^2 (\nu_0 - \nu)^2 + \gamma^2 B_1^2 T_1 T_2} \\
v &= \frac{\gamma B_1 M_0 T_2}{1 + 4\pi^2 T_2^2 (\nu_0 - \nu)^2 + \gamma^2 B_1^2 T_1 T_2} \\
M_z &= \frac{M_0 \left[1 + 4\pi^2 T_2^2 (\nu_0 - \nu)^2\right]}{1 + 4\pi^2 T_2^2 (\nu_0 - \nu)^2 + \gamma^2 B_1^2 T_1 T_2}
\end{aligned} \tag{4.25}$$

Under normal experimental conditions, $\gamma^2 B_1^2 T_1 T_2 \ll 1$ (non-saturation condition),

the magnetic moment in the x-y plane can be treated as a complex number G,

$$\begin{aligned} G &= u + iv \\ \frac{dG}{dt} &= -G\left[\frac{1}{T_2} - 2\pi i(\nu_0 - \nu)\right] - iC \end{aligned} \tag{4.26}$$

with $C = \gamma B_1 M_0$.

Now we consider two chemical sites in equilibrium and the exchange between them, and rewrite Eq. 4.26 in the following way:

$$\begin{aligned} \frac{dG_A}{dt} &= -\alpha_A G_A - iC_A - k_A G_A + k_B G_B \\ \frac{dG_B}{dt} &= -\alpha_B G_B - iC_B - k_B G_B + K_A G_A \end{aligned} \tag{4.27}$$

where $\alpha = 1/T_2 - 2\pi i(\nu_0 - \nu)$, k_A, k_B are the jumping rates from site A to site B and from site B to site A, respectively. Eq. 4.27 are called the *modified Bloch equations*. The solution to such equations would be

$$G = -\frac{iC_0(k_A + k_B + \alpha_A p_B + \alpha_B P_A)}{\alpha_A k_B + \alpha_B k_A + \alpha_A \alpha_B} \tag{4.28}$$

where $G = G_A + G_B$, $p_A + p_B = 1$, $p_A k_A = p_B k_B$ with p_A, p_B as fractional populations in site A and site B. To separate G into real and imaginary part is not a trivial task, and we shall not try to write down the separated form here except to illustrate the consequence of chemical exchange in Figure 4.5. We can see from the figure two extreme conditions: *slow exchange* and *fast exchange*. At the slow exchange extreme, we see two separated Lorenzian lines; At the fast exchange limit, the two lines coalesce into a single Lorenzian line. In-between the two extremes, the line shape evolves as a function of the jumping rate. When there's multi-site exchange, the right side of Eq. 4.28 remains similar but contains more complicated matrix forms.

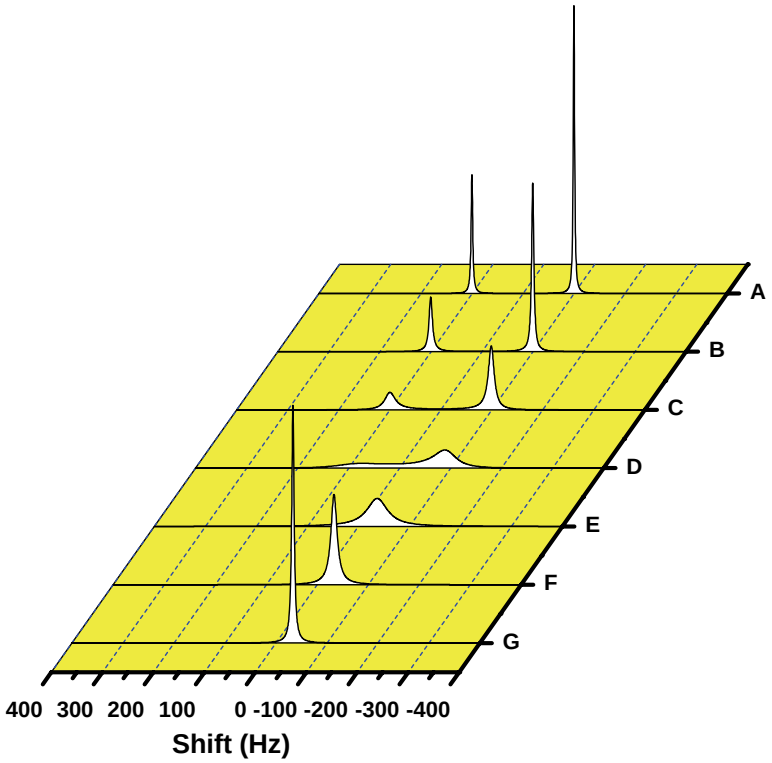

Figure 4.5: Two site chemical exchange as an example. $\delta\nu = 200$ Hz, $T_2 = 2$ s for both peaks, natural line width is 2 Hz, $p_1 = 0.333$, $p_2 = 0.667$. The rate constants for A, B, C, D, E, F are: 0, 20, 100, 600, 2500, 10000, 50000 Hz, respectively. Spectra are calculated with MEXICO program. (Bain and Duns, 1996)

4.2.2 Simulation

The simulation of the chemical exchange effect was done using the program MEXICO (Bain and Duns, 1996), where in uncoupled case one can specify more than 100 peaks with different shift and intensity, the natural line-width and T_1 for each peak, and jump rate matrix between these peaks.

For our amorphous sample, the spectrum (Figure 3.6) shows only a broad peak. To be able to get distinct chemical environments for simulation, we sliced the spectrum evenly in frequency axis as shown in Figure 4.6. Each column will then represent a distinct chemical environment, with the center of the column as the resonance frequency for that environment, and the area under that column over the total area as the possibility of finding a ^{31}P in such an environment. We assume a single hopping rate k, so the hopping probability to any column A would be

$$P_A = \frac{S_A}{S} \tag{4.29}$$

where S_A is the area under column A, S is the total area of the spectrum.

We now have the sites, the shift and intensity of each site, and hopping matrix according to Eq. 4.29. We assume that T_1 is the same for every site—the real T_1 measured in experiment at that temperature. We put all these information into the input file for MEXICO and simulate the spectrum using different hopping rate k at each temperature, and find out the best fit for the real spectrum at that temperature. In this way we can determine the hopping rate k as a function of temperature. Figure 4.7 shows simulation result at one temperature, 730 K, and the final results for all temperatures are included in Figure 4.9.

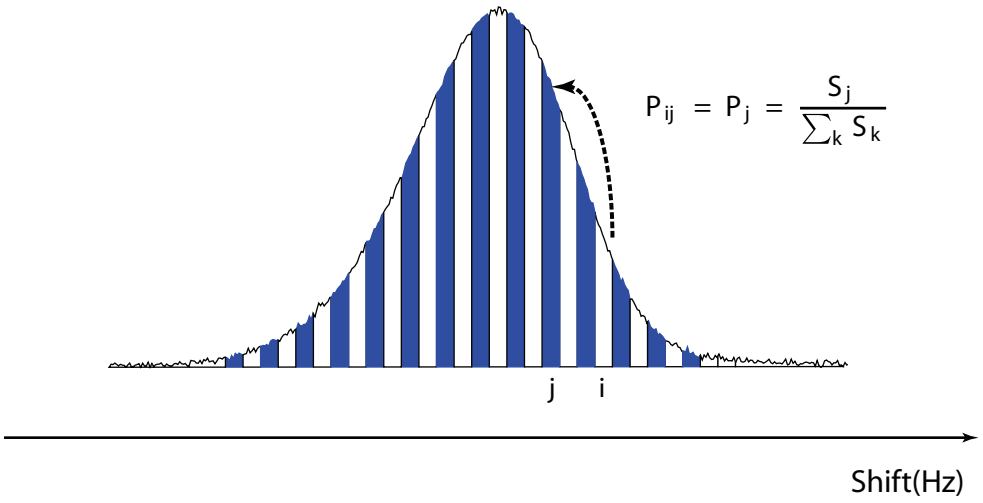

Figure 4.6: Illustration of method used for 1-d line shape simulation of broad amporphous spectrum. The shape of the evelope is from experimental NMR spectrum of ^{31}P spectrum in $Pd_{43}Ni_{10}Cu_{27}P_{20}$. Each column in the envelope represents a distinct chemical environment, and the hopping between these chemical enviroments is assumed to be completely random. Real simulation was done using 300 sites to accurately reproduce the shape of the spectrum.

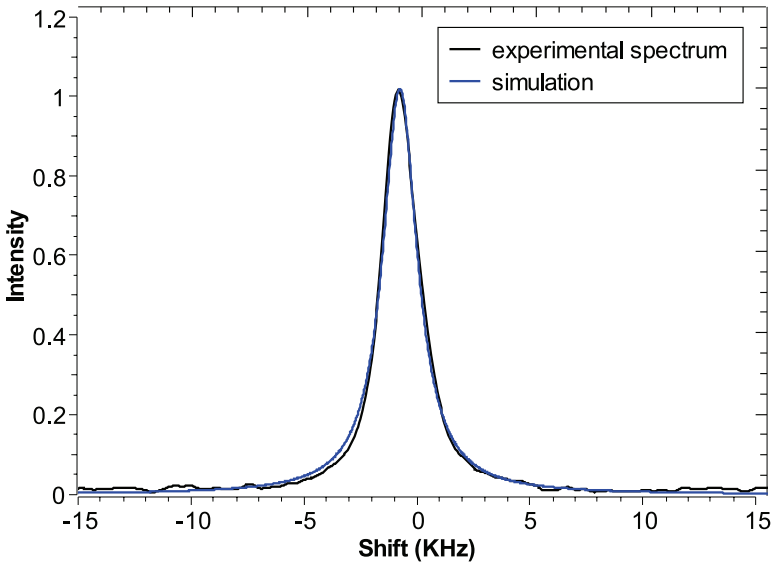

Figure 4.7: 1-d line shape simulation of ^{31}P line shape at temperature point 730 K. A hopping rate of 9.2×10^6 Hz was obtained from simulation.

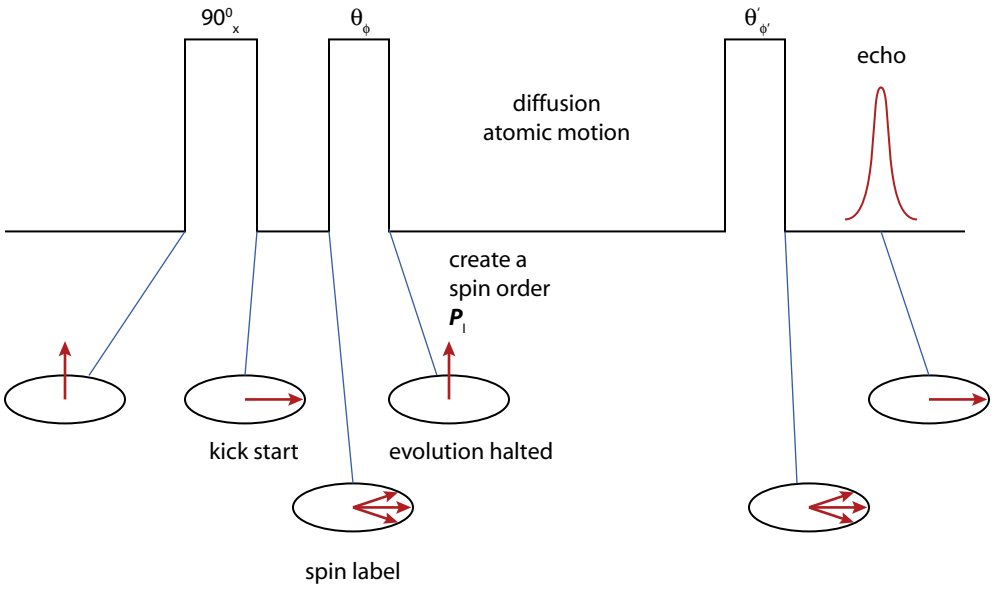

Figure 4.8: Stimulated echo pulse sequence.

4.3 Stimulated Echo

For extremely slow hopping at low temperatures, the simulation of 1-d line shapes won't be accurate anymore, and new techniques must be employed to study slow hopping phenomenon. Stimulated echo is one of the techniques that could be useful here. The experimental work in this part was done by Dr. Xiaoping Tang, so in this dissertation I'll just briefly discuss the basic principles of the stimulated echo technique and include Xiaoping's data in our final graph.

The stimulated-echo sequence of an NMR experiment consists of three pulses: after a first $\pi/2$ pulse at $t = 0$ the second one follows after a preparation time t_p; then after a certain mixing time t_m the third pulse is applied and the echo at $t = t_p + t_m + t_p$ is recorded. With the second pulse the transverse magnetization is transformed into a population state, i.e. longitudinal magnetization or spin-alignment, depending on the phases of the pulses. If molecular motion in the t_p time is slow compared to phase

changes of transverse magnetization ($\Phi^{\lambda}(t) = \omega^{\lambda}(0)t_p$), the phase changes would then be stored after the second pulse, and the prepared population state would evolve under the influence of the molecular motion and the spin-lattice relaxation. The third pulse after the mixing time transforms the remaining population into the transverse magnetization. Thus aside from the spin-lattice relaxation influence, the echo-amplitude at a time t_p after the third pulse is determined by the "*phase correlation function*":

$$E_2(t_p, t_m) = \left\langle \exp\left[i\omega^{\lambda}(t_m)t_p\right] \exp\left[-i\omega^{\lambda}(0)t_p\right] \right\rangle \tag{4.30}$$

Out of Eq. 4.30, the two functions

$$E_2^{ss}(t_p, t) = \left\langle \sin\left[\omega^{\lambda}(t)t_p\right] \sin\left[\omega^{\lambda}(0)t_p\right] \right\rangle \tag{4.31}$$

and

$$E_2^{cc}(t_p, t) = \left\langle \cos\left[\omega^{\lambda}(t)t_p\right] \cos\left[\omega^{\lambda}(0)t_p\right] \right\rangle \tag{4.32}$$

can be measured independently by proper phase-cycling. $\omega^{\lambda}(t)$ and $\omega^{\lambda}(0)$ are proportional to the local magnetic field experienced by a given spin λ after and before the mixing time t_m. If the local environment of any given spin does not change during the time interval t, $\omega^{\lambda}(t)$ and $\omega^{\lambda}(0)$ will be the same and the echo-amplitude will only decay through the spin-lattice relaxation given by the factor $\exp(-t/T_1)$. If atomic hopping over mixing time is significant, ω^{λ} is likely to change during time interval t. Assuming a stochastic hopping process during mixing time t_m, with a hopping rate constant Ω, $E_2^{ss}(t_p, t)$ decays as $\exp(-\Omega t)$. In we include spin-lattice relaxation, the echo amplitude $f(t)$ will be proportional to $\exp\left[-(\Omega + 1/T_1)t\right]$:

$$f(t) \propto \exp\left[-(\Omega + 1/T_1)t\right] \tag{4.33}$$

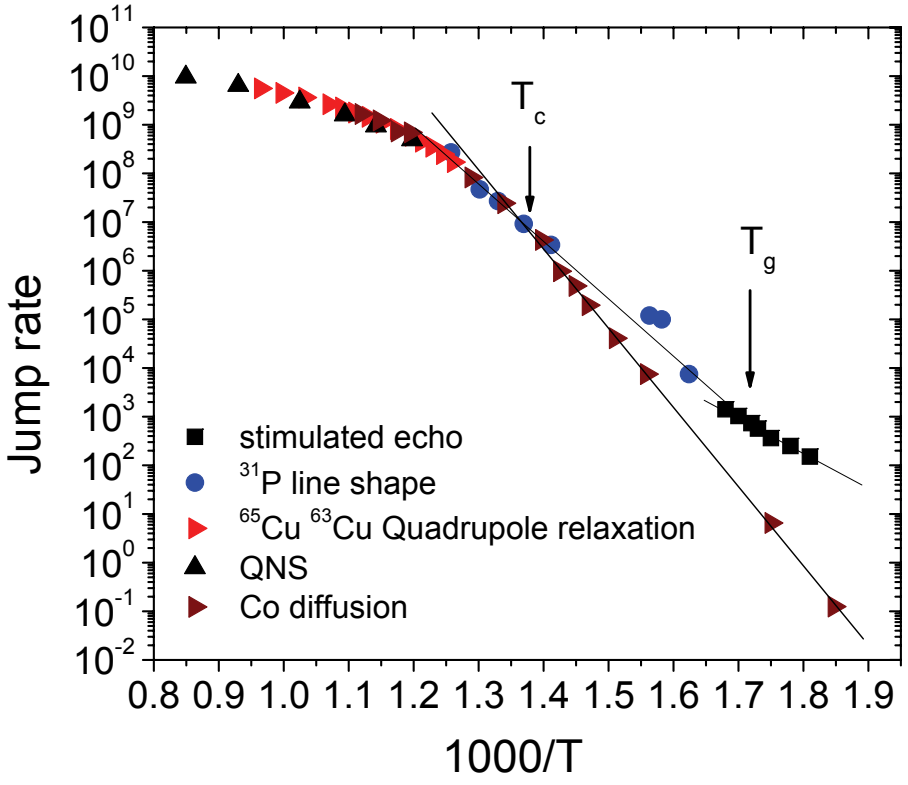

Figure 4.9: Study of dynamical processes in $Pd_{43}Ni_{10}Cu_{27}P_{20}$ on different nuclei with various techniques. Stimulated echo data is from Ref. (Tang et al., 2005), Co tracer diffusion data is from Ref. (Zöllmer et al., 2003), and quasi-elastic neutron scattering data is from Ref. (Meyer, 2002). Jumping rates from ^{31}P stimulated echo adn ^{31}P line shape analysis are absolute numbers. Data from quadrupole relaxation, Co diffusion, and QNS are normalized by certain factors.

thus by measuring spin-lattice relaxation and the echo decay as a function of mixing time t, one can get a hopping constant for atomic motion.

4.4 Results and Discussions

In Figure 4.9 experimental data from various techniques as well as from other publications are compiled together for good comparison. It is seen that at temperatures above T_c, the dynamical processes for different nuclei studied by different techniques

show the same temperature dependence. From T_c to lower temperatures, the data for ^{31}P and Co diffusion starts to differ. The difference gets greater at low temperatures. A decoupling of diffusion modes so far has been observed in ionic compounds where distinct cationic or anionic species were reported to have different mobilities. There is also study of decoupled relaxation in metallic glassformers but it was mainly in the glassy state. In the present result, the whole temperature region was probed for differences in diffusion behavior for different types of atoms. The pictures that can emerge from the current study is that for temperatures above T_c, diffusion is dominated by flow-type of motion, and cooperative flow of interacting atoms guarantees that even for different sizes of atoms with different local bonding, since they are moving together in a cooperative way, their diffusion behavior is the same. Below T_c, the main contribution for relaxation should be activated process, and for different types of atoms, a difference in activation energy provides different slopes for ^{31}P and Co below T_c in Figure 4.9.

Therefore, the study of slow processes is still best explained in the framework of extended MCT. Above T_c, the dominant slow process is cooperative flow, and the relaxation time for such process exactly follows the MCT power law equation (Figure 4.4). According to ideal MCT, the supercooled liquid would freeze at T_c. But when activated process is included in the extended MCT, ergodicity can be restored by such processes. So below T_c, the dominant slow process becomes "activated hopping", and we see a difference in activation energy for ^{31}P and Co.

The current result also points to a temperature T_c, the same as the dynamic crossover temperature in the previous chapter. This temperature is also close to the temperature where a crossover in crystallization mechanism was observed(Schroers et al., 2002). It is also reported that this is also the point where the Debye-Einstein relationship fails (Zöllmer et al., 2003). Naturally these are connected observations that all points to a crossover temperature T_c, where definitely there is a transition is the

dynamics of the system. Whether there is corresponding change in thermodynamics still remains to be verified. In the following section we'll crudely examine some of the thermodynamic theory of glass transition and make our suggestions.

One feature in Figure 4.9 remains yet to be explained, namely, the change of slope at T_g for ^{31}P data. Is there something important happening at T_g? And what is it if there is? One can probably dismiss this question by saying that this is just the consequence of the relaxation timescale of the supercooled liquid crossing the timescale of the experiment. Below T_g, the sample doesn't have enough time to relax, so it may have more free volume and hence the increased hopping. If one anneals the sample below T_g for long enough time, the hopping rate will be smaller and there will be no obvious change of slopes at T_g. This is a possible explanation, but not the only answer at the present time. There are indications that something more fundamental is going on around T_g, and it's in the author's belief that later studies will reveal the fundamental physics around T_g.

4.5 Discussion within the Context of Thermodynamic Theories

4.5.1 Energy Landscape

The energy landscape picture was articulated more than 30 years ago (Goldstein, 1969), and offers a convenient topographical view (Figure 4.10) for interpreting the complex phenomenology regarding the glass transition (Stillinger, 1995). It considers the potential energy function of an N-body system $\Phi(\vec{r}_1, \ldots, \vec{r}_N)$, where vectors $\vec{r}_i$ comprise the position, orientation and vibration coordinates. For the simplest case, the particles do not have internal orientational or vibrational degrees of freedom, the landscape is a

$(3N+1)$-dimensional object. The quantities of interest here are the number of potential energy minima (often called inherent structures) of a given depth, and the nature of saddle points separating the neighbouring minima.

An important observation in our experiment is that there is a T_c above T_g that marks a crossover of dynamical processes. Any theoretical considerations shall have to be able to take this into account. In fact, in Goldstein's seminal paper which raised the idea of potential energy barrier (Goldstein, 1969), he stated that in very "viscous" liquid with shear relaxation time $\geqslant 10^{-9}$ sec, flow is dominated by potential energy barriers high compared to thermal energy, whereas at higher temperatures this will no longer be true. On the other hand, it was noted by Angell (Angell, 1988) that experimentally it is often found that the shear relaxation time is on the order of 10^{-9} seconds for the MCT T_c. So it's very possible that there's a connection between these two descriptions. So far, however, real energy landscape is mainly explored in computer simulations, and some of them did establish such connections between energy landscape and MCT to provide a description of crossover behavior in term of system potential energy. A lot of these simulations have appeared in literature (Angelani et al., 2000; Broderix et al., 2000; Denny et al., 2003). Here we'll use one as a particular example (Sastry et al., 1998).

For an N-body material system in volume V, the landscape is fixed. The way the system samples its landscape as a function of temperature provides information on its dynamical behaviour, while how a landscape deforms as a result of changes in density provides information on the mechanical properties of the material. Figure 4.11 shows the average IS energy for a mixture of unequal-sized atoms as a function of temperature. At higher temperatures (labeled as free diffusion in Figure 4.11) the IS energy is is virtually temperature independent, suggesting that the system has enough thermal energy to sample the entire energy landscape, and the overwhelming number of the en-

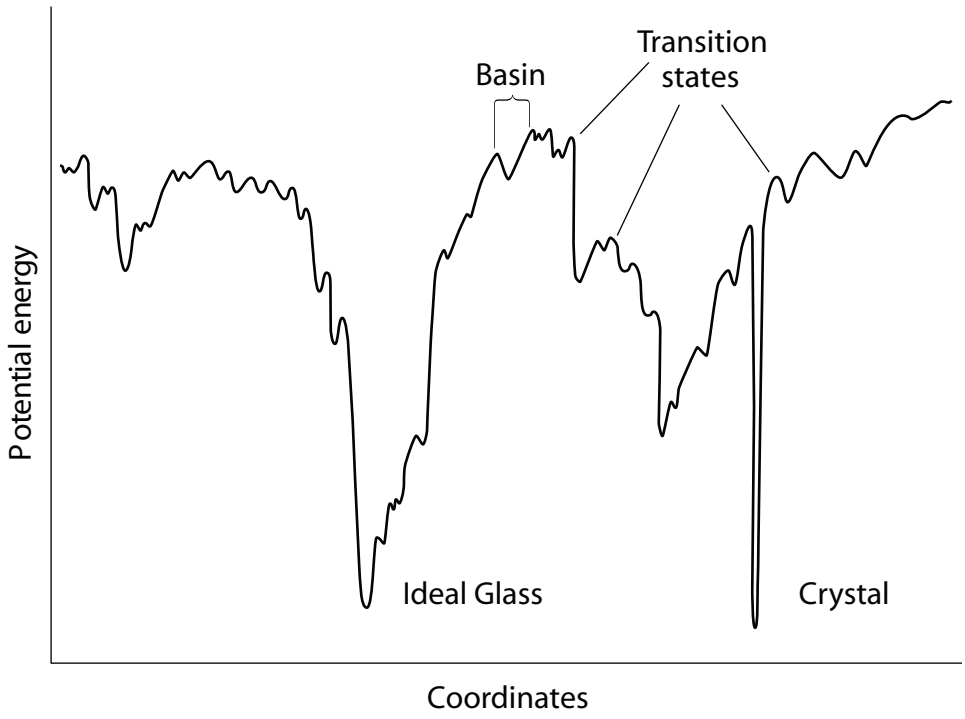

Figure 4.10: Schematic view of an energy landscape. The x-axis represents all configurational coordinates. Adapted from (Stillinger, 1995; Debenedetti and Stillinger, 2001).

ergy minima are shallow and the deep minima are rare. But as the reduced temperature decreases to a point of $T = 1$, the system becomes unable to cross the highest energy barriers and is forced to sample the much rarer deeper minima. When this happens, the kinetics of structural relaxation changes from exponential to stretched exponential, and the activation energy increases with decreasing temperature (landscape influenced in Figure 4.11). Below a temperature of $T \approx 0.45$, the height of the barriers separating sampled IS increases abruptly (landscape dominated in Figure 4.11). Finally at low enough temperature the system becomes stuck in a single minimum, the depth of which increases as cooling rate decreases (Glass in Figure 4.11).

Three important temperature was pointed out in these type of simulations: T_0, T_x

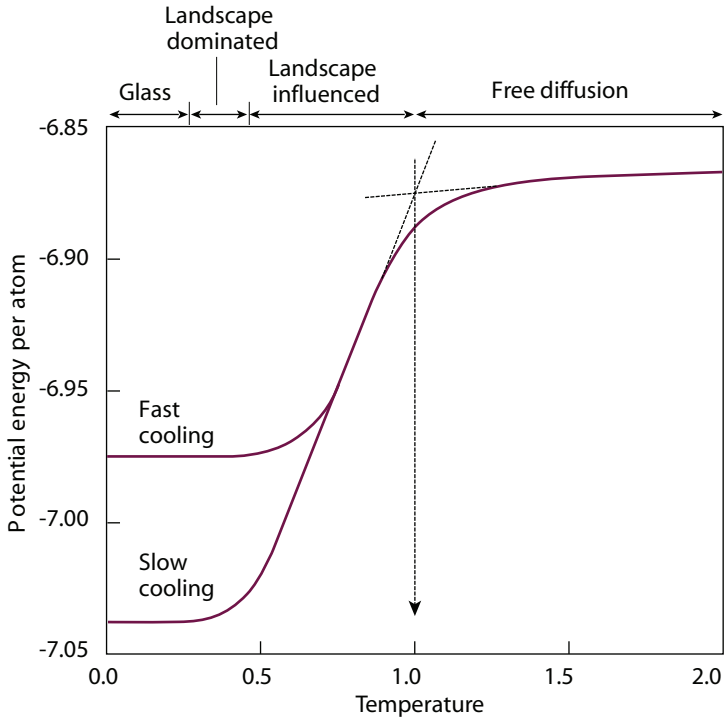

Figure 4.11: Mean IS energy per particle of a binary mixture of unequally sized Lennard-Jones atoms as a funtion of reduced temperature. When $T > 1$, the energy of the system is sufficiently high to sample all the energy minima (free diffusion); between $T = 1$ and $T \approx 0.45$, the mechanically stable configuration the system can sample are strongly temperature dependent and the activation energy of the system increases upon cooling (landscape influenced); below $T \approx 0.45$, the height of the barriers seperating sampled adjacent energy minima seems to increase abruptly, and the particles execute rare jumps over distances roughly equal to interparticle distance (landscape dominated). Adapted from (Sastry et al., 1998; Debenedetti and Stillinger, 2001).

and T_g, where T_0 stands for the transition from free diffusion to "landscape influenced" region, T_x from "landscape influenced" to "landscape dominated", and T_g the glass transition. From our experimental results, we don't see the existence of a T_0, but it's possible that this is due to our temperature not being able to go high enough (about 1500 K if $T_c \approx T_x = 0.45T_0$). We do see a crossover in dynamics at $T_c \approx 700$ K, and almost all the simulations show that T_x is in proximity to MCT T_c. If this picture is true, T_c then is the point below which the liquid is trapped most of the time in the local minima of the energy landscape, while at higher temperature the liquid can explore high order saddle points (Angelani et al., 2000). In terms of diffusion, at higher temperature (above T_c), the system can cross over saddle points and change configurations easily. This type of configuration change involves nearby atoms (high order saddles) so it is reasonably expected that all type of atoms would diffuse in the same way in the "flow" process. At lower temperatures (below T_c), the diffusion would be more like solid which is dominated by activated hopping process, so smaller and lighter elements have a higher probability for hopping. Although in this region the system is "landscape dominated", it still has chances to cross the saddle points, or to have flow process; but below T_g, such chances would diminish to zero, and activated hopping becomes the single dominant process. In terms of the vibrational processes, it seems that when the system is trapped in a local minima, it has lower degrees of freedom for such processes, hence the abrupt changes between T_c and T_g, and a higher slope for $T > T_c$ compared to that for $T < T_c$ (Figure 3.8).

While this type of explanation based on energy landscape offers an appealing picture, one has to bear in mind that the energy landscape theory is still qualitative. No quantitative predictions can be given, at least as to our observations here. So our results can not act as a verification of the theory, although it shouldn't be deemed as adventurous either to state that there's no serious contradictions between the energy

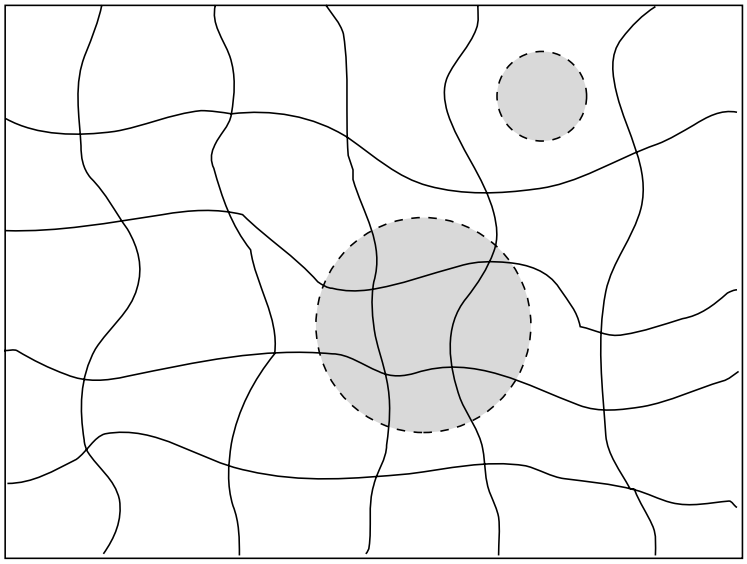

Figure 4.12: "Mosaic structure" in random first order transition theory. The mosaic structure represents local metastable configuration in supercooled liquids. The system escapes from a local metastable configuration by an activated process equivalent to forming a liquidlike droplet inside a mosaic element. Adapted from (Xia and Wolynes, 2001b).

landscape picture and our experimental results.

4.5.2 Random First Order Transition

The notion of random first order transition (RFOT) is based on the early efforts to connect the dynamical MCT of structural glass to the mean field theory of spin glasses (Kirkpatrick and Wolynes, 1987a; Kirkpatrick and Thirumalai, 1987; Kirkpatrick and Wolynes, 1987b). The RFOT theory considers the activated dynamics which is termed as "hopping process" in MCT, and give a physical picture and thermodynamical description of such activated processes. According to RFOT theory of glasses (Xia and Wolynes, 2001b; Lubchenko and Wolynes, 2003), the barriers for activated dynamics in supercooled liquids vanish as the temperature of a viscous liquid approaches the dy-

namical transition temperature from below. The dynamical transition thus represents a crossover from low T activated behavior to a "collisional transport regime" at high T. The theory is also able to explain the fragility of the supercooled liquid and Vogel-Fulcher law (Xia and Wolynes, 2000), the deviation from Stokes-Einstein relationship (Xia and Wolynes, 2001a), stretched exponential relaxation (Xia and Wolynes, 2001b), the aging phenomenon (Lubchenko and Wolynes, 2004). Recently Efforts have also been made to bridge the RFOT theory and MCT (Bhattacharyya et al., 2005).

Important temperature points in RFOT theory are T_A and T_k. T_A is the dynamical transition at high temperature (above T_g), and T_k is a static transition below T_g. T_A has further been identified same as T_c in mode coupling theory, and T_k identified as Kauzmann temperature. in RFOT theory, T_g is nothing but a temperature at which the relaxation timescale of the liquid reaches the laboratory time scale of about 1 hour. It's encouraging that such a naive picture illustrated in 4.12 can produce rich theoretical predictions in RFOT theory, but it seems to me to be a little awkward to imagine that below T_g, there are still "liquid droplets" in the solid matrix. Nevertheless, RFOT theory points to a promising direction: use new thermodynamic models at a microscopic level to describe the dynamics below T_c. At present stage, we believe that such a thermodynamic model must take into full account the change of dynamics around T_g. We may imagine that with a microscopic model which introduces solid-like cluster in the supercooled liquid at T_c and transforms the supercooled liquid into a complete solid at T_g would be able to bridge the gap between MCT and low temperature phenomena observed in supercooled liquids and glasses.

CHAPTER 5

STRUCTURE

Metallic glasses, being amorphous in nature, may possess intriguing local structural ordering. Such local structure can not only influence the glass forming ability, it may also have an impact on the phenomena of glass transition itself. So the study of structure in metallic glasses under various conditions may help us find ways to improve the glass forming ability and look for new compositions that can form metallic glasses. For basic science, such studies will also help us better understand metallic glasses, glass in general, crystallization processes, and glass transition itself.

5.1 Primary Crystallization in $Al_{92}Sm_8$

Metallic glasses have many desirable properties such as great strength, high elastic limit, corrosion resistance and wear resistance, etc, so naturally people would like to combine these properties with the lightness of some metallic elements to produce a metallic glass that is light and strong. A perfect candidate would then be an aluminum-based metallic glass, with the atomic percentage of aluminum as high as possible. Yet so far Al-based metallic glasses proved to be difficult to make. Since the first published research results that demonstrated some Al-based metallic glasses in ribbon shape (He et al., 1988; Inoue et al., 1988), the glass forming ability of Al-based glasses haven't been improved

much (Greer, 1995). So the important question is what type of crystalline phase these Al-based metallic glasses would most easily form out of amorphous matrix.

The metallic glass we studied here is of the composition $Al_{92}Sm_8$. This type of alloy can not produce bulk glasses but rather require rapid quenching to form glasses in ribbon shape. While many bulk glass forming alloys have substantial levels of a number of components, the marginal glasses are derived from alloys that are rather lean in solute content with solvent concentration in 85-90 at.% range. There is still ongoing investigation of the structural and alloy chemical origins of glass formation. Under the usual diagnostic examination for glass formation based upon transmission electron microscopy (TEM), x-ray diffraction analysis (XRD) and DSC, this type of glasses appears to be true amorphous materials. There's an unusual phenomenon related to this material, however, and we may call it primary crystallization (Perepezko et al., 2003a; Perepezko et al., 2003b). It is seen clearly in Figure 5.1 that there's no clear glass transition temperature in the DSC curve, while for samples obtained from cold-rolling does show a glass transition temperature of 172 °C (Wilde et al., 1999). There's a clear exothermic peak for each of the melt-spinning samples (batch A, B, C) presented here with an onset temperature of about 170 °C. We call this peak primary crystallization peak. From Figure 5.3 it's obvious that even by annealing the sample at 130 °C which is far below T_g, part of the sample will crystallize into aluminum crystalline phase. To find out exactly what's the reason for such early crystallization, one has to characterize the CSRO inside the sample. As one can see from XRD pattern 5.3 and TEM images 5.2, such usual structural characterization techniques won't be able to tell exactly what's going on. On the other hand, NMR is very sensitive on the local chemical environment of specific type of nuclei. More importantly, for quadrupole nuclei, NMR is extremely sensitive on the local symmetry around the nucleus of interest. In this sample ^{27}Al is a good candidate for NMR study. ^{27}Al is a spin 5/2 nuclei, we would also expect that

local symmetry around ^{27}Al is able to give us detailed structural information.

5.1.1 Sample processing

Homogeneous ingots of $Al_{92}Sm_8$ were produced by repeatedly arc-melting high-purity (99.999%) constituents of each alloying element in a Ti-gettered, argon atmosphere. Amorphous melt-spun ribbon samples were synthesized by ejecting the molten alloy from a quartz crucible onto a rapidly spinning Cu wheel (55 m/s tangential velocity) in an Ar atmosphere. The structure of the melt-spun ribbon samples was confirmed to be macroscopically amorphous by XRD with Cu-Kα radiation. As solidified ribbon samples were annealed for various times at 130 ^{o}C to induce primary Al nanocrystals in the residual amorphous matrix. Subsequently, NMR measurements were performed.

5.1.2 NMR Measurement

The NMR experiments were carried out on a 9.4 T and a 4.9 T magnet. the ^{27}Al central transition was observed at 104.356 MHz in the 9.4 T magnet and 52.22 MHz in the 4.7 T magnet with a Hahn echo pulse sequence.

As we have known already, the main NMR shift mechanism in a metallic system is the Knight shift due to the interactions between nuclei and electrons. In this system, ^{27}Al is a spin 5/2 quadrupole nucleus with an NMR spectrum that is also very sensitive to quadrupole interactions between the nuclear spin and the EFG present at the ^{27}Al nucleus. If the structure around the ^{27}Al nucleus is cubic, as is the case for crystalline Al, the EFG is reduced to zero and the quadrupole coupling vanishes between ^{27}Al and the EFG. If, on the other hand, the local structure is not cubic, as one would expect for an amorphous environment, the transition between the ^{27}Al spin states will split into three levels. For a powder pattern, the satellite transitions normally extend over MHz and "thin-out" in an NMR spectrum (Figure 4.1). The central transition

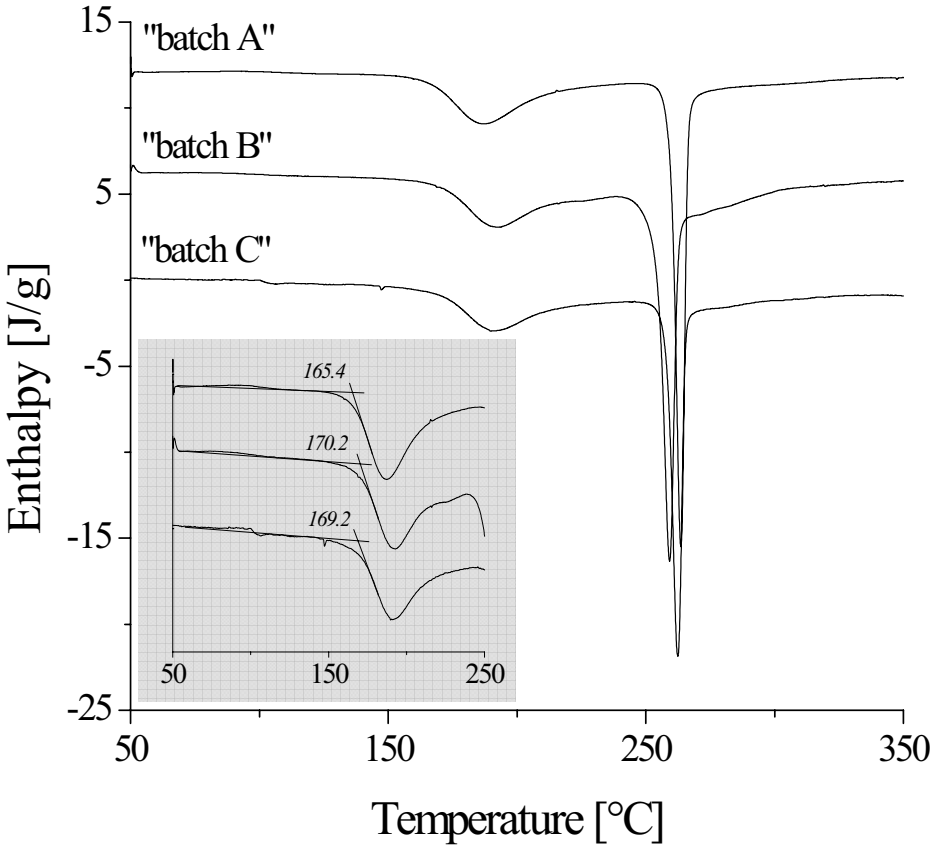

Figure 5.1: DSC trace of different batches of $Al_{92}Sm_8$ glass sample produced in conditions controlled as identical as possible. Figure is from Prof. Perepezko's group (see ACKNOWLEDGEMENT).

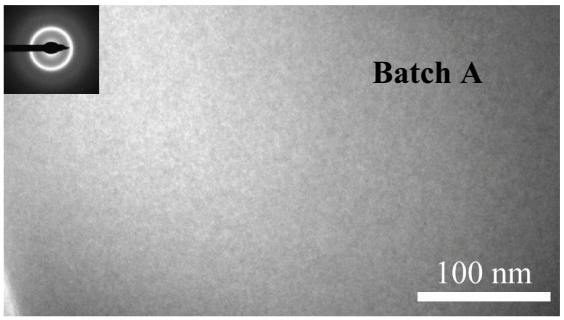

(a)

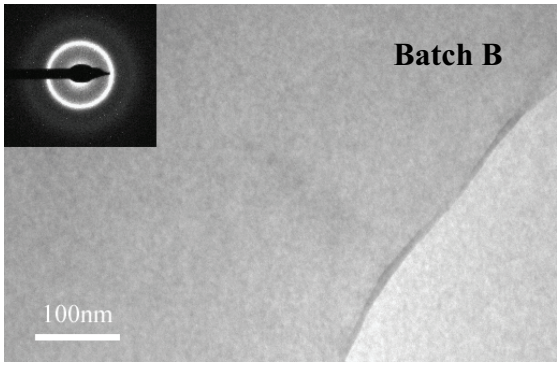

(b)

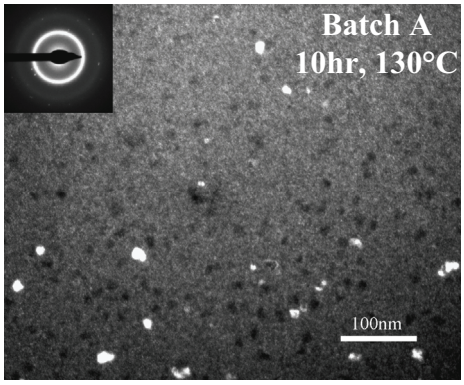

(c)

Figure 5.2: TEM images of samples of $Al_{92}Sm_8$. Batch A and batch B as-quenched sample appears to be amorphous, while sample of batch A annealed at 130 °C for 10 hours contains nano-crystals inside the amorphous matrix. Figure is from Prof. Perepezko's group (see ACKNOWLEDGEMENT).

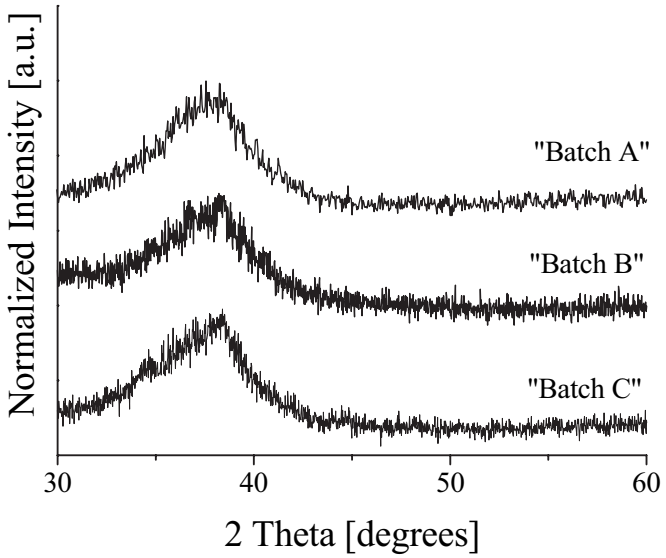

(a)

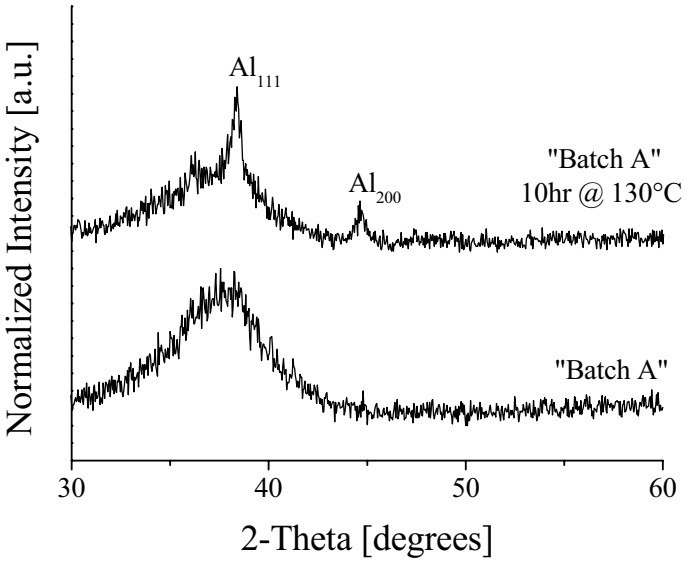

(b)

Figure 5.3: X-ray diffraction pattern of $Al_{92}Sm_8$. (a) 3 batches (A, B, C) of samples produced undered conditions controlled as identical as possible. (b) batch A as quenched and batch A annealed under 130 °C for 10 hours. Little difference is seen among the as-quenched samples, although it does seem to show small peaks in (a) batch B and batch C pattern at Al_{111} and Al_{200} diffraction angles, with the pattern of batch C more clear. Figure is from Prof. Perepezko's group (see ACKNOWLEDGEMENT).

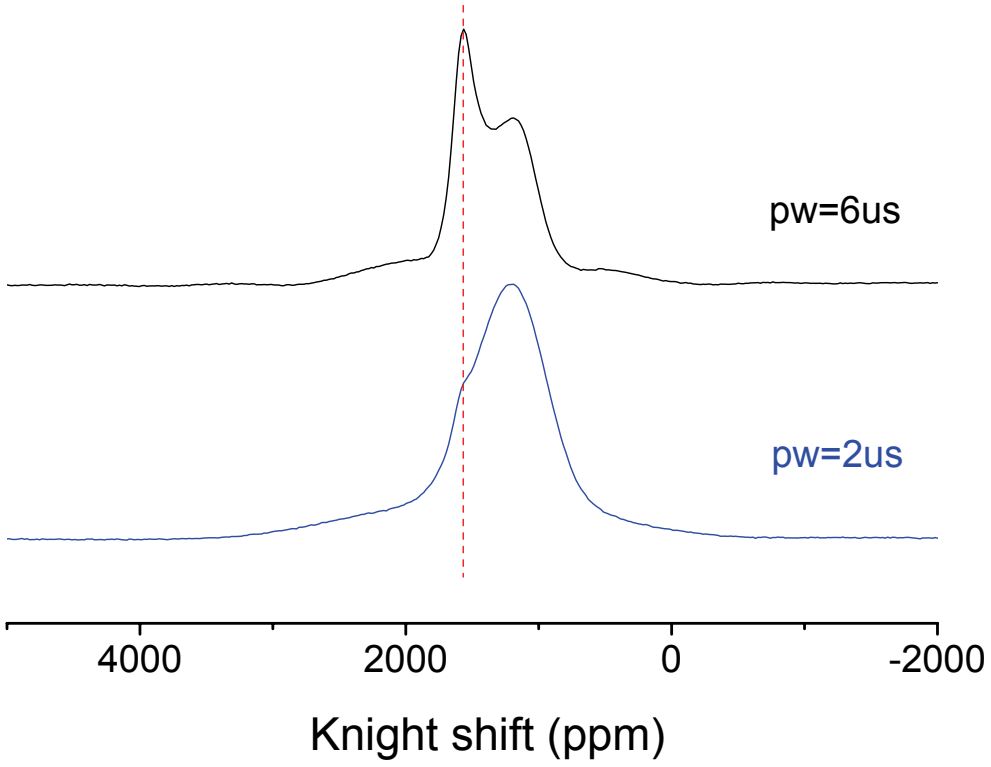

Figure 5.4: Nutation effect. ^{27}Al NMR spectra of $Al_{92}Sm_8$ batch B under same conditions except that the pulse length is different. The difference in spectra indicates that the quadrupole coupling constants for the two peaks are different, so there are two ^{27}Al environment with different symmetry.

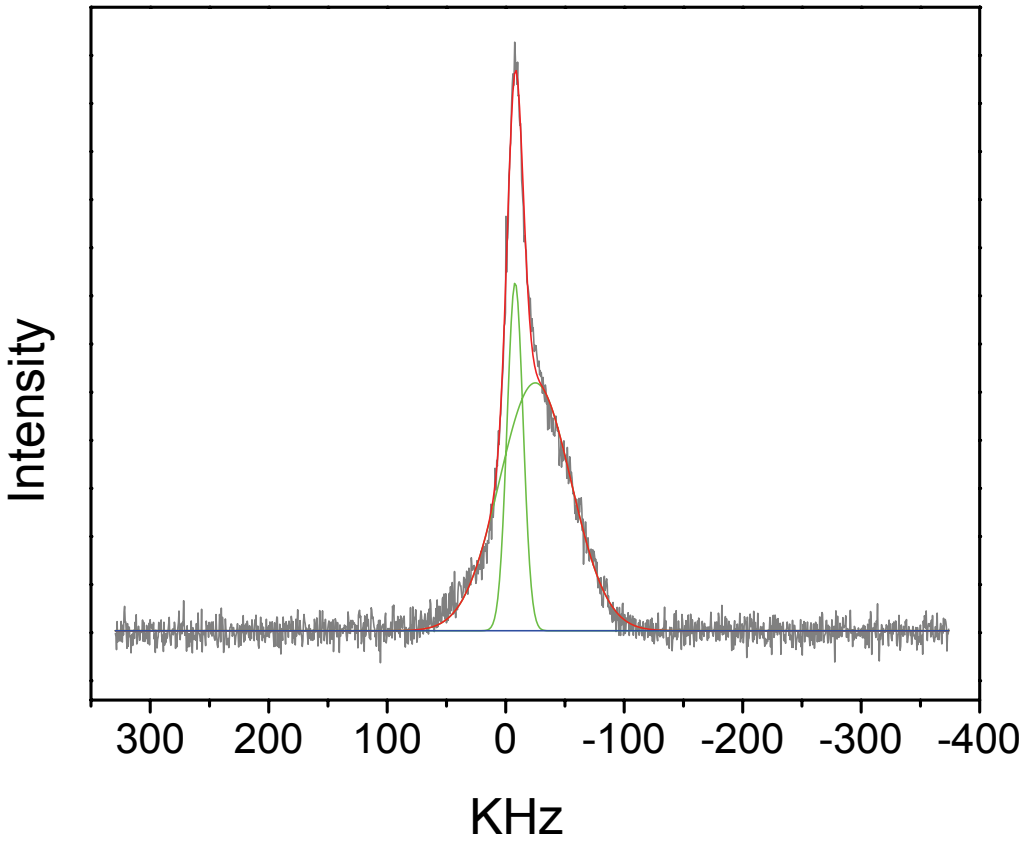

Figure 5.5: Fitting of ^{27}Al NMR spectrum of $Al_{92}Sm_8$ with two peaks. Green lines are the two peaks; red line is the sum of the two peaks; gray line the experimental data; blue line is the baseline.

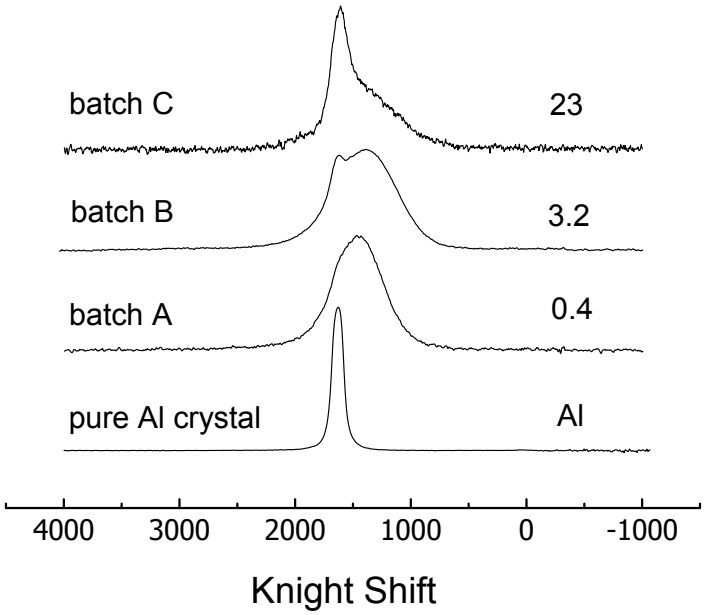

(a)

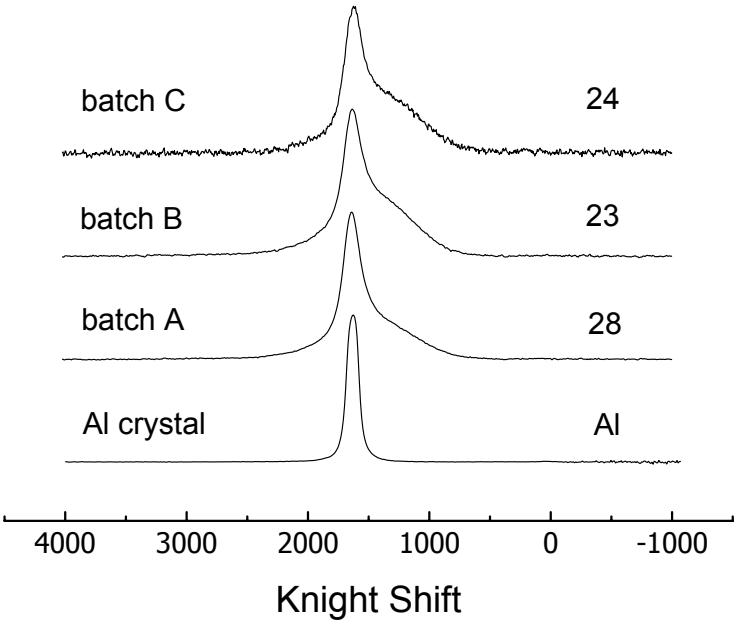

(b)

Figure 5.6: NMR spectra of as-quenched and annealed $Al_{92}Sm_8$ samples. (a) as quenched; (b) after annealing at 130 °C for 10 hours. Spectra of crystalline aluminum are also presented at the bottom of those of the three samples for comparison. The numbers on the right of the figures are atomic percentage of the atoms in the crystalline-aluminum like peak from simulation/calculation.

will experience a second order broadening that is inversely proportional to the external applied magnetic field. For the analysis of NMR spectra one complication introduced by quadrupole coupling is the convolution of RF pluses and the quadrupole interactions (Figure 5.4). Analytical solutions to allow deconvolution can only be obtained for the two extreme conditions (i.e. "hard" pulses and "soft" pulses) while for other conditions it is necessary to rely on numerical calculations. Here we see convolution effect in Figure 5.4, so numerical methods must be employed to study the quadrupole effects.

For analysis of the NMR spectra involving quadrupole nuclei it is essential to determine the quadrupole coupling constant. For the broad peak corresponding to the amorphous phase in Figure 5.5, the quadrupole coupling constant was determined by frequency sweeping method where a set of RF frequencies is used to observe steps for the satellite transitions. From this approach the quadrupole coupling constant was calculated to be about 9 MHz. The quadrupole coupling constant for the narrow peak in Figure 5.5 was determined from the field dependence of the line shape. A fitting of the line shape using the SIMPSON program resulted in a quadrupole coupling constant of 7.5 MHz for the broad peak and 3 MHz for the narrow peak. The line-broadening used for the fitting analysis is for 60 kHz and 15 kHz for the broad and narrow peak respectively at high field and 30 kHz and 7.5 kHz at the low field.

For a quadrupole coupling constant of about 9 MHz, a 20 kHz RF pulse will remain in the "soft" pulse limit while the 90 and 180 degree pulses are still sufficiently short to cover the whole spectrum. In order to set the RF strength exactly an aqueous solution of aluminum nitride was used while the Q factor effect is also taken into account when the samples are changed in the instrument. For a 3 MHz quadrupole coupling constant, although a 20 kHz pulse is not strictly soft, the effect of convolution is very small on the overall analysis as can be verified by simulation. For the same number of nuclei in the sample, but with different quadrupole coupling constants (i.e. 3 MHz and 9 MHz),

the SIMPSON simulation that was carried out with the same parameters as those in a real experiment, yielded a relative output of spectrum intensity of 111 for the narrow peak and 97 for the broad peak.

5.1.3 Experimental Results

In order to establish a basis for comparison, the observations on melt spun amorphous ribbons are analyzed from three separate processing runs that were conducted to be replicate runs. For this purpose, in addition to processing the identical alloy chemistry (i.e. $Al_{92}Sm_8$), the key melt spinning process parameters that can be controlled such as wheel speed (55 m/s), melt superheat and duration, gas ejection pressure and nozzle size were maintained to be as identical as is possible. As revealed in Figure 5.3, the x-ray diffraction patterns from the three samples were essentially identical and indicate that they are macroscopically amorphous. There might be slight indication of crystalline aluminum phase in Figure 5.3(a) batch C sample, but it's barely distinguishable. Other common diagnostic measures such as TEM examination and DSC examination that are shown in Figure 5.2 and 5.1 provide evidence that the three samples are amorphous and in terms of the usual structural and thermal behavior for the onset of primary crystallization are essentially identical.

While XRD, thermal analysis, and electron microscopy studies do not indicate significant differences in the microstructure of as-solidified samples due to processing conditions during melt spinning, the NMR spectra from the independent specimens show clear and quantitative differences 5.6(a). Based upon a comparison with the Knight shift from pure crystalline Al the different samples display a noticeable amount of Al in a crystalline-like environment as well as the majority of Al in less well-defined amorphous environment.

NMR scans (measured with identical pulse sequences under identical conditions) of

different ribbon samples show a broad signal peaking at a Knight shift position slightly up-field (lower shift) than that of the pure Al coupled with the presence of a small peak at the Knight shift position corresponding to pure Al (Figure 5.5). However, the relative magnitude of the Al peak is distinctly different between the sample batches, indicating that different volume fractions of each sample exist in a specific local atomic configuration corresponding to clusters of Al atoms. Since NMR is sensitive to the local atomic environment, the configuration of the Al cluster represents Al with Al atoms as first nearest neighbour with similar coordination number to that for crystalline fcc Al. The broad peak at the up-field position corresponds to the Al-rich amorphous phase in the as-solidified samples. Analysis of NMR measurements on the independent as-solidified MSR batches show that the volume percentage of aluminum in the amorphous matrix, clustered into a specific local atomic environment representative of crystalline Al, ranges from 0.4–23 vol% in separate sample batches. From this analysis it is apparent that amorphous Al alloys are indeed sensitive to processing conditions. Even in a given laboratory and when processing of a given alloy composition is replicated as much as possible, there is a notable difference in the as-quenched condition of the samples.

For further comparison, NMR scans of MSR samples that were annealed at 130 °C for 10 hrs show an intense Al peak indicating that a large volume fraction with a small variation between 23 and 28 vol.% of Al clusters is present in the matrix. Of course, in this case as illustrated by the TEM image in Figure 5.2(c), the Al is now present in the form of a high number density of nanocrystals. It is remarkable that in spite of the rather large variation in the initial condition of the samples with respect to the volume fraction containing Al clusters, the final state after a common annealing treatment was essentially the same.

5.1.4 Discussions

It is important to note that according to the NMR spectra, the disparity in initial states does not affect significantly the final state after annealing. This has two implications. First, a relaxation process must be occurring during the isothermal annealing treatment to allow for the approach to a common end state in terms of the fraction of the volume in an Al crystalline environment. Secondly, there's a metastable equilibrium state for $Al_{92}Sm_8$ at temperatures well below the reported glass transition temperature. This metastable equilibrium state must be, according to Figure 5.3 and 5.2, nanocrystalline Al embedded in amorphous matrix.

There's no obvious difference in NMR spectra between as-quenched and annealed sample of batch C. The x-ray results are obviously different, however. If we look closely, there's some indication of crystalline Al phase in batch C as-quenched x-ray pattern (5.3), this suggests that there should be some small clusters of Al, however dilute, in at least medium range ordered structure to be observable via x-ray diffraction, and these clusters should be shown in NMR spectrum. But this is not enough to account for the high fraction of the narrow peak in NMR spectrum. The high fraction of narrow peak in batch C must be coming from Al that have crystalline-Al like short range order but lacking a long range order necessary for x-ray observation. From the difference among three batches of sample, such crystalline-Al like local configuration is sensitive to quenching. A less favorable quenching would induce Al local ordering and growing of Al-rich region. But even at low temperatures, the Al atoms have enough mobility to migrate across several atoms to form large crystalline clusters.

In conclusion, our studies show that: 1) Al in $Al_{92}Sm_8$ like to form local crystalline Al ordering; 2) The percentage of locally ordered Al is dependent on subtle quenching conditions; 3) even at low temperatures (130 ^{o}C), Al have enough mobility, and will migrate towards more crystalline Al ordering. 4) there's a common metastable state

at low temperature and that's nano-crystalline Al clusters embedded in amorphous matrix.

5.2 Glass Forming Ability

5.2.1 GFA and CSRO

Metallic glass sample discussed in this session, except that of the Yttrium-base sample, are obtained from Dr. Wang's group at the Institute of Physics, Chinese Academy of Sciences. Alloys with nominal compositions were prepared by arc melting pure Cu, Al, Zr with industrial grade Ce in Ti-gettered argon atmosphere. The purity of Ce is only about 99.5 wt%, which is much lower that that of other base elements. The alloy ingots were remelted and suck cast into a Cu mold to get cylindrical rods with different diameters. The Yttrium-based sample was obtained from Poon's group at Univ. of Virginia. The glass forming ability of $Y_{36}Sc_{20}Al_{24}Ni_{10}Co_{10}$ is so good that a cast step is not necessary—the alloys can directly form metallic glass ingots. Yttrium-based metallic glass rods can also be produced by vacuum sealing the ingots in quartz tubes, heating to molten state in an oven and a subsequent water quenching.

We see very small shifts for $Y_{36}Sc_{20}Al_{24}Ni_{10}Co_{10}$ and $Zr_{45}Cu_{45}Al_{10}$ and $Zr_{47}Cu_{47}Al_6$ samples (Figure 5.7a). An interesting but probably too simplistic explanation is that there is a minimum in the density of states at the Fermi level. Some believe that such minimum in electronic energy stabilizes the structure of metallic glasses and is responsible for the GFA of some metallic glasses (Nagel and Tauc, 1975). Such situation occurs in icosahedral alloys which indeed show a very small ^{27}Al Knight shift (Tang et al., 1997). Icosahedral short range order in metallic supercooled liquids and glasses has been observed experimentally (Kofalt et al., 1986; Xing et al., 2000; Saida et al., 2001; Chen et al., 2001; Takagi et al., 2001; Luo et al., 2004) and via computer simula-

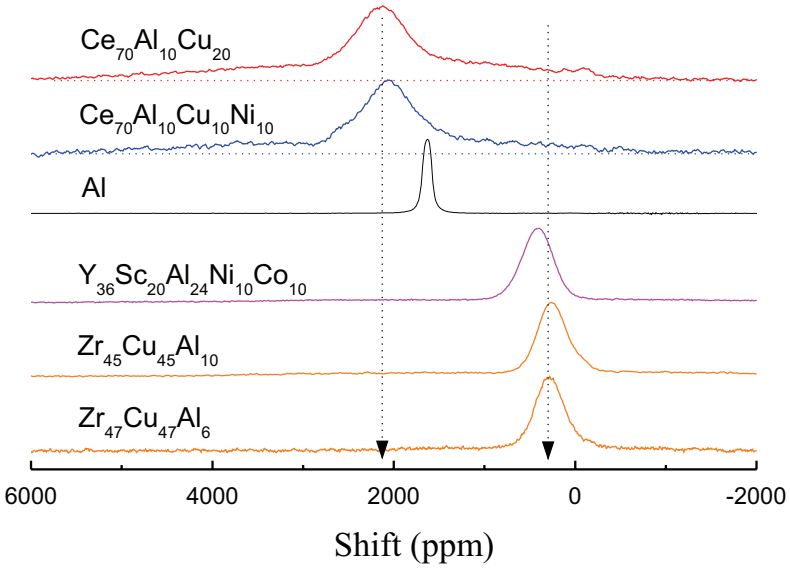

(a) ^{27}Al Spectra

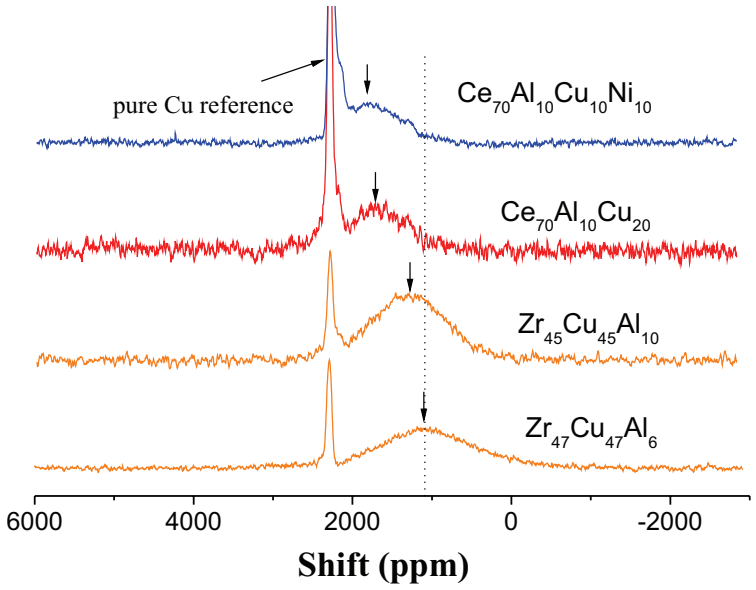

(b) ^{65}Cu Spectra

Figure 5.7: RT ^{27}Al and ^{65}Cu spectra of various matellic glass systems at 9.4 Tesla.

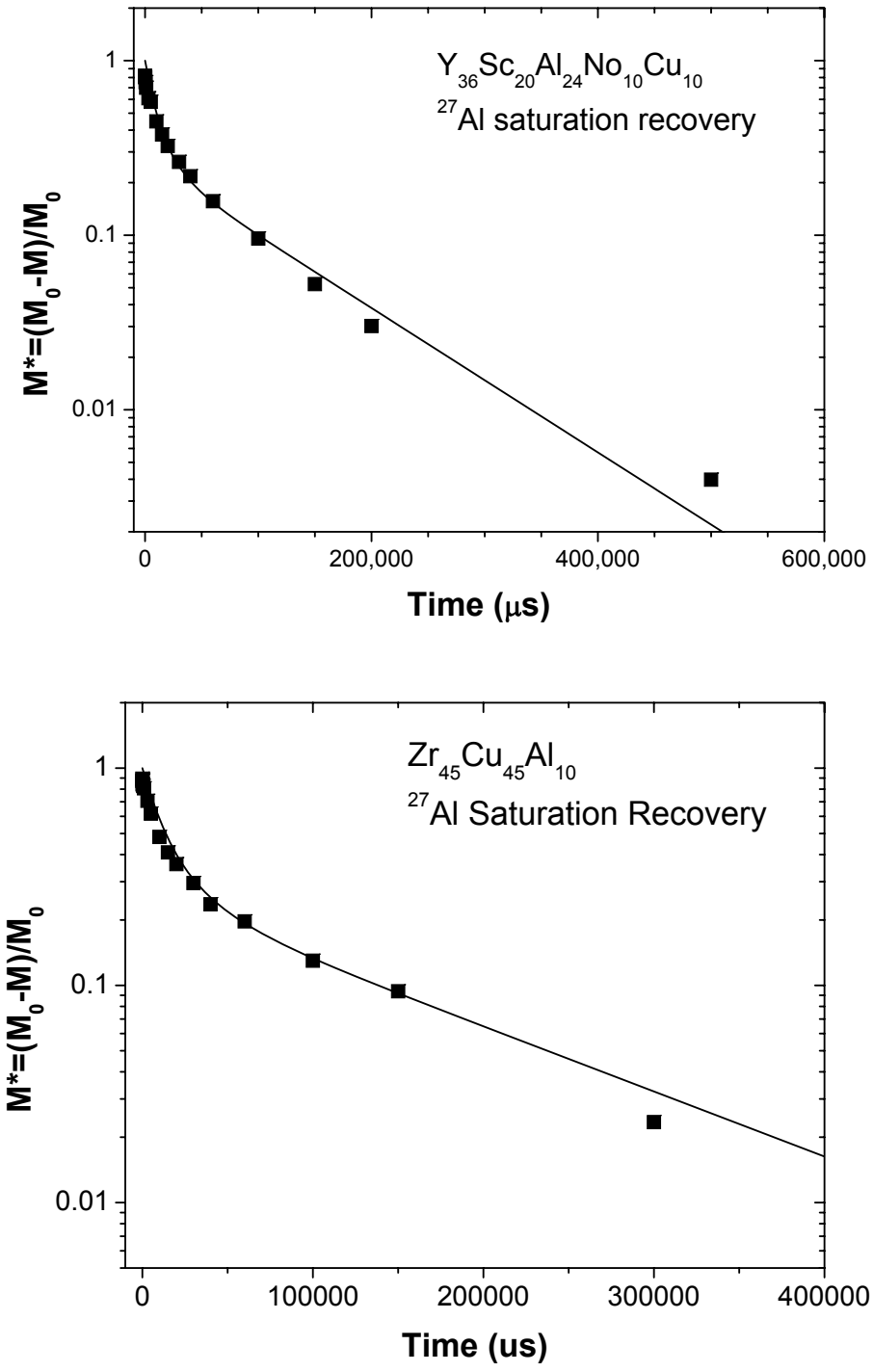

Figure 5.8: ^{27}Al T_1 measurements using saturation recovery pulse sequence with echo detection. Soft pulse excitation was for measurements. Best fit was obtained with Eq. 5.1

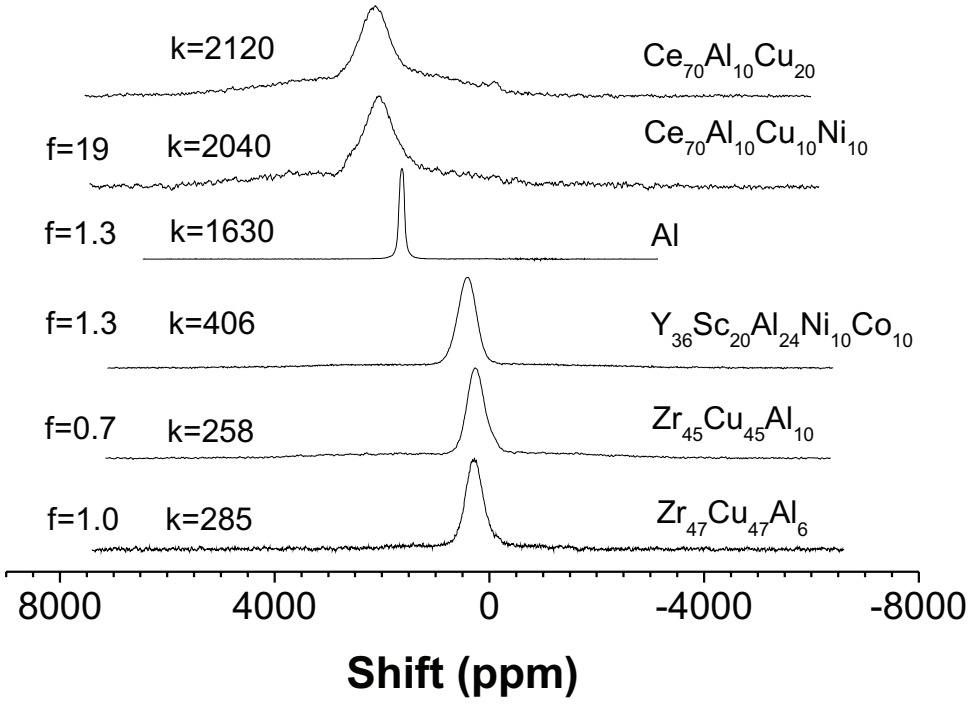

Figure 5.9: Knight shift and enhancement factor of ^{27}Al for various metallic glass samples. k is Knight shift value, and f is enhancement factor according to Eq. 3.10.

tions (Jónsson and Andersen, 1988; Clarke and Jónsson, 1993; Cozzini and Ronchetti, 1996). Since most of the icosahedral short range order in supercooled metallic liquids and glasses reported in literature are Zr-based, it is possible that high content of Zr favors the formation of icosahedral ordering. The current situation is more complicated when we look at the ^{65}Cu spectra. Figure 5.7b shows the ^{65}Cu NMR spectra of $Ce_{70}Al_{10}Cu_{10}Ni_{10}$, $Ce_{70}Al_{10}Cu_{20}$, $Zr_{45}Cu_{45}Al_{10}$ and $Zr_{47}Cu_{47}Al_6$ BMGs. The Knight shift of ^{65}Cu in $Cu_{45}Zr_{45}Al_{10}$ and $Zr_{47}Cu_{47}Al_6$ are 1300 ppm and 1100 ppm, respectively, significantly smaller than that of pure copper at 2300 ppm. However, a shift of over 1000 ppm still represents a strong metallic character unlike that at the Al sites. We noticed that increasing the Al content from 6 to 10 at% increases the ^{65}Cu Knight shift (thus the density of state at the Cu sites) notably (Figure 5.7b) although the shift of ^{27}Al peak decreases very slightly at the same time (Figure 5.7a). This might explain the decreasing of GFA when the Al content goes from 6 at% to 10 at%. This result suggests that a balance has to be observed in the process of promoting GFA. Adding Al to ZrCu introduces covalent bonding (possibly with Zr) which favors chemical short range order and obviously improved the GFA over that of CuZr. However, too much Al could also lead to unfavorable effect, namely, increasing the density of states at the Fermi level at the Cu sites thus increasing the electronic energy. It's also possible that too much Zr-Al bonding will lead to easier aggregation of ZrAl atoms and less binding energy between Cu and other elements and thus favors nucleation and growth.

The character of bonding can be further characterized by the rate of spin-lattice relaxation. For quadrupole nuclei, the situation can be more complicated since there can be multiple relaxation rates (Andrew and Tunstall, 1961; McDowell, 1995). We used saturation recovery pulse sequences with echo detection and chose a pulse length such that we only saturate the central transition. In this condition, the recovery curve

should follow the equation:

$$M = M_0 \left[1 - 0.25714 \exp(-\frac{t}{T_1}) - 0.26667 \exp(-\frac{6t}{T_1}) - 0.47619 \exp(-\frac{15t}{T_1}) \right] \quad (5.1)$$

Now we can calculate the enhancement factor according to Eq. 3.10. The final results are listed in Figure 5.9. We see that for sample $Zr_{45}Cu_{45}Al_{10}$, the enhancement factor is even smaller than 1 which indicates that there's a significant portion of the shift that may come from chemical shift or second order effect of quadrupole Hamiltonian. There might also exist contributions of T_1 from NQR. Detailed information can be obtained from accurate studies on temperature dependence.

5.2.2 GFA and Electronic Structure

In contrast to $Y_{36}Sc_{20}Al_{24}Ni_{10}Co_{10}$, $Zr_{45}Cu_{45}Al_{10}$ and $Zr_{47}Cu_{47}Al_6$ systems, the ^{27}Al spectra of $Ce_{70}Al_{10}Cu_{10}Ni_{10}$ and $Ce_{70}Al_{10}Cu_{20}$ in Figure 5.7a exhibit a shift that is even larger than that of pure aluminum. Moreover, there is also a broad peak underlying the sharp peak. The most likely reason for this larger than pure aluminum shift as well as the presence of the broad peak is the paramagnetic effect from $4f$ orbitals in Ce sites.

Cerium metal as well as Cerium compounds have been studied extensively in the past because of its interesting electronic properties. For example, FCC cerium metal can have an isomorphic phase transition from low density ($a_0 = 5.15$ Å) γ state to high density ($a_0 = 4.85$ Å) α state by increasing pressure or reducing temperature. The large increase in cell volume associated with this transition arises from the change in electronic structure. In the γ state cerium ions primarily have the trivalent $4f^1(5d6s)^3$ structure, while in the α state, the electronic structure of cerium fluctuates between trivalence and tetravalence $4f^0(5d6s)^4$. The fluctuation of valency has been observed in a number of cerium crystalline and amorphous alloys, and under low temperatures com-

plicated magnetic interactions will occur. However, under room temperature, cerium ion can be paramagnetic or non-magnetic depending on its electronic state. Here the anomalous Knight shift and the extremely broad peak under a relatively narrow one must be related to this intriguing electronic properties of cerium.

5.2.2.1 Ce Valence Fluctuation

First of all, the Knight shift of ^{27}Al is even larger in Ce-based metallic glasses than in Al metal which is not common in these type of metallic glasses (Figure 5.7). However, if we consider the transferred hyperfine field H_f at Al site mediated through $4f$/conduction electron exchange, this can be readily explained.

The effective magnetic field at Al site can be written as (Ghoshray et al., 2002):

$$\mathbf{H} = \mathbf{H}_0 + \mathbf{H}_c + \mathbf{H}_d^{4f} + \mathbf{H}_{vf}^{4f} \tag{5.2}$$

where $\mathbf{H}_0$ is the applied magnetic field, $\mathbf{H}_c$ is the contact hyperfine field due to conduction electrons, $\mathbf{H}_d^{4f}$ is the dipolar field due to the Ce $4f$ electrons, and $\mathbf{H}_{vf}^{4f}$ is the contribution to the contact hyperfine field due to transfered magnetic moment from $4f$ orbitals. The additional Knight shift that arises from the $4f$ valence fluctuations is:

$$K_{s-f} = \frac{H_{vf}}{N_A \mu_B} \chi_M^f(T) \tag{5.3}$$

where H_{vf} is the transferred hyperfine field which is related to the transferred hyperfine coupling constant A_{hf} as $H_{vf} = A_{hf}/\gamma\hbar$, N_A is the Avogadro's number, μ_B is the Bohr magneton, χ_M^f is the Ce $4f$ electron contribution to the molar susceptibility. Thus as long as H_{vf} remains constant, K_{s-f} should follow $\chi_M^f(T)$ linearly. In our metallic glass system, the unusually large Knight shift should come from this contribution of $4f$-conduction electron fluctuation effect.

5.2.2.2 Dipolar Coupling

When there are dipolar interactions between nuclear and electron spins, the classic Pake doublet will not occur due to the extremely fast electronic relaxation time on NMR time scale. The line shape then resembles that of CSA. The Hamiltonian can be represented by

$$H_d^{en} = \frac{\mu_0}{4\pi}\bar{\mu_e}\tilde{D_{en}}\mu_n \tag{5.4}$$

where $\bar{\mu_e}$ is the averaged magnetic moment of the electrons, μ_n the magnetic moment of the nuclei, μ_0 the permeability, and $\tilde{D}_{en}$ is the dipolar coupling tensor between the unpaired electron and the nucleus, defined at follows:

$$D_{ij} = \frac{1}{r^3}(\delta_{ij} - 3e_i e_j) \tag{5.5}$$

If $\bar{u_e}$ is isotropic, the diploar interaction results in a line broadening of the resonance only but no overall shift. But this will not be the case for an anisotropic magnetic moment. Here both line broadening and a pseudo-contact shift will occur. The pseudo-contact shift due to a lanthanide ion is shown to be proportional to $1/T^2$ (Grey et al., 1990; Bleaney, 1972).

If we assume that the main contribution to the Knight shift of the narrow peak in NMR spectra of Ce-based alloys (Figure 5.7a) is due to valence fluctuation effect, then the influence of dipolar coupling should be small. This is not surprising (Ghoshray et al., 2002; Grey and Dupre, 2004). But then it's difficult to account for the broad peak underlying the narrow one. So here in Ce-based metallic glasses there exist at least two types of Al environment, one with Ce neighbors that are completed depleted with $4f$ orbitals, so the dipole coupling with $4f$ electrons now remains minimal, the other one with Ce neighbors that have fluctuating $4f$ orbitals. In a metallic system where we can have very different valency state for the same element, the atomic configuration

and bonding of the same element must be very different so that the energy level of the same orbital can be altered.

5.2.2.3 Micro-alloying

Recently some unusual GFA in the Ce-based system was observed (Zhang et al.,): with the addition of 0.5 % Co in $Ce_{70}Al_{10}Cu_{20}$, the critical thickness of the BMG can increase from 2 mm to 10 mm. We speculate that such unusual GFA may be intimately related to the electronic properties. Figure 5.10 presents some preliminary results of this study. From Figure 5.10, we see the difference between the spectrum of $Ce_{70}Al_{10}Cu_{20}$ and that of $Ce_{69}Al_{10}Cu_{20}Co_1$. First of all, with the addition of Co, the Knight shift of the narrow peak becomes lower. With the introduction of Co and thus more states at lower energy, the average occupation number of $4f$ states might get lower and so there will be less contribution from s-$4f$ exchange interaction. More interesting phenomenon is that the overall percentage of the broad peak is much smaller with the addition of Co. This might indicate that with the addition of Co and a change in electronic state, the system now favors a more ordered CSRO and has tighter bonding and thus the GFA is improved[1].

[1] After the writing of this dissertation, recent studies suggest that the convolution of the Hamiltonian due to the interaction of spin dipole moment with electronic magnetic dipole moment and that of spin system with the rf pulses may also play a role in the change of relative intensity of the two peaks. Detailed investigation is still ongoing.

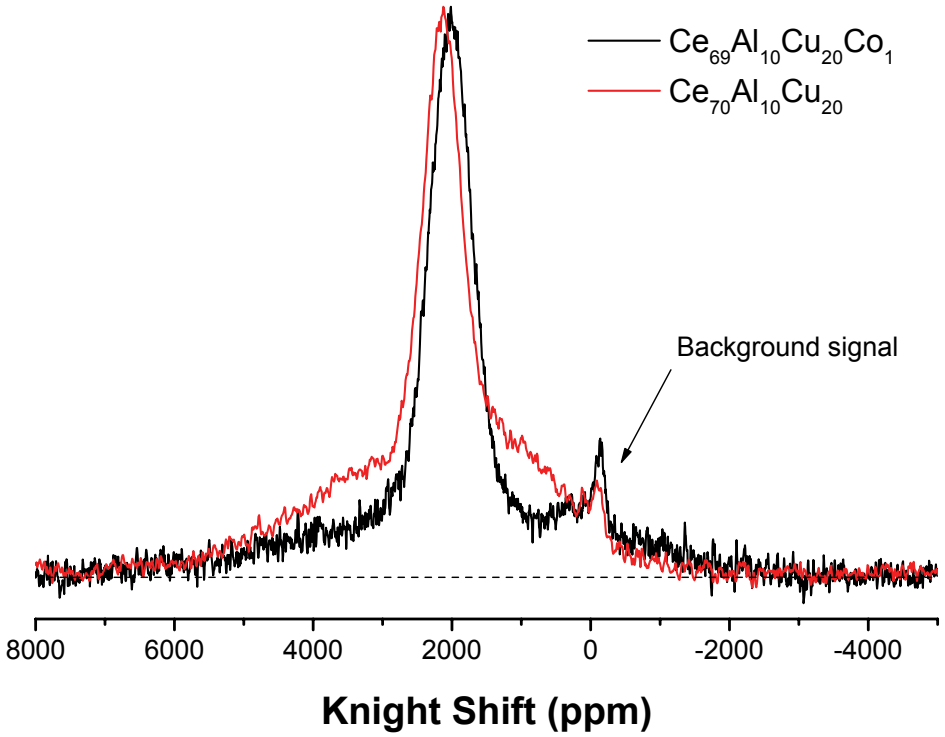

Figure 5.10: NMR spectra of ^{27} in $Ce_{69}Al_{10}Cu_{20}Co_1$ and $Ce_{70}Al_{10}Cu_{20}$. The Knight shift of the sample that contains 1% Co changed to lower frequency, which means that the DOS gets lower. At the same time, the intensity of the broad peak is reduced. Dashed line is the base line of the spectra.

BIBLIOGRAPHY

Abragam, A. (1961). *the Principle of Nuclear Magnetism.* Oxford University Press, London.

Alam, T. and Brow, P. (1998). Local structure and connectivity in lithium phosphate glasses: a solid-state p-31 mas nmr and 2d exchange investigation. *J. Non-Cryst. Solids*, 223:1.

Andrew, E. R. and Tunstall, D. P. (1961). Spin-lattice relaxation in imperfect cubic crystals and in non-cubic crystals. *Proc. Phys. Soc.*, 78:1.

Angelani, L., Leonardo, R. D., Ruocco, G., Scala, A., and Sciortino, F. (2000). Saddles in the energy landscape probed by supercooled liquids. *Phys. Rev. Lett.*, 85:5356.

Angell, C. A. (1988). Perspective on the glass transition. *J. Phys. Chem. Sol.*, 49:863.

Angell, C. A. (1995). Formation of glasses from liquids and biopolymers. *Science*, 267:5206.

Bain, A. and Duns, G. (1996). A unified approach to dynamic nmr based on a physical interpretation of the transition probability. *Can. J. Chem*, 74:819.

Benedek, G. B. and Kushida, T. (1958). The pressure dependence of the knight shift in the alkali metals and copper. *J. Phys. Chem. Solids*, 5:241.

Bengtzelius, U., Götze, W., and Sjölander, A. (1984). Dynamics of supercooled liquids and the glass-transition. *J. Phys. C*, 17:5915.

Bernu, B., Hiwatari, Y., and Hansen, J. P. (1985). A molecular dynamics study of the glass transition in binary mixtures of soft spheres. *J. Phys. C: Solid State Phys.*, 18:L371.

Bhattacharyya, S. M., Bagchi, B., and Wolynes, P. G. (2005). Bridging the gap between the mode coupling and the random first order transition theories of structual relaxation in liquids. cond-mat/05050301.

Bleaney, B. (1972). Nuclear magnetic resonance shifts in solution due to lanthanide ions. *J. Magn. Resnon.*, 8:91.

Broderix, K., Bhattacharya, K. K., Cavagna, A., Zippelius, A., and Giardina, I. (2000). Energy landscape of a lennard-jones liquid: Statistics of stationary points. *Phys. Rev. Lett.*, 85:5360.

Chapman, S. and Cowling, T. G. (1991). *The Mathematical Theory of Non-uniform Gases*. Cambridge University Press, Cambridge, England.

Chen, H. S. (1974). Thermodynamic considerations on the formation and stability of metallic glasses. *Acta Metall.*, 22:1505.

Chen, H. S. and Turnbull, D. (1968). Evidence of a glass-liquid transition in a gold-germanium-silicon alloy. *J. Chem. Phys.*, 48:2560.

Chen, H. S. and Turnbull, D. (1969). Formation, stability and structure of palladium-silicon based alloy glasses. *Acta Metall.*, 17:1021.

Chen, M. W., Dutta, I., Zhang, T., Inoue, A., and Sakurai, T. (2001). Kinetic evidence for the structural similarity between a supercooled liquid and an icosahedral phase in zr65al7.5ni10cu12.5ag5 bulk metallic glass. *Appl. Phys. Lett.*, 79:42.

Claridge, E., Moore, D. S., Seymour, E. F. W., and Sholl, C. A. (1972). Nuclear quadrupole interactions in liquid alloys. *J. Phys. F: Metal Phys.*, 2:1162.

Clarke, A. S. and Jónsson, H. (1993). Structural changes accompanying densification of random hard-sphere packings. *Phys. Rev. E*, 47:3975.

Cozzini, S. and Ronchetti, M. (1996). Local icosahedral structures in binary-alloy clusters from molecular-dynamics simulation. *Phys. Rev. B*, 53:12040.

Das, S. P. and Mazenko, G. F. (1986). Fluctuating nonlinear hydrodynamics and the liquid-glass transition. *Phys. Rev. A*, 34:2265.

Debenedetti, P. G. and Stillinger, F. H. (2001). Supercooled liquids and the glass transition. *Nature*, 410:259.

Denny, R. A., Reichman, D. R., and Bouchaud, J.-P. (2003). Trap models and slow dynamics in supercooled liquids. *Phys. Rev. Lett.*, 90:025503.

Donth, E. (2001). *The Glass Transition: Relaxation Dynamics in Liquids and Disordered Materials*. Springer.

Drehman, A. J., Greer, A. L., and Turnbull, D. (1982). Bulk formation of a metallic glass: Pd40ni40p20. *Appl. Phys. Lett.*, 41:716.

Ernst, R. R., Bodenhausen, G., and Wokaun, A. (1990). *Principles of Nuclear Magnetic Resonance in One and Two Dimensions*. Oxford.

Fahrenheit, D. B. (1724). *Phil. Tans. Roy. Soc.*, 33:78.

Gaskell, T. and Woolfson, M. S. (1984). Temperature dependence of the quadrupolar relaxation rate in liquid metals. *Phys. Lett. A*, 105:83.

Geszti, T. (1983). Pre-vitrification by viscosity feedback. *J. Phys. C*, 16:5805.

Ghoshray, K., Bandyopadhyay, B., and Ghoshray, A. (2002). Nmr study of the electronic state in the dense kondo compound cenial4. *Phys. Rev. B*, 65:174412.

Goldstein, M. (1969). Viscous liquids and the glass transition: A potential energy barrier picture. *J. Chem. Phys.*, 51:3728.

Götze, W. (1984). Some aspects of phase-transitions described by the self-consistent current relaxation theory. *Z. Phys. B*, 56:139–154.

Götze, W. (1985). Properties of the glass instability treated within a mode-coupling theory. *Z. Phys. B*, 60:195–203.

Götze, W. and Sjögren, L. (1992). Relaxation processes in supercooled liquids. *Rep. Prog. Phys.*, 55:241–376.

Greer, A. L. (1995). Metallic glasses. *Science*, 267:1947.

Grey, C. P. and Dupre, N. (2004). Nmr studies of cathode materials for lithium-ion rechargeable batteries. *Chem. Rev.*, 104:4493.

Grey, C. P., Smith, M. E., Cheetham, A. K., Dobson, C. M., and Dupree, R. (1990). Yttrium-89 magic angle spinning nmr study of rare-earth pyrochlores: paramagnetic shifts in the solid state. *J. Am. Chem. Soc.*, 112:4670.

Guo, F., Poon, S. J., and Shiflet, G. J. (2003). Metallic glass ingots based on yttrium. *Appl. Phys. Lett*, 83:2575.

Hansen, J.-P. and McDonald, I. R. (1990). *The Theory of Simple Liquids.* Academic, London.

He, Y., Poon, S. J., and Shiflet, G. J. (1988). Synthesis and properties of metallic glasses that contain aluminum. *Science*, 241:1640.

Hines, W. A., Glover, K., Clark, W. G., Kabacoff, L. T., Modzelewski, C. U., Hasegawa, R., and Duwez, P. (1980). Electronic-structure of the ni-pd-p and ni-pt-p metallic glasses - a pulsed nmr-study. *Phys. Rev. B.*, 21:3771.

Inoue, A. (2000). Stabilization of metallic supercooled liquid and bulk amorphous alloys. *Acta Mater.*, 48:279.

Inoue, A., Ohtera, K., Tsai, A.-P., and Masumoto, T. (1988). New amorphous alloys with good ductility in al-y-m and al-la-m (m=fe, co, ni or cu) systems. *Jpn. J. Appl. Phys.*, 27:L280.

Jäckle, J. (1986). Models of the glass transition. *Rep. Prog. Phys.*, 49:173.

Jónsson, H. and Andersen, H. C. (1988). Icosahedral ordering in the lennard-jones liquid and glass. *Phys. Rev. Lett.*, 60:2295.

Kasowski, R. V. (1969). Temperature-dependent knight shift in cadmium: A theoretical study. *Phys. Rev.*, 187:891.

Kasowski, R. V. and Falicov, L. M. (1969). Calculation of the temperature dependence of the knight shift in cadmium. *Phys. Rev. Lett*, 22:1001.

Kawasaki, K. (1966). Correlation-function approach to the transport coefficients near the critical point. i. *Phys. Rev.*, 150:291.

Kirkpatrick, T. R. and Thirumalai, D. (1987). Dynamics of the structual glass transition and the p-spin-interaction spin-glass transition. *Phys. Rev. Lett.*, 58:2091.

Kirkpatrick, T. R. and Wolynes, P. G. (1987a). Connections between some kinetic and equilibrium theories of the glass transition. *Phys. Rev. A*, 35:3072.

Kirkpatrick, T. R. and Wolynes, P. G. (1987b). Stable and metastable states in mean-field potts and structual glass. *Phys. Rev. B*, 36:8552.

Klement, W., J., Willens, R. H., and Duwez, P. (1960). Noncrystalline structure in solidified gold-silicon alloys. *Nature*, 187:869.

Kofalt, D. D., Nanao, S., K., T. E., Wong, M., and Poon, S. J. (1986). Differential anomalous-x-ray-scattering study of icosahedral and amorphous pd58.8u20.6si20.6. *Phys. Rev. Lett.*, 57:114.

Kohlrausch, R. (1854). Theorie des elektrischen rückstandes in der leidener flasche. *Ann. Phys. (Leipzig)*, 91:179.

Korringa, J. (1950). Nuclear magnetic relaxation and resonnance line shift in metals. *Physica*, 16:601.

Kui, H. W., Greer, A. L., and Turnbull, D. (1984). Formation of bulk metallic glass by fluxing. *Appl. Phys. Lett*, 45:615.

Leutheusser, E. (1984). Dynamical model of the liquid-glass transition. *Phys. Rev. A*, 29:2765.

Lu, I.-R., Görler, G. P., and Willnecker, R. (2002). Specific volume of glass-forming liquid pd43cu27ni10p20 and related thermodynamic aspects of the glass transition. *Appl. Phys. Lett.*, 80:4534.

Lu, I.-R., Wilde, G., Gorler, G., and Willnecker, R. (1999). Thermodynamic properties of pd-based glass-forming alloys. *J. Non-Cryst. Solids*, 252:577–581.

Lubchenko, V. and Wolynes, P. G. (2003). Barrier softening near the onset of non-activated transport in supercooled liquids: Implications for establishing detailed connection between thermodynamic and kinetic anomalies in supercooled liquids. *J. Chem. Phys.*, 119:9088.

Lubchenko, V. and Wolynes, P. G. (2004). Theory of aging in structural glasses. *J. Chem. Phys.*, 121:2852.

Luo, W. K., Sheng, H. W., Alamgir, F. M., Bai, J. M., He, J. H., and Ma, E. (2004). Icosahedral short-range order in amorphous alloys. *Phys. Rev. Lett.*, 92:145502.

Marsden, J., Havill, R. L., and Titman, J. M. (1980). The temperature dependence of the quadrupole relaxation rate in liquid metals and alloys. *J. phys. F: Metal Phys.*, 10:1589.

Martin, P. C., Parodi, O., and Pershan, P. S. (1972). Unified hydrodynamic theory for crystals, liquid crystals, and normal fluids. *Phys. Rev. A*, 6:2401.

Masuhr, A., Waniuk, T. A., Busch, R., and Johnson, W. L. (1999). Time scales for viscous flow, atomic transport, and crystallization in the liquid and supercooled liquid states of zr41.2ti13.8cu12.5no10.0be22.5. *Phys. Rev. Lett.*, 82(11):2290.

Maxim, P., Brinkmann, R., Paulick, C. A., Elwenspoek, M., v. Hartrott, M., Keihl, M., and Quitmann, D. (1986). Nuclear quadrupolar relaxation in liquid alloys and nearest neighbour dynamics. *Z. Naturforsch.*, 41a:118.

McDowell, A. F. (1995). Magnetization-recovery curves for quadrupolar spins. *J. Magn. Reson., Ser A*, 113:242.

Meyer, A. (2002). Atomic transport in dense multicomponent metallic liquids. *Phys. Rev. B*, 66:134205.

Meyer, A., Busch, R., and Schober, H. (1999). Time-temperature superposition of structual relaxation in a viscous metallic liquid. *Phys. Rev. Lett.*, 83:5027.

Meyer, A., Franz, H., Sepiol, B., Wuttke, J., and Petry, W. (1996a). Fast relaxation in a metastable metallic melt. *Europhys. Lett.*, 36:379.

Meyer, A., Wuttke, J., Petry, W., Peker, A., Bormann, R., Coddens, G., Kranich, L., Randl, O. G., and Schober, H. (1996b). Harmonic behavior of metallic glasses up to the metastable melt. *Phys. Rev. B*, 53:12107.

Meyer, A., Wuttke, J., Petry, W., Randl, O. G., and Schober, H. (1998). Slow motion in a metallic liquid. *Phys. Rev. Lett.*, 80:4454.

Mezei, F. (1991). *Liquids, Freezing and Glass Transition.* Elsevier, Amsterdam.

Mezei, F. and Russina, M. (1999). Intermediate range order dynamics near the glass transition. *J. Phys.: Condens. Matter*, 11:A341.

Mori, H. (1965a). A continued-fraction representation of the time-correlation functions. *Prog. Theor. Phys.*, 34:399.

Mori, H. (1965b). Transport, collective motion, and brownian motion. *Prog. Theor. Phys*, 33:423.

Moutain, R. D. and Thirumalai, D. (1987). Molecular-dynamics study of glassy and supercooled states of a binary mixture of soft spheres. *Phys. Rev. A*, 36:3300.

Mukherjee, S., Schroers, J., Zhou, Z., Johnson, W., and Rhim, W.-K. (2004). Viscosity and specific volume of bulk metallic glass-forming alloys and their correlation with glass forming ability. *Acta Mater.*, 52:3689.

Nagel, S. R. and Tauc, J. (1975). Nearly-free-electron approach to the theory of metallic glass alloys. *Phys. Rev. Lett.*, 35:380.

Nishiyama, N., Inoue, A., and Jiang, J. Z. (2001). Elastic properties of pd40cu30ni10p20 bulk glass in supercooled liquid region. *Appl. Phys. Lett*, 78:1985.

Ott, K., Haghani, M. A., Paulick, C. A., and Quitmann, D. (1989). Quadrupolar relaxation and thermodynamical process in liquid metallic alloys. *Prog. NMR Spect.*, 21:203.

Oyama, S., Clark, P., Wang, X., Shido, T., Iwasawa, Y., Hayashi, S., Ramallo-Lopez, J., and Requejo, F. (2002). Structural characterization of tungsten phosphide (wp) hydrotreating catalysts by x-ray absorption spectroscopy and nuclear magnetic resonance spectroscopy. *J. Phys. Chem. B*, 106:1913.

Peker, A. and Johnson, W. L. (1993). A highly processable metallic glass: Zr41.2ti13.8cu12.5ni10.0be22.5. 63:2342.

Pelletier, J. M., de Moortèle, B. V., and Lu, I. R. (2002). Viscoelasticity and viscosity of pd-ni-cu-p bulk metallic glasses. *Mat. Sci. Eng. A*, 336:190.

Perepezko, J., Hebert, R., Tong, W., J, H., HR, R., and G, W. (2003a). Nanocrystallization reactions in amorphous aluminum alloys. *Mater. Trans.*, 44:1982.

Perepezko, J., Hebert, R., Wu, R., and Wilde, G. (2003b). Primary crystallization in amorphous al-based alloys. *J. Non-Cryst. Solids*, 317:52.

Résibois, P. and de Leener, M. (1977). *Classical Kinetic Theory of Fluids.* Wiley Interscience, New York.

Richter, D., Dianoux, A., and Petry, W. (1989). *Dynamics of disordered materials.* Springer, Heidelberg.

Ritter, A. L. and Gardner, J. A. (1971). Pseudopotential calculation of knight-shift temperature and volume dependence in liquid and solid sodium. *Phys. Rev. B*, 3:46.

Saida, J., Matsushita, M., and Inoue, A. (2001). Direct observation of icosahedral cluster in zr70pd30 binary glassy alloy. *Appl. Phys. Lett.*, 79:412.

Sastry, S., Debenedetti, P. G., and Stillinger, F. H. (1998). Signatures of distinct dynamical regimes in the energy landscape of a glass-forming liquid. *Nature*, 393:554.

Schroers, J., Wu, Y., and Johnson, W. (2002). Heterogeneous influences on the crystallization of pd43ni10cu27p20. *Philos. Mag. A*, 82(6):1207–1217.

Sholl, C. A. (1974). Nuclear quadrupolar relaxation in liquid metals. *J. Phys. F: Met. Phys.*, 4:1556.

Slichter, C. P. (1990). *Principles of Magnetic Resonance*. Springer Verlag.

Stillinger, F. H. (1995). A topographic view of supercooled liquids and glass formation. *Science*, 267:1935.

Takagi, T., Ohkubo, T., Hirotsu, Y., Murty, B. S., Hono, K., and Shindo, D. (2001). Local structure of amorphous zr70pd30 alloy studied by electron diffraction. *Appl. Phys. Lett.*, 79:485.

Tang, X., Loffler, J., Schwarz, R., Johnson, W., and Wu, Y. (2005). Structural influence on atomic hopping and electronic states of pd-based bulk metallic glasses. *Appl. Phys. Lett.*, 86:072104.

Tang, X.-P., Hill, E. A., Wonnell, S. K., Poon, S. J., and Wu, Y. (1997). Sharp feature in the pseudogap of quasicrystals detected by nmr. *Phys. Rev. Lett.*, 79:1070.

Turnbull, D. (1961). The liquid state and the liquid-solid transition. *Trans. AIME*, 221:422.

Turnbull, D. (1969). Under what conditions can a glass be formed. *Contemp. Phys.*, 10:473.

Turnbull, D. and Fisher, J. C. (1949). Rate of nucleation in condensed systems. *J. Chem. Phys.*, 17:71.

Ullo, J. and Yip, S. (1989). Dynamical correlations in dense metastable fluids. *Phys. Rev. A*, 39:5877.

v. Hartrott, M., Höhne, J., Quitmann, D., Rossbach, J., Weihreter, E., and Willeke, F. (1979). Systematical trends of nuclear quadrupolar relaxation in metallic liquid alloys of indium. *Phys. Rev. B*, 19:3449.

von Schweidler, E. (1907). Studien über die anomalien im verhalten der dielektrika. *Ann. Phys.*, 24:711.

Wilde, G., Sieber, H., and Perepezko, J. H. (1999). Glass formation versus nanocrystallization in an al92sm8 alloy. *Scripta Mater.*, 40:779.

William W. Warren, J. (1974). Nuclear quadrupolar relaxation in monatomic liquids. *Phys. Rev. A*, 10:657.

Williams, G. and Watts, D. C. (1970). Non-symmetrical dielectric relaxation behaviour arising from a simple empirical decay function. *Trans. Faraday Soc.*, 66:80.

Winter, J. (1971). *Magnetic Resonance in Metals*. Oxford, New York.

Xia, X. and Wolynes, P. G. (2000). Fragilities of liquids predicted from the random first order transition theory of glasses. *Proc. Natl. Acad. Sci. U.S.A.*, 97:2990.

Xia, X. and Wolynes, P. G. (2001a). Diffusion and the mesoscopic hydrodynamics of supercooled liquids. *J. Phys. Chem. B*, 105:6570.

Xia, X. and Wolynes, P. G. (2001b). Microscopic theory of heterogeneity and nonexponential relaxation in supercooled liquids. *Phys. Rev. Lett.*, 86:5526.

Xing, L. Q., Hufnagel, T. C., Eckert, J., Loser, W., and Schultz, L. (2000). Relation between short-range order and crystallization behavior in zr-based amorphous alloys. *Appl. Phys. Lett.*, 77:1970.

Zhang, B., Wang, R. J., Zhao, D. Q., Pan, M. X., and Wang, W. H. unpublished results.

Zöllmer, V., Rätzke, K., Faupel, F., and Meyer, A. (2003). Diffusion in a metallic melt at the critical temperature. *Phys. Rev. Lett.*, 90:195502.

Zubarev, D. N., Morozov, V., and Röpke, G. (1997). *Statistical Mechanics of Nonequilibrium Processes*, volume II. John Wiley & Sons.

Zwanzig, R. (1961). *Lectures in Theoretical Physics*, volume 3. Wiley-Interscience, New York.